Title

Extreme Rain-Snow Level Variations during California Storms

Permalink

https://escholarship.org/uc/item/4db9s236

Author

Osborne, Tashiana

Publication Date

2021

UNIVERSITY OF CALIFORNIA SAN DIEGO

Extreme Rain-Snow Level Variations during California Storms

A dissertation submitted in partial satisfaction of the requirements
for the degree Doctor of Philosophy

in

Oceanography

by

Tashiana Chanté Osborne

Committee in charge:

Arthur J. Miller, Chair
Joel R. Norris, Co-Chair
F. Martin Ralph, Co-Chair
Amin Dezfuli
Myrl Hendershott
Lane Kenworthy
Shang-Ping Xie

2021

The dissertation of Tashiana Chanté Osborne is approved, and it is acceptable in quality and form for publication on microfilm and electronically.

University of California San Diego

2021

DEDICATION

To the children of my family, and to my brother.

To the strong-willed women and men who helped raise me.

~~~~~~~

To those who will inherit Earth next.
~~~~~~~

EPIGRAPH

When I dare to be powerful,
to use my strength in the service of my vision,
then it becomes less and less important whether I am afraid.

Audre Lorde, 1979

Just like moons and like suns,
With the certainty of tides,
Just like hopes springing high,
Still I'll rise.

Still I Rise by Maya Angelou, 1978

TABLE OF CONTENTS

LIST OF KEY TERMS

Water Year	12-month period, 1 October - 30 September, during which precipitation totals are measured for the ending calendar year (i.e., hydrological year)
Cool Season	7-month period, 1 October - 1 May, during which California receives the bulk of its precipitation and experiences cooler atmospheric temperatures (i.e., wet season, winter)
Hydrometeor	particle within Earth's atmosphere consisting of water in any form, such as snow, ice, rain
Snow Level	altitude or elevation where frozen hydrometeors completely melt to become rain (i.e., rain-snow level, atmospheric snow level, rain-snow transition elevation, radar-derived brightband height)
Freezing Level	0°C altitude or elevation typically positioned 100-300 m above the snow level in California (i.e., melting level)
Melting Layer	vertical layer wherein frozen hydrometeors melt as they fall; capped by the freezing level which, in California, exists on the order of 100-300 m above the snow level (i.e., radar-derived bright band)

LIST OF ACRONYMS AND ABBREVIATIONS

MSL	above mean sea level
SLC	snow level change (referring to a rise or fall within one or three hours)
+SLC	snow level rise
-SLC	snow level fall
Ext.	extreme (used in Chapter 3 table and figures)
Exc.	exceptional (used in Chapter 3 table)
Sierra	Sierra Nevada (mountain range in inland California)
AR	atmospheric river (most prevalent type of storm in California)
IVT	integrated water vapor transport
IWV	integrated water vapor

LIST OF FIGURES

LIST OF TABLES

ACKNOWLEDGEMENTS

There are many individuals I would like to thank for the gifts they've shared with me on this journey. I also realize words cannot adequately express my gratitude, but I will do my best to thank those who have played a special role in helping me become the woman I am today.

I'd like to begin with my grandmother, my confidante, and fierce supporter. I'm beyond grateful for you and all I've learned from you. You have believed in me when I didn't know if I could believe in myself. You've been there through times of chaos and life-threatening illnesses and times of celebration. I'd also like to acknowledge my mother and my brother. I recognize and honor the inner fire we each share parts of. It drives us, and encourages creativity and free expression. Being with you in this world has helped deepen my understanding of and approach towards life's endless dualities. My Auntie Jessie and Uncle Gary, thank you for caring for me during an especially difficult period of my life. Thank you for my cousins who brought joy and hope to some of the most painful days. Thank you for helping me prepare for college and adulthood, and showing me what it means to operate as a team.

I'd like to thank more of the village I grew up in: my great aunts and uncles and their children, and my great grandparents (Bert Casper and Marlene Vadnais), many of whom also shared their love of nature with me and, simultaneously, helped spark my interest in natural science. Some of my most cherished memories include swimming in Minnesota lakes, running in rain, identifying animal tracks and scat, collecting fresh treats from my aunts' gardens, and playing outside with my brother and our cousins.

My niece, young cousins, and current and future children of my family: Thank you for reminding us all to play, dream, laugh, rest. You may not know it, but you have deepened my sense of purpose, my "why" in all I do. I wish for your safety and peace of mind, and I carry you in my soul, eternally. I acknowledge and honor the higher powers that be and the ancestral forces within and around us. Know that you are our ancestors' wildest dreams, but the weight of this world is not yours to carry alone.

There are also those who have become part of my life thanks to the brightest stars aligning. I'm grateful for Justin, my steady river. You've provided me a massive amount of love, care, laughter, support. Thank you for helping me purposefully expand my ability to maintain (or regain) inner strength and peace through valleys, peaks, growing pains. Thank you for it all.

Liz, Adi, Yassir, Daniela, Nathalí, Letícia: I thank you for all that you are as soul siblings in science and far beyond. Thanks for being unapologetically you, and proving that doing so allows for magic to happen. I'd like to express gratitude for the Gusse, Warren, and Stokes families for treating me as one of their own for over a decade. I've also been fortunate to gain two new uncles, Otto and Richard. Thank you for your vibrant life stories and voicemail messages (reminds me of another time). I'm appreciative of Ms. Keiara for her tireless efforts to enhance campus climate, and of Sophie and Judy for advocating for my family and me during a difficult time.

From the bottom of my heart, I'd like to thank Anna Wilson. You are truly phenomenal. Thank you for your invaluable mentorship and friendship. Thank you for the tremendous amount of time, energy, and compassion you poured into me. Again, "thank you" is not enough.

I'm also grateful for Gillian Bowser and Diane White Husic. Thank you for showing me what it means to, along with your expertise, bring your heart and identity to the table; to show up and speak out for both yourself and others. Additionally, I thank Brian Arbic for his vision, and for helping me connect with others in meaningful ways. I'd also like to extend my gratitude to the Rocky Mountain Science and Sustainability Network, Coastal Ocean Environment Summer School in Ghana, and Ocean Corps crews. You are the future we want to see.

I remain appreciative of Ben Hatchett for helpful input and enthusiasm on research and manuscript drafts, and for including me in new efforts. Brian Henn, Justin, and Ashish Kashinath, I thank you for helping me learn to write and use data analysis scripts early in my PhD. I would also like to thank glass ceiling-breakers in natural sciences before me for their courageousness and will to pay it forward: Dr. Dawn Wright, Dr. Gillian Bowser, Dr. Brandon Jones, Dr. Lisa White, Dr. Marshall Shepherd, and others.

Thanks to Rob Monroe, Brittany Hook, Diane, and private donors, one of my high school dreams came true during my graduate studies (not one time, but three). I will continue to cherish and share the professional and personal lessons I learned while activating on a global stage at United Nations Climate Summits. Thank you for these powerful experiences.

I'm grateful to individuals of Saint Cloud State University who provided me with extraordinary support and training, and remain supportive to this day. I'd especially like to thank the Multicultural Student Services (Julie Cruz, Angie Witte, Shahzad Ahmad, Shawn Kakuk, Precious Palmer, and others), the Department of Atmospheric and Hydrologic Sciences (K. Pound, T. Hansen, J. Hoff, R. Kubesh, A. Srock), Robert Johnson, Brian Billings, Dale Buske, NSBE mentors, and the lifelong friends I gained. I'd also like to acknowledge supportive supervisors and PIs from undergraduate internships and research experiences, and K-12 educators and coaches (including teachers of Kyrene Akimel A-al MS and Coach Mancuso of Mountain Pointe HS), several of whom helped me build skills and resilience that proved valuable in higher education.

I would like to thank all of my doctoral committee members. Myrl, my academic grandfather, you reserved time outside of class to address my many questions, and expressed support through words that comforted me in trying times. Knowing you is a great joy of mine. Amin, I'm grateful for your exceptional mentorship since the first day I started as an intern. Thank you for helping me learn and grow in research, and for encouraging me throughout the PhD and during my search for postdoctoral opportunities. Shang-Ping, thank you for helping me learn fundamentals of air-sea interactions during one of my favorite graduate courses.

Finally, I express gratitude for my doctoral advisors. Art, you and Jenny invited me in as part of your family. Thank you for going above and beyond, for strongly advocating for and supporting me. Joel, I'm truly grateful for the energy, patience, and countless hours you gifted me to help me train for qualifying exams, learn data analysis techniques, prepare manuscript drafts, and sharpen my skills as a scientist. Marty, thank you for valuing professional development and providing opportunities to grow in these areas. I feel honored to carry the invaluable and unique lessons I learned from each of you, and to pass them on to others.

I would also like to extend gratitude to members of Team Miller, Team Norris, CW3E. I appreciated your virtual company during the recent and ongoing global pandemic. To those mentioned here and others who have been part of this journey: Thank you. I'm grateful to have you in my corner. In closing, I respectfully acknowledge the Kumeyaay Nation whose unceded ancestral home is occupied by UC San Diego, and to whom I owe honor and gratitude.

Chapter 2 and Chapter 3, in part, are being prepared for submission for two publications as: Osborne, T.C., J.R. Norris, A.M. Wilson, B.J. Hatchett, F.M. Ralph, and B. Henn. In both cases, the dissertation author was the primary investigator and author of this material.

VITA

EDUCATION

2021	Doctor of Philosophy in Oceanography, University of California San Diego
2016	Master of Science in Oceanography, University of California San Diego
2014	Bachelor of Science in Meteorology, Saint Cloud State University
2014	Bachelor of Science in Hydrology, Saint Cloud State University

RECENT ROLES

2015-2021	Hydrometeorology Graduate Research, University of California San Diego
2020-2021	Lecturer and Facilitator, Coastal Ocean Environment Summer School in Ghana
2017-2019	United Nations Conference of the Parties Delegate, University of California Revelle and Moravian College
2019	Undergraduate Mentor, Rocky Mountain Science and Sustainability Network
2018	Extreme Precipitation Intern, National Aeronautics and Space Administration

PUBLICATIONS

Osborne, T.C., J.R. Norris, A.M. Wilson, B.J. Hatchett, F.M. Ralph, and B. Henn: A methodology to identify intrastorm changes in radar-derived snow levels, *in preparation for submission to the Journal of Atmospheric and Oceanic Technology.*

Osborne, T.C., J.R. Norris, A.M. Wilson, B.J. Hatchett, F.M. Ralph, and B. Henn: Extreme intrastorm changes in radar-derived snow levels: definition and characteristics, *in preparation for submission to the Journal of Hydrometeorology.*

Whipple, S., S. Tiwari, **T.C. Osborne**, G. Bowser, S.A. Green, P.H. Templer, S. Ho, 2021: Engaging youth environmental alliance in higher education to achieve the Sustainable Development Goals. *SPUR Special Issue on Climate Change*, *sub judice*.

Ferrer, E.M., L.M. Cavole, S. Clausnitzer, D.F. Dias, **T.C. Osborne**, R. Sugla, and E. Harrison, 2021: Entering negotiations: early-career perspectives on the United Nations Conference of Parties and how to address the unfolding climate crisis. *Frontiers in Marine Science*.

Hatchett, B.J., and Coauthors, 2020: Observations of an extreme atmospheric river storm with a diverse sensor network. *Earth and Space Science*, 6, e2020EA001129, https://doi.org/10.1029/2020EA001129.

Henn, B., R. Weihs, A.C. Martin, F.M. Ralph, and **T.C. Osborne**, 2020: Skill of rain-snow level forecasts for landfalling atmospheric rivers: a multimodel assessment using California's network of vertically profiling radars. *Journal of Hydrometeorology*, 21(4), 751-771, https://doi.org/10.1175/JHM-D-18-0212.1.

Ralph, F.M., and Coauthors 2019: ARTMIP-Early start comparison of atmospheric river detection tools: how many atmospheric rivers hit northern California's Russian River Watershed? *Climate Dynamics*, 52, 4973-4994, https://doi.org/10.1007/s00382-018-4427-5.

Shields, C.A., and Coauthors, 2018: Atmospheric River Tracking Method Intercomparison Project: project goals and experimental design. *Geoscience Model Development*, 11, 2455-2474, https://doi.org/10.5194/gmd-11-2455-2018.

FELLOWSHIPS

2020-2021	Dissertation Year Fellowship, University of California Office of the President
2020-2021	Katzin Endowment Fellowship
2016-2020	Graduate Research Fellowship, National Science Foundation
2015-2017	San Diego Fellowship, University of California San Diego

ABSTRACT OF THE DISSERTATION

Extreme Rain-Snow Level Variations during California Storms

by

Tashiana Chanté Osborne

Doctor of Philosophy in Oceanography

University of California San Diego, 2021

Arthur J. Miller, Chair
Joel R. Norris, Co-Chair
F. Martin Ralph, Co-Chair

Western U.S. residential, municipal, and agricultural water supplies depend on cool season storms. The majority of these storms are landfalling atmospheric rivers which travel in the troposphere from the tropical Pacific Ocean. Sudden changes in mesoscale features or storm ingredients can dramatically alter impacts affecting hydrologic processes and communities. Although storms provide vital water supplies, they also induce deleterious flooding, landslide, wind, and snow-related disasters. Precipitation phase and the type and severity of storm impacts vary depending on the altitude at which frozen hydrometeors melt relative to ground elevations. Thus, this rain-snow transition altitude, or atmospheric snow level, and its intrastorm vertical variations are key in determining storm benefits and hazards.

While there has been a considerable amount of recent progress in snow level research, there remain challenges regarding substantial changes in snow level observed during high-impact storms. The primary goal of this dissertation, therefore, is to provide a robust methodology to define, catalogue, and describe extreme intrastorm changes in snow levels during California storms. This work considers 10 vertically-oriented radar locations over six recent cool seasons, defining an *extreme snow level change* as a one-hour change with a magnitude of at least 400 meters. The provided dissertation identifies 134 and 113 extreme rises and falls, respectively, finding strong associations with periods of enhanced water vapor transport including atmospheric rivers. Additionally, this research designs data quality filters that reduce spurious snow level changes. This work also defines and identifies distinct events, termed *semicontinuous snow level events*, in which to compute hourly changes.

Further, this dissertation provides statistical, spatial, and temporal descriptions of semicontinuous snow level events, intrastorm snow level changes, and extreme changes. Results indicate an elevated number of extremes existed at northern sites, during December-March, and during anomalously wet cool seasons. Key findings reveal, for 60-100% of extreme changes at each radar, an atmospheric river occurred within the six hours preceding or following each extreme. Ultimately, this dissertation provides methodologies, findings, and a catalogue of extremes beneficial to future investigations of intrastorm snow level changes, atmospheric

mechanisms controlling these variations, and implications for hazard prediction and preparedness.

Chapter 1

Executive Introduction

1.1. Background

Water from rainfall and snowpacks is essential to sustain living creatures and ecosystems of Earth. At the same time, both an overabundance or absence of precipitation can lead to destruction. A number of interrelated factors involving the atmosphere, oceans, land, subsurface water and soil, and human activities determine precipitation type, intensity, location, duration, along with resultant hydrologic and societal impacts. Sudden changes in any precipitation-enhancing or inhibiting factor can result in disasters. Thus, there exists a fine line between hazards and benefits of precipitating storms. Scientists and communities have grappled with this truth throughout history, and face challenges with it today that are exacerbated by anthropogenic climate change.

Atmospheric rivers (ARs), previously referred to as tropospheric rivers, are a relatively new type of storm identified and investigated by researchers. Foundational work of the 1990s (Newell et al. 1992; Zhu and Newell 1994, 1998) contributed to considerable advancements in AR research and knowledge between the early 2000s and present (Gimeno et al. 2014; Ralph et al. 2017a). ARs are long, narrow corridors of elevated atmospheric moisture that typically form over tropical ocean regions and exist within the warm (pre-cold front) sector of an extratropical cyclone. This sector often features a low-level jet, a region of strong winds, which enhances moisture transport from tropical and extratropical source regions (e.g., Zhu and Newell 1998, Ralph et al. 2004, 2005, 2011; Bao et al. 2006; Wick et al. 2013; Dacre et al. 2015).

While ARs are relatively narrow (~600-1000 km wide), they are responsible for more than 90% of the water vapor transported poleward across midlatitudes (Zhu and Newell 1998). Thus, ARs play important roles in a wide range of challenges, including the development of reliable weather and flood forecasts and understanding the global water budget on weather and climate time scales (e.g., Ralph et al. 2004; Dettinger et al. 2011; Dettinger 2011; Gershunov et al. 2019). ARs simultaneously supply valuable water in the form of precipitation, and create weather and water hazards for regions across the globe (e.g., Waliser and Guan 2017; Payne et al. 2020). Recent studies examined impacts and characteristics of ARs affecting the western U.S., southern Africa (Blamey et al. 2018; Ramos et al. 2018), the Middle East (Dezfuli 2020), western South America (e.g., Viale and Nuñez 2011). Past studies also involved ARs in Europe (e.g., Lavers et al. 2012; Lavers and Villarini 2015; Ramos et al. 2015, 2016), the northern Pacific (Mundhenk et al. 2016; Kamae et al. 2017), the central and eastern U.S. (e.g., Moore et al. 2012; Debbage et al. 2017), Antarctica (Gorodetskaya et al. 2014; Adusumilli et al. 2021).

During California's storms, which are the focus of this dissertation, rain and snow in excess can result in natural hazards and negative societal impacts, from flooding and landslides to road closures and avalanches, all of which threaten lives and property. At the same time, as California produces the majority of various tree nuts, fruits, and vegetables grown in the U.S., its farming communities, economy, and consumers across the nation and world heavily depend on water from mountain snowpack and new precipitation during cool season storms. The majority of California's storms are landfalling ARs which provide up to 40-60% of annual precipitation (Dettinger et al. 2011; Rutz et al. 2014; Lamjiri et al. 2018) and up to 40% of snow water equivalent (Guan et al. 2010).

ARs that affect the western U.S. typically generate over the tropical Pacific Ocean near Hawaii or further west nearer eastern coasts of Pacific Islands and the continent of Asia (e.g., ; Sellars et al. 2017; Zhou and Guan 2018). They form as a result of interactions between the ocean surface and atmosphere involving strong evaporation and moisture convergence. These moisture plumes travel to the northeast or east towards land. Each exists within an extratropical cyclone which occurs during the cool season, typically near southern or western coasts of Alaska. Characteristics of the associated low-atmospheric pressure system and low-level jet (e.g., Demirdjian et al. 2020) involving magnitude, intensity, location, or variations over time affect corresponding impacts and characteristics of AR/s. Upon reaching the western U.S., ARs typically persist for 15-25 hours (e.g., Ralph et al. 2013a; Rutz et al. 2014). ARs extend through the lowest 3 km of the atmosphere, measuring 850 km wide, on average, and at least 1500 km long (Ralph et al. 2004, 2017b, 2018; Cordeira et al. 2013). Extreme precipitation, strong winds, floods, landslides, and avalanches can ensue from these ARs (e.g., Ralph et al. 2006; Dettinger 2016; Lamjiri et al. 2017; Hatchett et al. 2017a; Oakley et al. 2018; Cordeira et al. 2019).

The atmospheric rain-snow level, or the altitude at which frozen hydrometeors fully transition to rain, governs precipitation type during storms as well as resultant hydrologic responses and impacts for communities. Further, impacts of rain-dominated precipitation events can differ significantly from those of snow-dominated events. For instance, when rain-snow levels (hereafter referred to as snow levels) exist above the majority of ground elevations within a basin, the majority of the basin will experience rain which can quickly lead to flooding and mass movements. When, instead, snow levels are situated below ground elevations, most of the basin area will experience snow which can lead to avalanches and road closures and delays, or may be retained within a snowpack for a longer time period.

Additionally, hydrometeorologically high-impact basins within regions of steeply-varying ground elevation such as in California's Sierra Nevada ("snowy mountains"), are especially sensitive to snow levels and snow level variations over time. Further, storm-provided snowpacks and rainfall within these key regions such as the Sierra Nevada supply critical water for cities, farms, and ecosystems throughout the state. Thus, to predict and plan for distinct impacts of individual storms, it is important to explore and understand characteristics of snow levels and their intrastorm variations.

Following the discovery of the Doppler effect in the early 1840s, the discovery of radio waves in the late 1800s, and the invention of radars in the mid-1930s, radar profilers were designed and used to measure objects in the sky. In the 1940s and 1950s, as a result of radar advancements made during World War II, researchers began using radars to observe hydrometeors (Whiton et al. 1998; Saltikoff et al. 2019). Throughout the late 20th century and recent early 21st century, researchers have investigated spatiotemporal patterns, and physical and radar-observed characteristics of melting layer variables including California snow level. Researchers utilize vertically-oriented radars to detect snow levels which, through imagery of Doppler radar returns, appear as peak radar reflectivity heights (e.g., Austin and Bemis 1950; Battan et al. 1973; White et al. 2002; Johnston et al. 2017). These "brightband heights" result due to contrasting properties of rain and frozen droplets, largely diameter and water-to-ice ratio.

Past studies describe characteristics, spatial variations, and numerical weather model forecast skill for western U.S. snow levels and related variable within the melting layer (e.g., Stewart et al. 1984; Lundquist et al. 2008; Minder et al. 2011; Minder and Kingsmill 2013; Henn et al. 2020; White et al. 2010; Neiman et al. 2014; Hatchett 2018). In addition, previous research provides details on the sensitivity of streamflow responses to melting layer features (e.g., White et al. 2002; Neiman et al. 2014; Sumargo et al. 2020a). Recent studies have emphasized variations in snow levels over annual to decadal timeframes (e.g., Hatchett et al. 2017b), and spotlighted case studies of large-magnitude snow level changes occurring during a single AR event or across consecutive storms (e.g., Hatchett et al. 2016, 2020; White et al. 2019). While researchers have made important contributions to snow level research over time, there still remain unknowns surrounding the topic of substantial intrastorm snow level changes which are the focus of this dissertation (refer to Section 1.3 for an introduction to the dissertation).

1.2. Historical Context

While the numerous cultural histories and regional achievements of atmospheric and Earth sciences are beyond the scope of this dissertation, it is important to acknowledge and honor the invaluable contributions and the oral and written histories of those before us. By spotlighting a number of histories here, this section provides a broader, global perspective of precipitation-relevant ideologies and research advancements through time.

Across the ancient and present-day world, legends of hydrometeorological extremes in connection with deities or mythological beings have been passed down within Indigenous communities. For instance, West African Yorùbá goddess, Oshun (Ọṣun in ancestral Afro-Brazilian cultures), is traditionally said to unleash or withhold her waters when angered, causing floods or droughts. Similar beliefs have been shared by other communities existing across oceans and generations. Ancestral Hawaiian beliefs suggest the rain god, Lono-makua (Lono the Provider), supplies the archipelago with its wintertime rain. The Kumeyaay of present-day San Diego and Baja California, Mexico, include storm-bringing spirits in their ancestral stories (San Diego IRWM Program, 2017).

Long before the Spanish colonization of present-day California beginning in the 16th to 18th century, Indigenous communities depended on adapting to and understanding the interconnectivity of the sky, oceans, land, ecosystems, and Earth's beings. Much like other long-established groups across the world (e.g., Dube and Munsaka 2018; Zhang and Nakagawa 2018), Indigenous communities of the Sierra Nevada (the Kawaiisu, Mono, Northern Paiute, Sierra Miwok, Tübatulabal) and other California regions developed and applied ecosystem-based knowledge to establish best practices for sustainable living and for the management of land, livestock, and crops. This wisdom, which is still relevant today, has been used to increase community resilience during droughts, floods, and other natural hazards (e.g., Aldern and Goode 2014; Andrade-Sánchez et al. 2021). From ancient Egypt's goddess of moisture and rain, Tefnut (circa BCE 3200), to ancient Greece's god of the skies, Zeus (circa BCE 700), to spiritual beings that are part of Indigenous beliefs, countless communities throughout history share legends regarding rain sans destruction to be a gift from above.

In the oldest known comprehensive atmospheric science treatise (BCE 350), entitled *Meteorologica*, Greek philosopher Aristotle wrote about the interconnectivity of Earth's oceans, land, atmosphere, and rivers: "It is thought that the water is raised [from Earth's land and ocean surfaces] by the sun and descends in rain...[The rain] gathers below the earth and so flows from a great reservoir, all the rivers from one, or each from a different one." Over the lifetimes since pre-modern eras, researchers and communities continued investigating hydrometeorological processes and phenomena and documented their findings. Challenges in understanding and predicting features of the water cycle, and mitigating and preparing for storm-related hazards still exist today.

Prior to remote sensing, various instruments were invented and used within ancient and Indigenous communities to monitor the atmosphere and bodies of water. For instance, ancient Egyptians invented and used the nilometer to measure water height and clarity of the Nile River. Rainfall records from ancient Greece and India began circa BCE 500 and BCE 400, respectively. During 1441 in Korea, a rain gauge called the cheugugi was created to measure rain (Valipour 2020). Within the United Kingdom and post-colonization U.S., routine documentation of weather conditions did not begin until around the 1850s and 1870s, respectively, around when the British Meteorological Society (i.e., current Royal Meteorological Society) and the U.S. National Weather Service were established.

Since the early 20th century, scientists and engineers have worked to develop remote sensing instruments positioned on the ground, on airplanes, or on satellites in space. These instruments measure objects in the sky, including aircrafts and precipitation, as well as characteristics of bodies of water, and more. In 1842, Christian Johann Doppler formally described the Doppler effect which is used in modern-day radars to measure the speed of moving objects. In the late 1880s, Heinrich Hertz formally proved the existence of radio waves. It was not until the mid 1930s, however, that Sir Robert Alexander Watson-Watt led the design of the first operational radar system in Britain and the world. The British Royal Air Force used this system to identify aircraft during war. During the 1940s and 1950s, researchers made major developments in radar remote sensing (Whiton et al. 1998; Saltikoff et al. 2019). Much of the progress made in the U.S. and Europe stemmed from efforts to support or strengthen military operations during World War II. More recently, in the 1960s-1980s, the U.S. and European countries launched the first satellites which allowed scientists to measure features of Earth from space, including water in its gaseous, solid, and liquid forms (water vapor, ice, rain and snow) in the atmosphere, in oceans, and on land.

As a result of regional wisdom, the intergenerational sharing of knowledge, and through centuries of scientific and technological advancements, researchers and communities can measure, track, and elucidate details of water vapor and precipitation during ARs and other storms (as considered in this dissertation work) as well as hydrologic responses of rivers and streams. Advances in radar and satellite meteorology and technologies add value to society by allowing humans to observe features of the Earth and its atmosphere with enhanced breadth, accuracy, and precision. In turn, previous achievements and those of the future also allow for an elevated understanding of Earth's natural hazards, processes, and changes in a warming world.

1.3. Introduction to the Dissertation

The purpose of this dissertation is to develop the first robust definition, record, and analysis of *extreme intrastorm snow level changes* (magnitude ≥400 m within an hour) which have been observed during high-impact storms. These extremes are hereafter also referred to as extreme changes or extreme SLCs. Compared to previous studies, the research presented here includes an increased number of water years (six recent cool seasons) and California radar locations within a single radar network (10 total; consistent in design and operation).

Additionally, this dissertation work examines spatiotemporal patterns and characteristics of both extreme intrastorm rises and falls in snow level.

Overarching scientific questions include the following: (1) What methods can we create and apply for snow level event identification, data quality checks, intrastorm SLC computation, and the identification of extremes to define and catalogue valid extreme SLCs? (2) How might mean characteristics of extreme snow level rises and falls vary spatially, annually, and from one month to the next? (3) Do relationships exist between extreme SLCs and AR periods, or periods of enhanced water vapor transport?

We hypothesize anomalously wet winters and peak AR months (December-March) will have elevated counts and mean magnitudes for extreme snow level rises and falls. Additionally, we hypothesize extreme SLC counts and magnitudes will also exhibit a spatial dependence, with peak counts and magnitudes at radars located within typical frontal system penetration pathways or within regions that experience orographic precipitation enhancements. Further, we hypothesize strong associations between extreme SLC periods and high-moisture periods, in turn, meaning a strong association between extreme SLCs and ARs.

To begin, in Chapter 2, we employ high temporal resolution (10-minute) radar-derived snow levels to establish a methodology to identify *semicontinuous snow level events*. These events are defined through this dissertation as periods containing nearly-continuous snow levels which allow for data gaps due to the sporadic nature of precipitation. Next, we compute maximum one and three-hour snow level rises and falls within the predetermined semicontinuous snow level events. Further, to reduce spurious fairly-significant snow level changes (magnitude ≥ 200 m), we develop and apply quality check filters for radar-derived snow level measurements.

We compare the sensitivity of statistics for semicontinuous snow level events and intrastorm snow level changes pre- and post-quality check filters. Lastly, we assess patterns and statistics of intrastorm snow level changes and semicontinuous snow level events from one year, radar, and month to the next.

Chapter 3 expands on Chapter 2 by providing a definition and description of extreme intrastorm snow level changes. In Chapter 3, we establish and apply a percentile-based methodology to define and identify extreme rises and falls in snow level within the dataset of intrastorm snow level changes created in Chapter 2. Additionally, we investigate spatiotemporal patterns and statistics of extreme and exceptional (≥ 800 m within one hour) intrastorm snow level changes. Further, we explore associations between extreme snow level changes and ARs and integrated water vapor transport (IVT) values. To do so, we employ a high-resolution reanalysis product and an AR catalogue derived from an IVT-based detection algorithm. Both Chapter 2 and 3 include content-specific subsections of the scientific method. Chapter 4 includes concluding remarks involving broader implications of this dissertation. Lastly, in this final chapter, we suggest applications of this work for future studies of physical drivers and hydro-societal impacts of snow levels and extreme changes.

Chapter 2

A Methodology to Identify Intrastorm Changes in Radar-Derived Snow Level Elevation

2.1. Abstract

The elevation of the transition between rain and snow in the atmosphere is key for determining precipitation type, location, and hydrologic impacts. This transition, known as the atmospheric snow level, is particularly important in regions of complex terrain such as California's Sierra Nevada. Although abrupt snow level changes have been observed by vertically-oriented radars and contribute to substantial alterations in hydrometeor type and subsequent hydrometeorological impacts, these changes have not been comprehensively investigated. Here, we present a methodology to compute maximum hourly snow level changes, employing radar-derived snow levels during cool seasons spanning water years 2015-2020.

This study catalogues 1492 semicontinuous snow level events, defined as periods containing at least 50% available data lasting three or more hours with data gaps no longer than three hours. Within these semicontinuous events, intrastorm snow level rises and falls are computed and catalogued over one and three-hour increments. To minimize the number of invalid snow level changes, we develop and apply conservative data quality filters to existing measurements. Across all sites and years considered, the filters omit 2.8% of initial snow level measurements. We assess results by site, month, and year, finding peak counts for snow levels, semicontinuous snow level events, and intrastorm snow level changes at higher-latitude radars,

during March compared to other months, and during anomalously wet cool seasons including the record-setting 2017. This work provides a foundation for subsequent snow level studies investigating spatiotemporal variations, impacts, and driving mechanisms of intrastorm snow level rises and falls.

2.2. Significance Statement

In mountainous areas such as California's Sierra Nevada, the altitude where snow melts to become rain - the atmospheric snow level - is especially important. Snow level relative to ground elevation determines the fraction of the watershed experiencing snow or rain during a storm. Flood hazards resulting from rain or rain-on-snow differ considerably from snow hazards, and rapid vertical snow level changes can produce both rain and snow hazards simultaneously, depending on the location. Thus, we present a methodology to compute and investigate hourly rises and falls in radar-derived snow levels after removing spurious changes. This catalogue of snow level events and changes will be useful for subsequent studies examining hydrologic and societal impacts.

2.3. Introduction

Whether precipitation falls as rain or as snow plays a key role in determining the magnitude of storm hazards versus benefits. While rain replenishes reservoirs of the western U.S., sustained heavy or short-duration, high-intensity rainfall produces flooding and landslides (e.g., Ralph et al. 2006; Dettinger 2016; Oakley et al. 2018; Cordeira et al. 2019). New snowfall can increase mountain snowpacks that contribute to water supplies upon melting in warmer temperatures, but extremes lead to negative impacts such as traffic delays and avalanches (e.g., Hatchett et al. 2017a, 2020; White et al. 2019).

An important storm characteristic controlling hydrometeorological impacts in mountains is the snow level, defined as the elevation at which snow melts into rain. The snow level elevation relative to basin hypsometry determines the fraction of a watershed receiving snow versus rain. This elevation, also known as the rain-snow transition elevation, or rain-snow line, is especially important in regions with large (> 1000 m) elevation gradients. Freezing levels, or 0°C altitudes, are closely related to snow levels. Rather than representing a vertical temperature contour, snow levels represent the minimum altitude at which free-falling frozen hydrometeors melt entirely to rain. Whereas freezing levels exist at the top of the vertical layer where hydrometeors melt, snow levels lie further below, with an average difference of 192 m for coastal California (White et al. 2002).

California cool season snow levels typically occur between 1000 and 3500 m MSL with medians near 1500 m MSL (Hatchett et al. 2017b; Henn et al. 2020), a range that also encompasses ground elevations throughout much of California's Sierra Nevada, which has peaks at ~3300-4400 m MSL. The snow level can be deduced from radar brightband height, which is the elevation of peak reflectivity corresponding to the vertical melting layer (i.e., the bright band). Reflectivity peaks appear largely due to differences between the liquid-to-solid water ratio (which affects the dielectric constant) and the size of frozen hydrometeors and rain. Using vertically-oriented S-band radars, we can identify snow levels on short time scales (minutes to hours) during brightband-containing precipitation events. An hourly or sub-hourly rise or fall in snow level during a storm, which we refer to as an *intrastorm snow level change* (SLC), can alter the fraction of a basin that predominantly receives rain or snow. Such alterations can contribute to costly hazards to life and property and create water management challenges.

Previous studies examined characteristics, climatologies, or model forecast skill of western U.S. melting layer features (e.g., Marwitz 1983; Stewart et al. 1984; White et al. 2002, 2010; Lundquist et al. 2008; Minder et al. 2011; Minder and Kingsmill 2013; Neiman et al. 2014; Henn et al. 2020). Others considered annual and decadal-scale snow level variations (Hatchett et al. 2017b; Lynn et al. 2020), or case studies of single events containing SLCs (e.g., Hatchett et al. 2018, 2020; White et al. 2019). Within one winter (2016/17), Henn et al. (2020) found large variations (≥ 3000 m) in California snow levels at individual radar sites, suggesting that snow levels play an important role in determining precipitation and impacts for individual storms. Snow levels also exhibit spatial variability, with 5th percentile values up to ~500 m larger in southern regions compared to northern sites, and lower heights at coastal sites compared to inland locations at similar latitudes (Henn et al. 2020).

In excess of 40-60% of western U.S. cool season rain, snow, and the majority of precipitation variability results from landfalling atmospheric rivers (ARs; Dettinger et al. 2011; Rutz and Steenburgh 2012; Rutz et al. 2014; Dettinger 2016; Lamjiri et al. 2017, 2018). ARs are also important contributors to extreme precipitation which, depending on antecedent snowpack, soil moisture, and storm characteristics, can lead to high-impact hydrometeorological events (e.g., Guan et al. 2016; Sumargo et al. 2020b). Two recent high-impact precipitation events, the February 2017 Oroville Spillway Crisis (Hollins et al. 2018; White et al. 2019; Vano et al. 2019) and the February 2019 Valentine’s Day Event (Hatchett et al. 2020), both ensued from landfalling ARs and led to costly damages across California. Vertically-oriented radars observed large changes in snow level within one-hour periods in these events.

Prior findings emphasize the important role melting layer characteristics play in hydrologic forecasting and processes (e.g., White et al. 2002; Neiman et al. 2014; Sumargo et al. 2020a). For example, by performing a river forecast model simulation for a moderate single-day rain event, White et al. (2002) found an approximately 600 m rise in freezing level tripled peak flows at three northern California basins. In high freezing level events (> 2.3 km) and heaviest rainfall periods, the magnitude of negative freezing level forecast biases increases up to 900 m (White et al. 2010), emphasizing the challenges that numerical forecast models face in predicting bright band features during high-impact events. Hatchett et al. (2016) applied a 500-m minimum threshold to identify and assess six intrastorm (within ≤ 24 hours) snow level rises and linked the rises to midwinter peak runoff events in the northern Sierra. This previous study was limited to 2010-2014 at two radars and did not assess snow level falls.

Here, we provide the first robust computation and assessment of both rapid (one- and three-hourly) snow level rises and falls across 10 California vertically-oriented radars. We consider recent cool seasons spanning water years 2015-2020 which include two anomalously wet years, 2017 and 2019. These SLCs occur within what we define and identify as *semicontinuous snow level events*, or periods with nearly continuous snow levels and only brief data gaps. We also establish conservative snow level data quality check (QC) methods to minimize the number of invalid SLCs. To further increase reproducibility, we provide a data filter flow chart (refer to Table A.1) and develop a dataset for use in future studies of intrastorm SLCs and their drivers and impacts.

2.4. Data

Snow level heights (illustrated in Fig. 2.1) are provided by the Physical Sciences Laboratory (PSL) within the National Oceanic and Atmospheric Administration Earth System Research Laboratory (NOAA ESRL), the California Department of Water Resources (CA-DWR), and the Cooperative Institute for Research in Environmental Sciences (CIRES). In our study, we employ snow levels derived from 10 vertically-oriented Frequency-Modulated Continuous-Wave Snow Level Radars (FMCW SLRs, hereafter referred to as radars; Table 2.1, Fig. 2.2). NOAA PSL operates the radars and also designed, constructed, and deployed them, with funding provided by the CA-DWR (White et al. 2002; Johnston et al. 2017).

The radars operate within the S-band (2.835 GHz) which is ideal for measuring hydrometeor-size particles, especially when paired with FMCW capabilities. This frequency range is associated with reduced weakening of radar signals (attenuation) during heavier rain and improved accuracy above the boundary layer compared to larger or smaller ranges, respectively (e.g., White et al. 2000, 2002). Through the interagency Hydrometeorology Testbed Legacy Project, these radars were designed to be less costly and time-intensive than preceding wind profilers and S-band pulsed radars (White et al. 2013; Ralph et al. 2013b; Ray and White 2019).

Radar-derived snow levels are only available during brightband-containing precipitation periods, as often as every 10 minutes. Snow levels were identified using Doppler reflectivity (i.e., signal-to-noise ratio) and vertical radial velocity profiles pre-processed by NOAA through a NOAA and CIRES automated snow level detection algorithm, designed to reduce false alarms (White et al. 2002; 2003b). The algorithm identifies the snow level as the peak reflectivity altitude above the lower section of the bright band. Reflectivity begins increasing with height at the top of this lower bright band section; thus, the snow level is found in the upper section (refer to Fig. 2.1 schematic and Fig. 2.3a time series).

These FMCW radars operate with an ~8-10 km maximum vertical range and a 40-60 m vertical resolution. We initially consider all snow levels at all 10 radars during the cool season (1 October - 1 May) of water years 2015 to 2020. Radars are positioned near western Sierra Nevada foothills, southern Klamath mountains, and the central California coast. Five radars are situated along the northwest-to-southeast Sierra foothills transect, near high-impact basins which are key for California water supply and flood management (Table 1, Fig. 2.2). Sample size varies depending on the date of radar installation (Table 2.1). Additionally, there were periods when FMCW radars were not operational, most notably during the late December 2018-late January 2019 U.S. government shutdown.

2.5. Methodology

The goal of this algorithm is to conservatively estimate and understand occurrences of SLCs within impactful brightband precipitation events. Therefore, we begin by defining and identifying distinct time periods containing sufficient snow level measurements at each radar. We allow for data gaps of up to three hours due to the sporadic nature of snow occurrence, dubbing these periods semicontinuous snow level events. Next, we compute maximum one- and three-hour SLCs within each event. To minimize large-magnitude SLC false alarms, we developed data QC filters applied to snow levels prior to identifying events and while computing SLCs.

2.5.1. Defining Semicontinuous Snow Level Events

To identify and investigate intrastorm SLCs, we first establish a definition for semicontinuous snow level events. We consider stratiform precipitation events where the snow level detection algorithm identified a snow level (White et al. 2002). To be considered a semicontinuous snow level event, three requirements must be met. First, the time period must contain quality-controlled data for at least 50% of the 10-min time steps within the event. Second, the period may contain gaps in data lasting up to three hours. Lastly, the preceding requirements must be met for a total duration of at least three hours, including data gaps.

A three-hour minimum duration allows us to capture shorter events containing large SLCs that may be flanked by non-brightband precipitation periods not included here. The other requirements were established to allow for the inclusion of intermittent non-brightband and brightband precipitation periods (termed mixed precipitation by Neiman et al. 2005) occurring within a single event, rather than dividing these periods into multiple shorter-duration events. Figures 2.4a and 2.4b, for example, display three periods of time described as semicontinuous events during 6-10 February 2017 at Colfax. If data gaps between these events were shorter-duration, these periods may instead be grouped together as one or two events total. Our methods are informed by previous work (White et al. 2003a; Neiman et al. 2005) and by the fact that the majority of annual precipitation (59-82%) occurs during brightband precipitation (Neiman et al. 2005).

The dataset we construct captures only stratiform precipitation events containing brightband heights. By design, we also allow for intermittent periods of brightband and non-brightband precipitation, and brief periods when precipitation may cease (e.g., gaps in deeper seeder clouds above shallower feeder clouds). We do not consider non-brightband precipitation resulting from colder, solely snow-exclusive events (i.e., snow level below the ground surface), warmer and shallower rain-dominated events (i.e., warmer cloud echo tops situated beneath the snow level), or convective events where intensified turbulence complicates attempts to measure snow level.

2.5.2. Computing Rapid Snow Level Changes

For each semicontinuous snow level event, we employ a rolling 10-minute window when computing maximum one-hour SLCs in order to maximize the sample size for computed SLCs. We specifically target intrastorm SLCs that are more likely to alter hydrologic impacts resulting after the change compared to before. We identify a single maximum magnitude change (either a rise or fall) within each one-hour interval which can contain both positive and negative SLCs, and ultimately construct a dataset of maximum one-hour SLCs. For comparison, we perform the same process to compute maximum three-hour SLCs.

2.5.3. Quality filters for Snow Level Observations

To further minimize large-magnitude SLC false alarms, we developed quality check filters to apply to the initial snow level dataset. Intrastorm SLCs are considered erroneous if they are not clearly explicable by physical processes or sustained long enough to substantially alter hydrologic impacts. Through visual inspection, we found SLC beginning or ending heights typically lie near pre- or post-change elevations (i.e., within ± 300 m of one-hour SLC means, or ± 100 m of values within ± 30 min). Inspection also suggested that error-yielding, particularly anomalous snow levels, more often appear at low (rather than high) elevations (as seen in Fig. 2.4e). We performed multiple iterations of the following error-detection methods to maximize the number of realistic, sustained large SLCs while minimizing false positives. With this trade-off in mind, we remained conservative in constructing four QC filters (reference Table A.1). Although a snow level may be omitted through a particular filter applied before another, this does not mean an additional filter would not also identify the same error-yielding value.

Sometimes, isolated periods contain large changes in snow level, but return to pre-change snow level heights within an hour. These events are not identified as SLCs since they suggest the brightband precipitation period was too brief to substantially affect event-total precipitation type or intensity, or streamflow. We developed and applied the first two data filters (1a and 1b) to catch these short-lived, fairly substantial changes in snow level (≥ 200 m magnitude) that are subsequently reversed, thus appear as peaks dissimilar from surrounding values. We applied a third data filter (2) to identify snow level observations (note: not SLCs) surrounded by dissimilar or nonexistent values. Additionally, we included a fourth filter (3) to avoid computing SLCs falling at the very beginning or end of a semicontinuous snow level event. To prepare for Filters 1a and 1b, we computed the highest-resolution SLCs possible within the raw snow level dataset, i.e., down to 10-min changes if data allow (or up to one-hour changes). If an SLC is computed but is surrounded by nonexistent values for one hour or longer on both sides, it is excluded.

Filter 1a: We observed snow level falls of approximately 1000 m (or greater) in magnitude occurring within short periods of time (one hour or less) followed by rises to the original snow level height within an hour’s time, as seen at New Exchequer Dam on 2 March 2018 around 1:30 UTC (Fig. 2.4e). Similar examples are seen during the 2-11 February 2017

Oroville Dam Spillway Emergency (Figs. 2.4c and 2.4d), and following the large snow level rise identified at Oroville and New Exchequer Dam during the 2019 Valentine's Day Event (Figs. 2.3c and 2.3d, respectively). In these cases, the anonymously low or high snow level heights were only measured during one to four timestamps (i.e., 10-40 min).

To address these error-yielding measurements, we created Filter 1a to eliminate instances wherein a snow level measurement appears as a short-lived peak (as part of a fairly substantial SLC) that differs considerably from surrounding values and is only sustained for a brief period of time. Further, this step implicitly pinpoints snow levels surrounded by nonexistent or missing measurements (explicitly addressed by Filter 2). To do so, the algorithm omits the beginning (and/or ending) height of a fairly substantial SLC if it falls outside the ± 300 m range of the mean for the one hour preceding and/or one hour following the change. Because this step yields medians that are similar to means, and snow levels are fairly evenly distributed about the mean (Gaussian), we consider means. When there exist fewer than two snow level measurements for which to compute a mean both before and after an SLC, we do not further assess the SLC in this step. If the algorithm determines the SLC beginning snow level, for instance, falls outside the allowable range, it omits the beginning height. When the algorithm can only compute a mean on one side, it also omits the additional measurement included on the side without a mean. After processing the beginning height of the SLC, we consider the ending measurement using the same method.

Filter 1b: There also exist semicontinuous snow level events in which additional short-duration, anomalously low or high snow level peaks were measured. For example, single-value peaks (one timestamp) can be seen at Oroville and New Exchequer Dam during the 2019 Valentine's Day Event (Figs. 2.3c and 2.3e) and during every event shown in Figure 2.4.

We omit these remaining cases where a fairly substantial SLC is short-lived and contains snow levels that are dissimilar from surrounding measurements. Filter 1b eliminates the beginning (and/or ending) height of an SLC if the radar does not measure at least one similar snow level height (within ±100 m) within ±30 min of the beginning (or ending) SLC height.

Filter 2: If neither the six-hour period preceding or following a snow level measurement contains an additional measurement within ± 100 m, we omit the assessed snow level. Filter 2, for instance, eliminates the final snow level at Saint Helena during the 2019 Valentine's Day Event as it falls in the category described above (Fig. 2.3e). Similarly, this filter eliminates snow level heights measured at Colfax around 11:00 UTC on 9 February 2017 (during a gap between semicontinuous snow level events identified after applying QC filters; Figs. 2.4a and 2.4b).

Filter 3: Finally, we also exclude SLCs that occur at the beginning or end of a semicontinuous snow level event, and contain pre- or post-SLC snow level periods of insufficient durations (too brief). For instance, by initiating computation at the 40-minute mark, the algorithm avoids capturing the large snow level rise at the beginning of the 9 February 2017 Saint Helena semicontinuous snow level event (Fig. 2.4f). Another example appears at San Bernardino on 13 March 2020 (not shown) when the snow level rises approximately 500 m during the last 40 minutes of the semicontinuous snow level event. As this SLC occurs at the end of the event and is not followed by a period of brightband precipitation, it is less likely to contribute to precipitation phase changes compared to an SLC sustained for longer than 30 minutes. To exclude these and additional SLCs that occur at the very beginning or end of an event, we constrain the window over which to compute intrastorm SLCs within semicontinuous events. Specifically, we initiate SLC computation after 30 minutes following the start of the event (i.e., the 40-minute mark) and finish 30 minutes before the last one-hour window (1.5 h before the event end).

Through data filters, we intentionally designed the algorithm to avoid capturing large-magnitude changes that were not sustained long enough to contribute to marked differences in the precipitation type and hydrologic impacts expected before and after the change. When discussing results below, we refer to post-QC snow levels and SLCs unless otherwise noted.

2.6. Results and Discussion

2.6.1. Distribution of Snow Levels

Quality-controlled snow levels for all radars and cool seasons (Fig. 2.5) follow a normal distribution about a mean value of 1790 m MSL (Table 2.1), with ~53% of all observations measured at the five key radars. Approximately 46%, 54%, and 0.05% of snow levels are higher than, lower than, or equal to the mean, respectively. Snow levels range in height from a minimum of 215 (pre-QC) or 235 (post-QC) m MSL to a maximum of 4102 m MSL (Fig. 2.5). The median and standard deviation for all snow levels (post-QC) are 1,712 m MSL and 665 m, respectively (Fig. 2.5, Table 2.1). These California snow level statistics are consistent with those of previous studies (Hatchett et al. 2017b; Henn et al. 2020).

Both pre- and post-QC, ~72% of snow levels exist within the same elevation range (1000-2500 m MSL; Fig. 2.5). Additionally, both pre- and post-QC, peak occurrences (up to 5400 measurements) appear within the two bins between 1100 and 1300 m MSL. Meanwhile, fewer than 100 measurements occur within bins near either tail of the distribution (i.e., bins < 500, or > 3500 m MSL; Fig. 2.5). We find maximum counts for omitted values (~150-200 total) within 100-m bins between 500 and 1800 m MSL (Fig. 2.5). Overall, only 2.8% of radar-derived snow levels are omitted (Figs. 2.5-7), meaning the NOAA ESRL and CIRES snow level detection algorithm performs well and, as intended, greatly limits the number of invalid snow level measurements (White et al. 2002, 2003b). By establishing and applying additional QC steps, however, we identify and omit snow levels contributing to large SLC false alarms which is a key objective for our study.

2.6.2. Summary of Semicontinuous Snow Level Events

Across all radars and cool seasons, we find a total of 1492 semicontinuous snow level events after QC filters are applied (Fig. 2.8; refer to Section 2.5.1 for details on event identification). Prior to applying QC filters, we identify 1490 semicontinuous snow level events. This increase from 1490 (pre-QC) to 1492 (post-QC) final events is the result of a few possible factors which can slightly alter the number and duration distribution of semicontinuous events before and after applying QC methods (Fig. 2.8). Short-duration events may be eliminated as they no longer fulfill requirements. Longer-duration events may either be eliminated, truncated, or split into two or more shorter events.

The data availability requirement aids in isolating only events containing more continuous snow levels while simultaneously omitting periods containing sparse measurements. Ultimately, the number of post-QC events is reduced from 1954 to 1492 (or from 2080 to 1490 for pre-QC measurements) as a result of requiring a data availability minimum of at least 50%

for each event. We find a median event duration of 8.3 (post-QC) or 8.7 h (pre-QC) and maximum of 77 or 94 h, respectively (Fig. 2.8). Only ~10% of the events persist for longer than 24 hours (near the 90th percentile). Approximately 75% of events have a duration between three and 15 hours during both pre- and post-QC steps.

Inland and northern sites (Happy Camp, Shasta Dam, Oroville, Colfax, New Exchequer Dam, Pine Flat Dam) have slightly larger post-QC median events durations (~8.2-10.2 h) than southern and coastal sites (~7-7.8 h; not shown). The previously identified latitudinal dependence of snow levels (Fig. 2.7a) also appears when assessing semicontinuous snow level events. The northernmost four radars contain the largest number of semicontinuous events - from north to south: max of 287 at Happy Camp, 211 at Shasta Dam, and ~180 at both Oroville and Colfax. Other radars contain between a minimum of 84 (Saint Helena) and a maximum of 134 (New Exchequer Dam) events. The descending order of semicontinuous event counts across all radars by cool season (not shown) is the same as that of snow level counts (Fig. 2.7b), with a peak in 2017 (341 events), the wettest year on record, and a minimum (182) in 2015, one of the driest cool seasons on record (Fig. 1 of Durand et al. 2020). A slightly longer-duration median results for 2017 (9 h) compared to other cool seasons (7.8-8.3 h medians).

As is consistent with the number of snow level measurements from one month to the next (Fig. 2.7c), fewer semicontinuous events occur during the beginning and end of the cool season. For instance, only 74, 169, and 155 events are seen in October, November, and April, respectively, compared to midseason counts ranging from a minimum of 228 to a maximum of 331 in February and March, respectively. Results align with previous studies which identify December through February or March as a period of maximum total precipitation (e.g., Fig. 1c of

Jong et al. 2016), extreme precipitation (e.g., Fig. 1 of Dong et al. 2019), and atmospheric river (AR) frequency (e.g., Fig. 6 of Rutz et al. 2014) in California.

2.6.3. Distribution of Snow Level Changes

As for intrastorm SLCs, we find 71,332 and 65,085 one- and three-hour SLCs, respectively (Fig. 2.9), using rolling 10-minute computation periods. There is a slightly smaller percentage of snow level falls (46% and 45% of all one- and three-hour SLCs, respectively) compared to rises. Nevertheless, we find the SLC distribution skewed slightly towards negative values with medians (i.e., 50th percentiles) of -32 and -81 m for all one- and three-hour SLCs, respectively (Fig. 2.9). Median magnitudes for -SLCs and +SLCs separately are similar to one another; -95 and 91 m for one-hour SLCs, and -186 and 174 m for three-hour SLCs, respectively (not shown). These medians are also larger than medians for SLCs of both signs together.

As the time increment over which SLCs are computed increases from one to three hours, percentiles also increase. For example, 90th percentiles for three-hour SLCs (383 and -376 m) are of slightly larger magnitudes than 98th percentiles for one-hour SLCs (361 and -319 m), 22 m larger for +SLCs and 57 m larger for -SLCs (Fig. 2.9). Approximately 90% of one-hour SLCs fall between -200 and 200 m (Fig. 2.9). Meanwhile, only 57% of all three-hour SLCs exist within the same range. Within the -50 to 50 m SLC subrange, there is a reduction in occurrences compared to surrounding 50-m bins which is especially noticeable for three-hour SLCs (Fig. 2.9b). Resultant 95th, 98th, and 99.5th percentiles are notably larger for +SLCs than for -SLCs (magnitudes 9, 42, and 168 m larger, respectively, for one-hour +SLCs compared to one-hour -SLCs, and 18, 78, and 142 m larger, respectively, for three-hour +SLCs compared to three-hour

-SLCs). This means intrastorm -SLCs must exceed reduced minimum SLC magnitudes (compared to larger minima for +SLCs) to be considered anomalously large or extreme.

2.6.4. Spatial Variations: Snow Levels and Snow Level Changes

Assessments of snow levels suggest the total number of (up to 10-minute) measurements is latitudinally-dependent, with three to more than four times as many observations at northern Happy Camp (20,404) within the Klamath Mountains compared to southern sites, Pine Flat Dam, Kernville, and San Bernardino (Fig. 2.6a; Fig. 2.2). This result is consistent with results in Henn et al. (2020) in which southern and near coast sites contained fewer brightband periods (six-hour periods) compared to profilers further north.

Overall, northwestern and northern regions of California typically experience larger cool season precipitation totals than southeastern or southern locations. Key factors contributing to elevated precipitation amounts in northwestern regions involve more frequent high-moisture ARs (e.g., Guan and Waliser 2015; Ralph et al. 2019a) and longer-duration ARs (e.g., Rutz et al. 2014; Gershunov et al. 2017). Additionally, precipitation enhancements through orographic lifting along windward slopes of the Sierras (as depicted in Fig. 2.1), Klamath Mountains, Coast Ranges, and other orography play a role in increased precipitation totals near west-facing slopes (e.g., Smith 1979; White et al. 2003a; Dettinger et al. 2004; Smith et al. 2010). Finally, higher-latitude regions maintain cooler temperatures as do higher-elevation regions (i.e., many of the radars in northern California are situated within mountainous regions at varying elevations).

Thus, northern radars may be more likely to experience precipitation during which snow levels can be deduced. On the other hand, radars will not measure a bright band if all precipitation is falling as snow which is more likely at northern and high-elevation sites. Another example of non-brightband precipitation occurs during periods that solely contain rain which are typical for warmer temperature profiles at southern sites. Additionally, parcel-environment instabilities can create high-turbulence convective events which make it difficult for radars to isolate snow levels - e.g., within regions and periods where atmospheric fronts travel, where parcels are forced upwards by steep terrain, or where near-surface altitudes warm substantially relative to layers above. The frequency of occurrence for each of these scenarios is beyond the scope of this study, but could be addressed in future work.

Snow levels nearer the coast (San Luis Reservoir and Saint Helena radars) are similar to those at southern sites, with an overall minimum at Saint Helena (Fig. 2.6a). San Bernardino contains the largest number and percentage of omitted snow level measurements, 624 omitted values or 9% of site-total values, while all other radars resulted in less than 5% of site-total values omitted. Of relevance, considerably larger freezing level forecast errors existed for San Bernardino compared to other California sites in a recent study, potentially due to larger forecast errors in timing and location of southern California ARs (Henn et al. 2020). The dataset we present in our study provides insights for diagnostic forecast error evaluations, and we echo previous recommendations centered on investigating mechanisms lending to these errors in future studies.

Snow level heights measured at any particular radar can vary widely, with 96% of snow levels falling within a 2000-3000 m-wide range for each radar (Fig. 2.7a). This result is consistent with findings of Henn et al. (2020) wherein wide variations in snow level height at a single radar site were also emphasized. An overall minimum of 235 m MSL (Saint Helena) and maximum of 4102 m MSL (New Exchequer Dam) result. The majority of snow levels fall within the 800 to 2500 m MSL range across multiple radar locations (Fig. 2.7a). Snow levels at San Bernardino and Kernville, however, are positively skewed towards lower ranges (~1000-1500 m MSL).

As also noted by Henn et al. (2020), median snow levels increase with decreasing latitude from Happy Camp southward to New Exchequer (refer to Fig. 2.7a for distributions by radar, Fig. 2.2 for the map, Table 2.1 for site information). Nearer-coast radars (San Luis Reservoir and Saint Helena) experience elevated medians (2058 and 1928 m MSL, respectively) similar to those of their downstream neighbors (New Exchequer Dam and Colfax). Meanwhile, southern inland sites (Pine Flat Dam and two southern radars positioned at higher ground elevations, Kernville and San Bernardino) exhibit lower medians (between about 1500 and 1800 m MSL) similar to those of the northernmost three sites.

As observed for snow level measurements and semicontinuous snow level events, sample sizes for intrastorm SLCs (total counts as well as +SLC and -SLC counts separately) are elevated for northern and Sierra radars compared to all other locations (Fig. 2.10a-b). Overall, fewer +SLCs result compared to -SLCs; 32,643 (one-hour) and 29,328 (three-hour) +SLCs compared to 38,689 (one-hour) and 35,757 (three-hour) -SLCs when considering 10-minute rolling intervals during SLC computation. Recall, this rolling interval means, within a two-hour time window, up to seven (rather than only two) one-hour maximum SLCs can be computed.

Medians computed using all SLCs largely skew negative, between -5 and -53 m MSL for one-hour SLCs, and -58 and -135 m MSL for three-hour SLCs. Exceptions appear for Shasta Dam where medians of 6 and 70 m MSL result for one- and three-hour SLCs, respectively, and for Oroville for three-hour SLCs only (median: 75 m MSL). One-hour SLCs medians (both positive and negative) negatively increase in magnitude southward from Shasta Dam (6 m MSL) to Kernville (-53 m MSL; Fig. 2.10a). A nearly similar trend is observed for one-hour +SLC medians, but not for one-hour -SLC values or three-hour +SLC or -SLC medians (Figs. A.2 and A.3; subplots a-b). When separately assessing medians for +SLCs and -SLCs by radar, values fall within the 80-113 m magnitude range and the 164-202 m range for one- and three-hour SLCs, respectively. Key differences between results of +SLCs and -SLCs by radar appear when examining the vertical spread as well as the 98th and 99.5th percentiles of SLCs which are, minus a few exceptions, larger for +SLCs compared to -SLCs.

The two widest ranges of one-hour SLCs result for San Luis Reservoir and Colfax with differences of 9850 and 9469 m, respectively, between the 0.5th and 99.5th percentiles for all SLCs (Fig. 2.10a). This result also holds true for three-hour -SLCs. Radars exhibiting maximum vertical spreads differ when considering only one-hour -SLCs (San Luis Reservoir and San Bernardino), one-hour +SLCs (Colfax and Saint Helena), three-hour +SLCs (Saint Helena and New Exchequer Dam, with Colfax as a close third), or all three-hour SLCs (San Bernardino and Colfax). In summary, central Sierra Nevada foothills sites (Colfax and New Exchequer Dam), southern-inland San Bernardino, and the two nearer-coast sites (Saint Helena and San Luis Reservoir) exhibit the most variability in terms of SLC magnitude.

2.6.5. Interannual Variations: Snow Levels and Snow Level Changes

The peak snow level count (21,681) appears during the record-wet 2017 cool season (Fig. 1 of Durand et al. 2020). This value is considerably larger than counts for the other five cool seasons which range from ~10,000 to ~16,000 (Fig. 2.6b). Minimum counts occurred during the 2015 cool season, when snowpack was 5% of normal (CA-DWR 2015).

Snow level height distributions also vary from one year to the next (Fig. 2.7b), although medians do not vary as widely as when assessed across radars (Fig. 2.7a). The maximum and minimum median snow level heights were experienced during the warmer-skewed 2015 and the cooler 2020 season, respectively (486 m lower for 2020; Fig. 2.7b). Snow level distributions and percentiles for 2016 and 2019 are noticeably similar (Fig. 2.7b) although 2019 contains nearly 1020 fewer measurements (Fig. 2.6b). Unlike during other years, the 2018 distribution appears bimodal (Fig. 2.7b). We hypothesize that median snow levels are bound to median characteristics of temperature and precipitation for each year. While our time series is not long enough to identify specific trends, we note that Hatchett et al. (2017b), which considers a longer time series (2008-2019), finds overall increases in median snow level corresponding with decreases in Sierra snowpack.

Results suggest radars that receive more cool season stratiform precipitation overall (to the north, or upwind of mountains) are more likely to dominate a snow level height distribution (refer to Fig. 2.6a and distributions shown in Figs. 2.7b-c). For instance, during the 2017 cool season, the percentage contribution decreased from 25% at northern Happy Camp to 12-13% at Shasta Dam, Oroville, and Colfax (not shown; refer to Fig. A.1a statistics). This percentage continues to drop from 9% to 5% from New Exchequer Dam southward to San Bernardino. Meanwhile, near-coast San Luis Reservoir contributed 7% of snow level measurements that year while Saint Helena contributed 4%. Contribution percentages for all other years follow a similar pattern, with 2015 exhibiting the largest spread overall (i.e., standard deviation and range; Fig. A.1a).

For intrastorm SLCs collated by year, results mimic snow level count trends. Cool seasons 2017, 2016, and 2019 contain the largest number of both one-hour -SLCs and +SLCs (Figs. 2.10, A.2, A.3, subplots c-d). These three years also experience peak three-hour SLC counts. As noted when examining SLCs by radar (Figs. 2.10, A.2, A.3; subplots a-b), the SLC magnitude range as well as the 98th and 99.5th percentiles are all notably larger for +SLCs compared to respective -SLC values (Figs. 2.10, A.2, A.3, subplots c-d).

2.6.6. Seasonality: Snow Levels and Snow Level Changes

We find the maximum snow level count (18,983) appears in March (Fig. 2.6c). Percentages of omitted snow levels peak during October and April (both ~5%), during the beginning and end of the wet AR season when post-QC snow level counts are minimal (Fig. 2.6c). At the same time, October experiences the highest median snow level height (2430 m MSL) and the largest number of relatively high snow levels (i.e., within the 2700 to 3200 m MSL range; Fig. 2.7c). Medians between November and April fall within a narrower range of values, ~1500 (March) to ~1800 m MSL (November and December). Wider ranges for snow level heights exist for both October and April (Fig. 2.7c), while around 96-98% of snow levels during the five midseason months lie between ~700 and 3100 m MSL.

Happy Camp dominates the snow level dataset for October with a contribution percentage of 40% compared to reduced percentages at northwestern (8-13%) and central (2-13%) Sierra foothills sites (not shown; refer to Fig. A.1b statistics). October also has the largest standard deviation and range for contribution percentages. For all other months, contribution percentages from Happy Camp southward to Colfax (approximately 12-25% each) exist within a narrower range of values while all other radars result in percentages of approximately 10% or less.

Results for SLCs are similar to those for snow level measurements. Mid-cool season months provide considerably more SLCs compared to October, November, and April (Figs. 2.10, A.2, A.3; subplots e-f). Findings are consistent whether considering one-hour or three-hour SLCs, or assessing +SLCs, -SLCs, or all SLCs together. The widest range of all one-hour SLCs, defined as the largest difference between 0.5th and 99.5th percentiles, occurs in February (Fig. 2.10e-f). All other analyses of SLCs by month result in a maximum SLC range during February, except when assessing one-hour -SLCs and three-hour -SLCs. In these cases, November and October, and January and November, respectively, exhibit the widest SLC ranges (Figs. 2.10, A.2, A.3; subplots e-f). Median SLC magnitudes do not differ considerably from one month to the next within a single grouping of SLCs (note the six SLC groupings depending on sign and time increment). Medians do, however, differ across SLC groupings, falling within a -46 to -28 m MSL range for all one-hour max SLCs compared to slightly narrower ranges containing larger-magnitude medians for one-hour +SLCs (88 to 98 m MSL) and -SLCs (-101 to -90 m MSL). Larger-magnitude medians are observed for three-hour SLCs (all three-hour SLCs: -103 to -61 m MSL, three-hour +SLCs: 164 to 187 m MSL, three-hour -SLCs: -202 to -177 m MSL). Wider median ranges are also observed for three-hour SLCs (~23-40 m-wide versus ~8-18 m-wide for one-hour SLC groupings).

Past studies suggest months during the end and beginning of the cool season (Apr-Mar, Nov-Oct) experience the smallest number of calendar days exhibiting AR conditions of all strengths; each month featured 6-10% of all AR days between January 1980 and April 2017 (Fig. 7 of Ralph et al. 2019a). Meanwhile, December experienced the most AR days, containing nearly 18% of the total. Similar conclusions regarding AR seasonality for California sites are drawn from Fig. 6 of Rutz et al. (2014) (October was not included in this previous study). Further, although analysis of snow level-influencing mechanisms is reserved for ongoing work, previous studies have shown atmospheric modes of climate variability and sea surface temperature anomalies influence precipitation and AR characteristics (e.g., Mock et al. 1996; Guan et al. 2013; DeFlorio et al. 2013, 2018; Guan and Waliser 2015; Mundhenk et al. 2016; Payne and Magnusdottir 2014; Kim et al. 2017; Jong et al. 2016; Guirguis et al. 2018; Bartusek et al. 2021). Smaller-scale influences, including local thermodynamic processes (e.g., White et al. 2010; Raymond et al. 2017; Hatchett et al. 2020), Sierra barrier jets (e.g., Lundquist et al. 2010; Neiman et al. 2013), fronts and cutoff lows (e.g., Abatzoglou 2016), and Rossby wave breaking events (e.g., Ryoo et al. 2013; Hu et al. 2017), can also contribute to precipitation, AR, and snow level characteristics.

We suggest future examinations would benefit from emphasis on influences of atmospheric mechanisms of various scales on vertical temperature structure and precipitation, thus affecting snow level and intrastorm SLC characteristics. Detailed investigations may prove helpful as these atmospheric and oceanic features interact complexly with one another and can vary in terms of magnitude, location, and implications depending on the year, season, and region of interest. In future work, we will consider such mechanisms with emphasis on ARs.

2.6.7. High Impact Snow Level Changes at Sierra Nevada Sites

In mid-February 2019, much of California experienced a high-impact snow level oscillation event associated with a strong AR (Hatchett et al. 2020). Similarly, a series of ARs brought heavy rainfall in February 2017 which, combined with water stored in a pre-existing snowpack and spillway structural challenges, resulted in an evacuation order for nearly 188,000 nearby residents, and over one billion U.S. dollars over two years for repairs (Henn et al. 2020; White et al. 2019; Vano et al. 2019). Snow level time series from multiple radars for each of these events confirms the snow level height dropped or rose on the order of several hundred to over 1,000 meters within one to three-hour time periods (Figs. 2.3, 2.4c-d).

There were multiple, sizeable SLCs (magnitudes ≥ 300-800 m within one hour) computed during the 2019 Valentine's Day Event at various radars including Colfax, New Exchequer Dam, and Saint Helena (Fig. 2.3). At Colfax, a one-hour snow level rise from near 1200 m MSL to ~2800 m MSL (initially sustained for 3.5 hours) occurred between 9:05 and 10:05 UTC on 13 February 2019 (Figs. 2.3a-b). The elevated height is sustained for three hours before a 1568 m-magnitude extreme fall occurs, positioning the snow level at an altitude within 200 m of its pre-rise altitude (near 1350 m MSL). After nearly two hours elapsed at the lower altitude, another two sizeable rises occur in succession (+1079 m and +426 m, respectively), boosting the snow level to an elevated height similar to that of the first large rise (2260-2600 m MSL). Snow levels remain near this elevated altitude range (climbing to a maximum of 3000 m MSL) for the remaining nearly 19-hour duration of the semicontinuous snow level event, with the event spanning almost 30 hours total.

For New Exchequer Dam, a large snow level rise of similar magnitude occurs during the same time as the initial rise shown at Colfax, but no additional large SLCs are detected (Fig. 2.3d). The fact that only one large SLC is detected here is a direct result of applying conservative methods when eliminating erroneous snow level values and defining semicontinuous events in order to minimize false positive large SLCs. In this case, the notably lower snow level altitudes observed between 12 and 13 UTC on 13 February 2019 following the mega-rise are not sustained for long enough (< one hour) to substantially alter precipitation or hydrologic impacts. Additionally, unlike for Colfax, post-snow level rise measurements are situated 600 to 800 m lower than initial snow levels before the mega-rise (~1400 m MSL). Thus, the encompassing semicontinuous event is truncated to a shorter period, seven hours, where no gaps exceeding three hours exist and at least 50% of remaining observations are available (Fig. 2.3d). Notably large SLCs were also computed at other key Sierra sites including Oroville (Fig. 2.3c) and Shasta Dam during this event (summary provided by Hatchett et al. 2020). In Sections 2.6.1 through 2.6.3, we showed these events are representative of the magnitude and spatiotemporal differences that can exist in snow levels and SLCs within the radar network. For ongoing and future work, we propose using the SLC datasets created here to investigate dynamical origins and impacts (e.g., runoff) associated with particularly large or extreme intrastorm SLCs.

2.7. Acknowledgements

Collaborators on material presented within this dissertation chapter include Joel R. Norris, Anna M. Wilson, Benjamin J. Hatchett, F. Martin Ralph, and Brian Henn. Chapter 2, in part, is being prepared for submission for publication as: Osborne, T.C., J.R. Norris, A.M.

Wilson, B.J. Hatchett, F.M. Ralph, and B. Henn. The dissertation author was the primary investigator and author of this material. Authors thank NOAA ESRL, CA-DWR, and CIRES personnel for providing valuable snow level measurements. We are grateful to Allen White of NOAA ESRL for elucidating details of radar-derived snow levels. We also thank Peter Yao of the Center for Western Weather and Water Extremes (CW3E) for providing the Valentine's Day event Doppler radial velocity time series. Lastly, authors express appreciation for the support of NOAA California Nevada River Forecast Center affiliates including Art Henkel and Rob Hartman, Art Miller and Myrl Hendershott of SIO at UC San Diego, and Amin Dezfuli of NASA Goddard Space Flight Center.

2.8. Data Availability Statement

For this study, snow levels derived from detection algorithm-processed radar observations (White et al. 2002, 2003b) were retrieved from NOAA: ftp://ftp1.psl.noaa.gov/psd2/data/realtime/RadarFMCW.

2.9. Figures and Tables

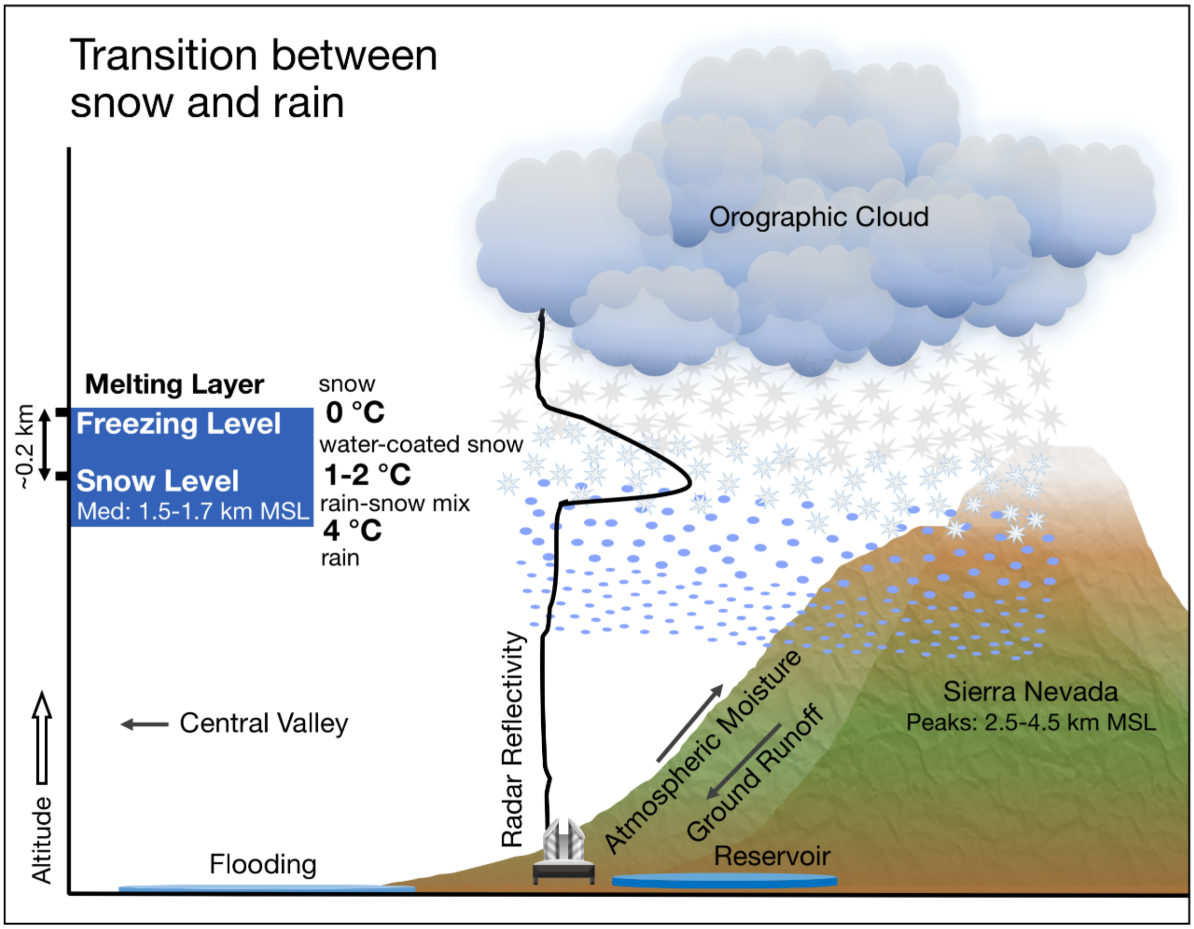

Figure 2.1. Schematic illustration of the melting layer as a hypothetical high-moisture storm penetrates inland from east to west (left to right) reaching Sierra slopes. A vertically-pointing radar is included with its reflectivity profile, along with typical precipitation types, atmospheric temperatures, and hydrometeors. A range of climatological medians for California snow levels is shown beneath the snow level. Altitude is depicted along the vertical axis (not to scale).

Table 2.1. Information on the 10 FMCW S-band profiling radar sites providing 10-minute resolution snow level observations during precipitation events in this study. Five key radars positioned within or near hydrologically high-impact basins are shown in boldface text. Details were obtained from NOAA PSL's Profiler Network Data and Image Library (https://psl.noaa.gov/data/obs/datadisplay/).

Site Name	Site Code	Latitude	Longitude	Elevation (m MSL)	Install Date	Total Days of Observations	Snow Level Median (Mean) (m MSL)	Snow Level Standard Deviation (m)
Happy Camp	hcp	41.79	-123.39	366	02 Feb 2012	141.7	1521 (1600)	639
Shasta Dam	**std**	40.72	-122.43	202	09 Dec 2009	89.3	1572 (1650)	613
Oroville	**ovl**	39.53	-121.49	114	08 Dec 2011	72.4	1767 (1793)	640
Colfax	**cff**	39.08	-120.94	644	10 Dec 2008	75.5	1858 (1905)	587
New Exchequer Dam	**ner**	37.60	-120.28	259	03 Dec 2010	51.0	2024 (2021)	727
Pine Flat Dam	**pfd**	36.83	-119.33	184	06 Dec 2010	42.0	1762 (1835)	651
Kernville	knv	35.75	-118.42	816	02 Jan 2012	34.3	1793 (1938)	596
San Bernardino	sbo	34.20	-117.34	602	12 Mar 2013	43.6	1572 (1772)	673
San Luis Reservoir	slr	37.06	-121.07	81	02 Apr 2013	44.0	2058 (1998)	704
Saint Helena	sth	38.55	-122.49	135	09 July 2014	29.7	1928 (1907)	743
All 10 Radars						623.7	1712 (1790)	665

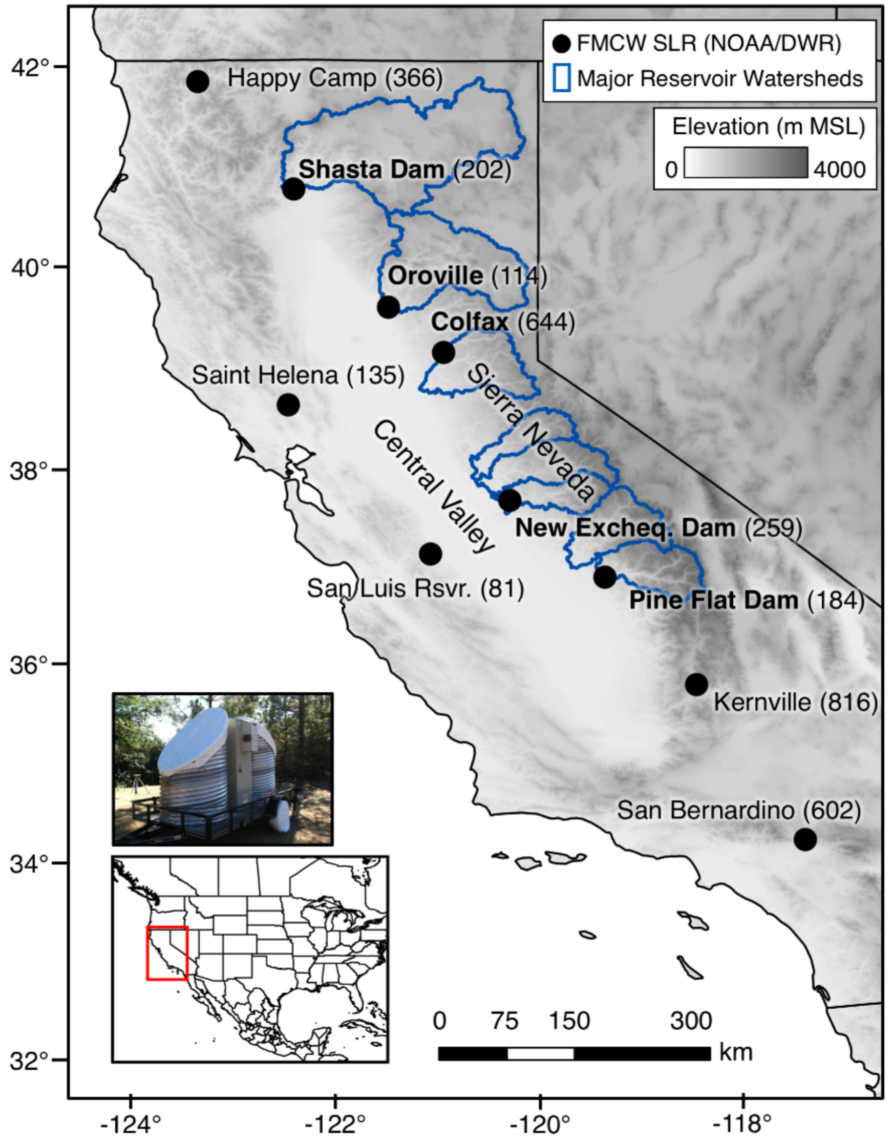

Figure 2.2. Map of California topography displaying the 10 FMCW radars used in this study (black circles). The boundaries of eight Sierra Nevada watersheds supplying major reservoirs (blue outlines) are shown as follows from northwest to southeast: Shasta Lake, Lake Oroville, Folsom Lake, New Melones Reservoir, Don Pedro Reservoir, Lake McClure, Millerton Lake, Pine Flat Lake. Elevation (m MSL) for each radar is shown in parentheses. Key radars within hydrologically-important basins are labeled in boldface text. An inset map and image of the Colfax FMCW radar are also included (image provided by NOAA ESRL).

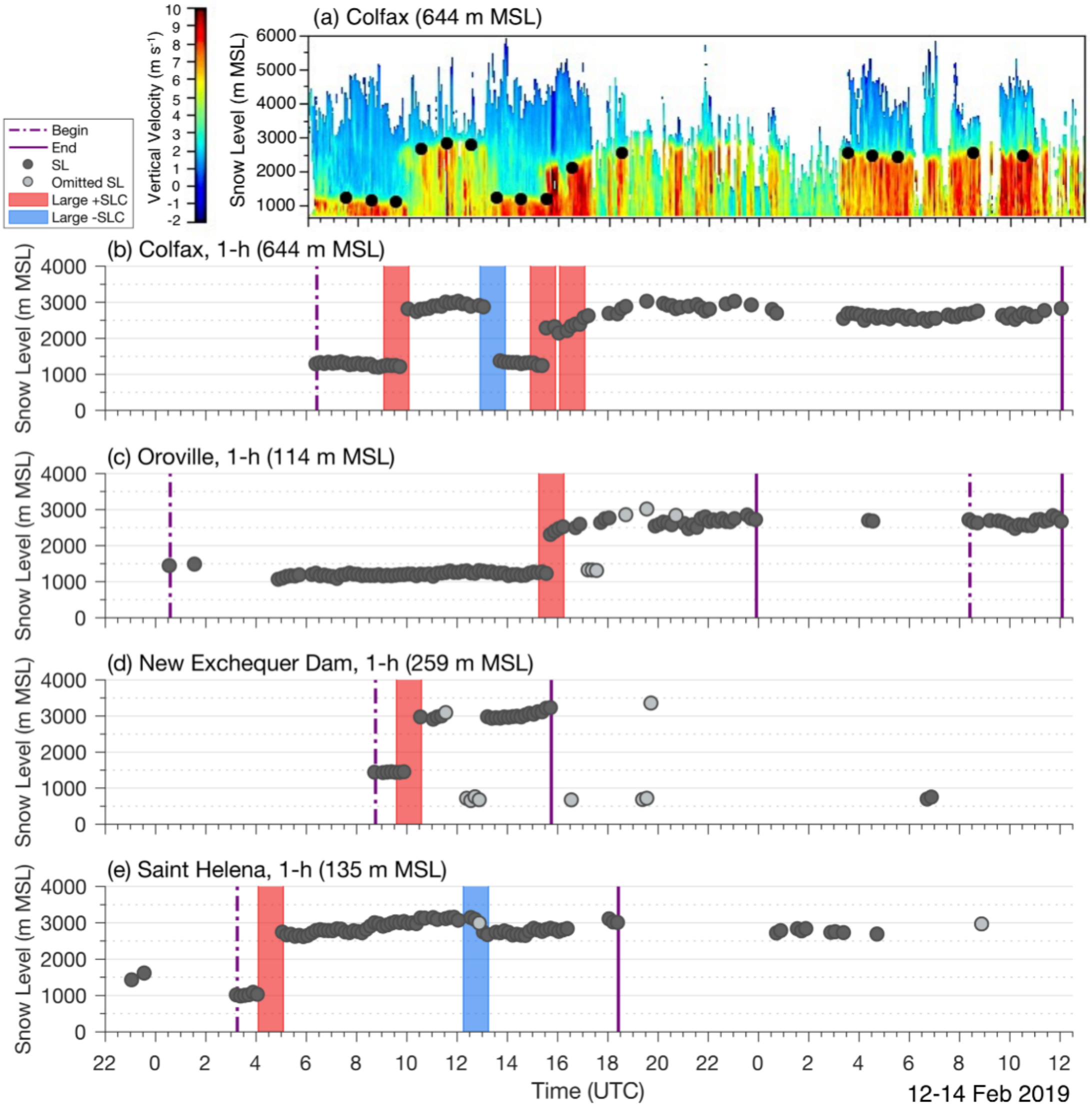

Figure 2.3. 2019 Valentine's Day Event time series of (a) radar vertical radial velocity in m s^{-1} and hourly-averaged radar-derived snow levels (SLs), and (b)-(e) snow levels at maximum temporal resolution. (a) and (b) both display measurements at Colfax. Radar site elevations are displayed in parentheses within each subplot title. Snow levels retained for analysis in this study are shown as solid dark gray circles. Snow levels omitted as a result of conservative data quality filters (Filters 1a, 1b, and 2) are shown as white circles with colored outlines (goldenrod, green, and medium gray, respectively). In (a), snow levels are averaged every hour, positioned at the 30-minute x-axis mark for each hour. Vertical dash-dot purple lines denote the start of the defined semicontinuous snow level event while solid purple lines mark the end of the event. Red and blue vertically-elongated bands indicate the presence of a large one-hour snow level ascent or descent, respectively.

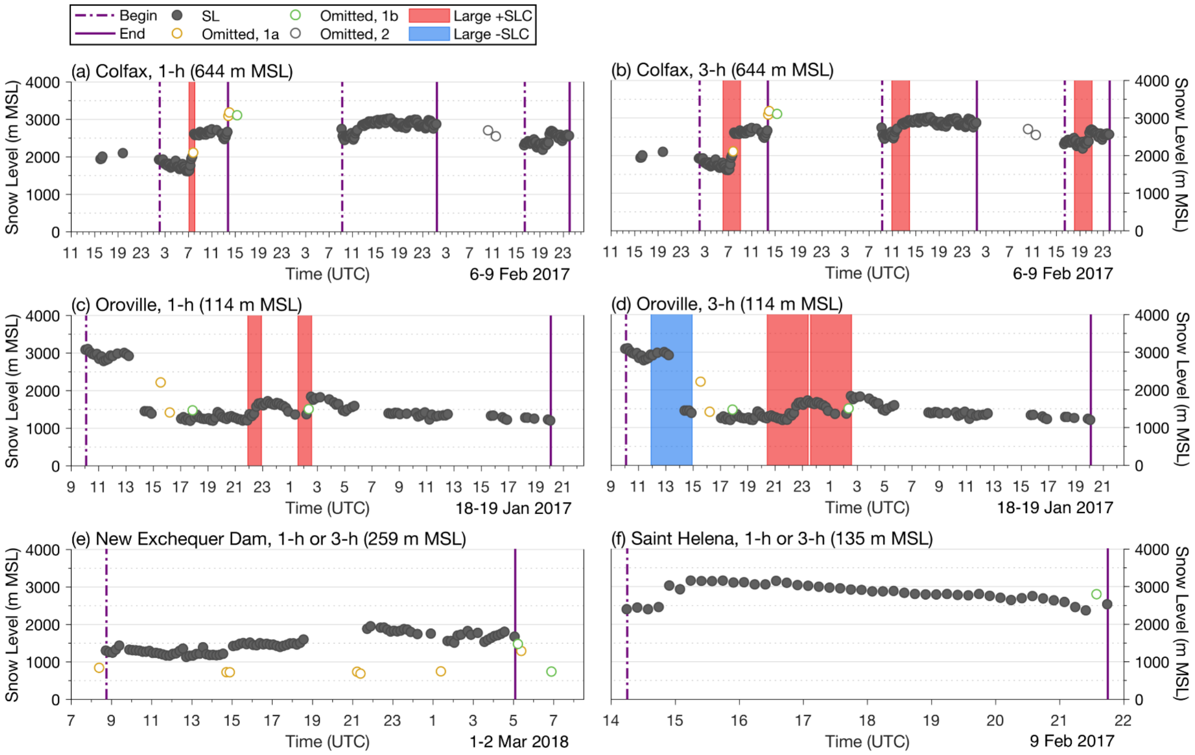

Figure 2.4. Radar-derived snow level time series as in Figure 2.3, but now for different dates and radar site combinations. Panels (a) and (c) assess one-hour maximum vertical snow level changes while (b) and (d), respectively, assess three-hour changes during the same time period and at the same radar. Panels (e) and (f) feature time periods that do not contain extreme SLCs and remain the same whether considering one- or three-hour SLCs.

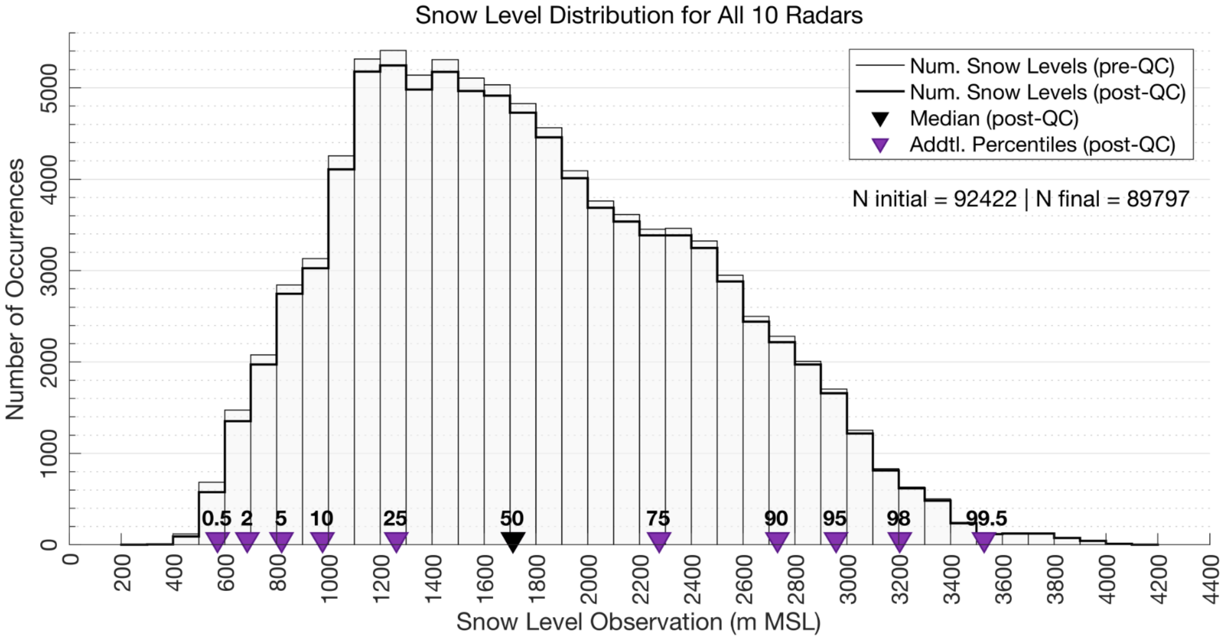

Figure 2.5. Frequency distribution of all snow level measurements post-QC (bold black line) and pre-QC (thinner black line) filters (1a, 1b, and 2) plotted as a histogram. The number of occurrences is displayed along the y-axis and the snow level height (m MSL) is shown along the x-axis (100-m bins). Percentiles are included as inverted triangles (all are shown in purple except for the 50th percentile, i.e., median, shown in black); from left to right, the 0.5th, 2nd, 5th, 10th, 25th, 50th, 75th, 90th, 95th, 98th, 99.5th percentiles.

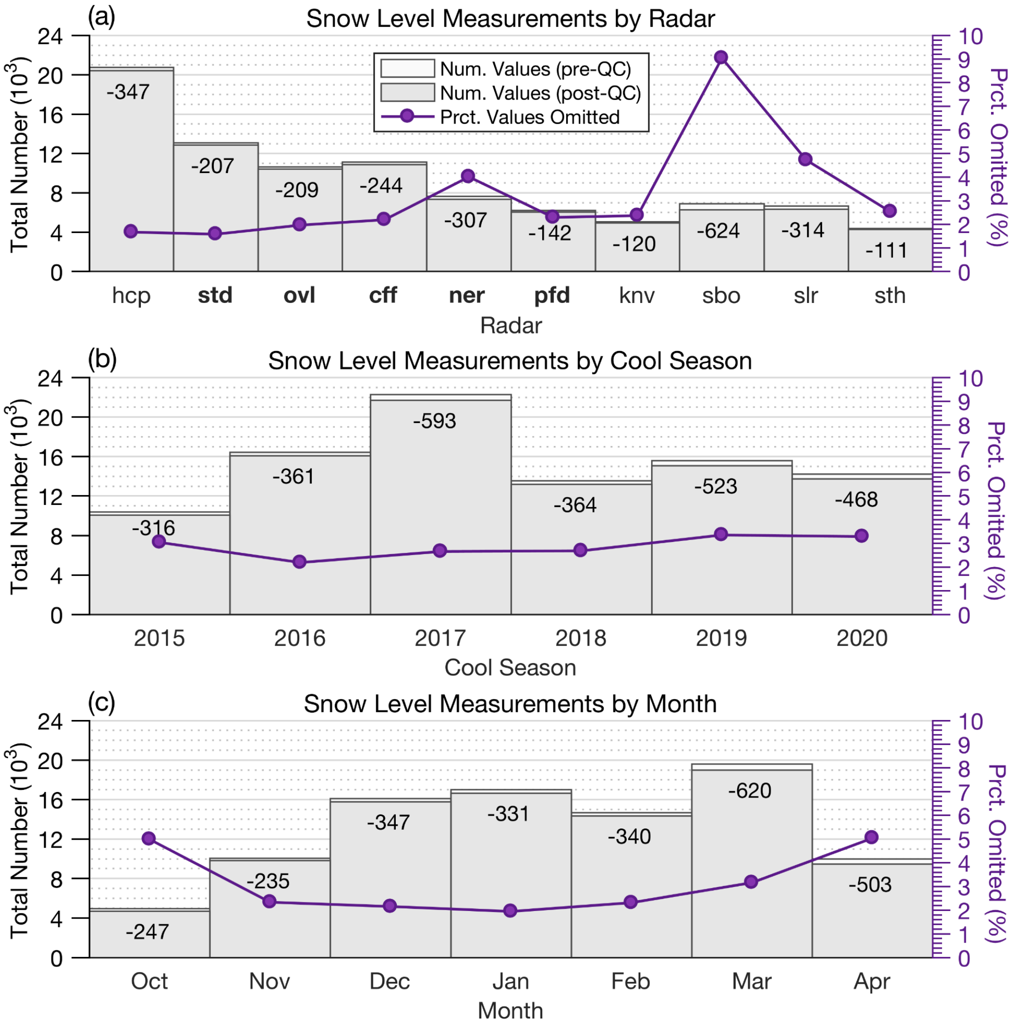

Figure 2.6. Total counts of snow level measurements before (light gray bars) and after (dark gray section of bars) applying data QC filters are plotted along the left y-axis. The number of measurements omitted are shown as a negative value near the top of each bar. The purple dots and line plotted along the right y-axis represent the percentage of snow level measurements omitted. Aforementioned variables are plotted by (a) radar (in descending latitudinal order from left to right up to San Bernardino, and then including the two near-coast radars on the far right; with key radars shown in bold text), (b) cool season (1 October - 1 May) of each water year, and (c) month.

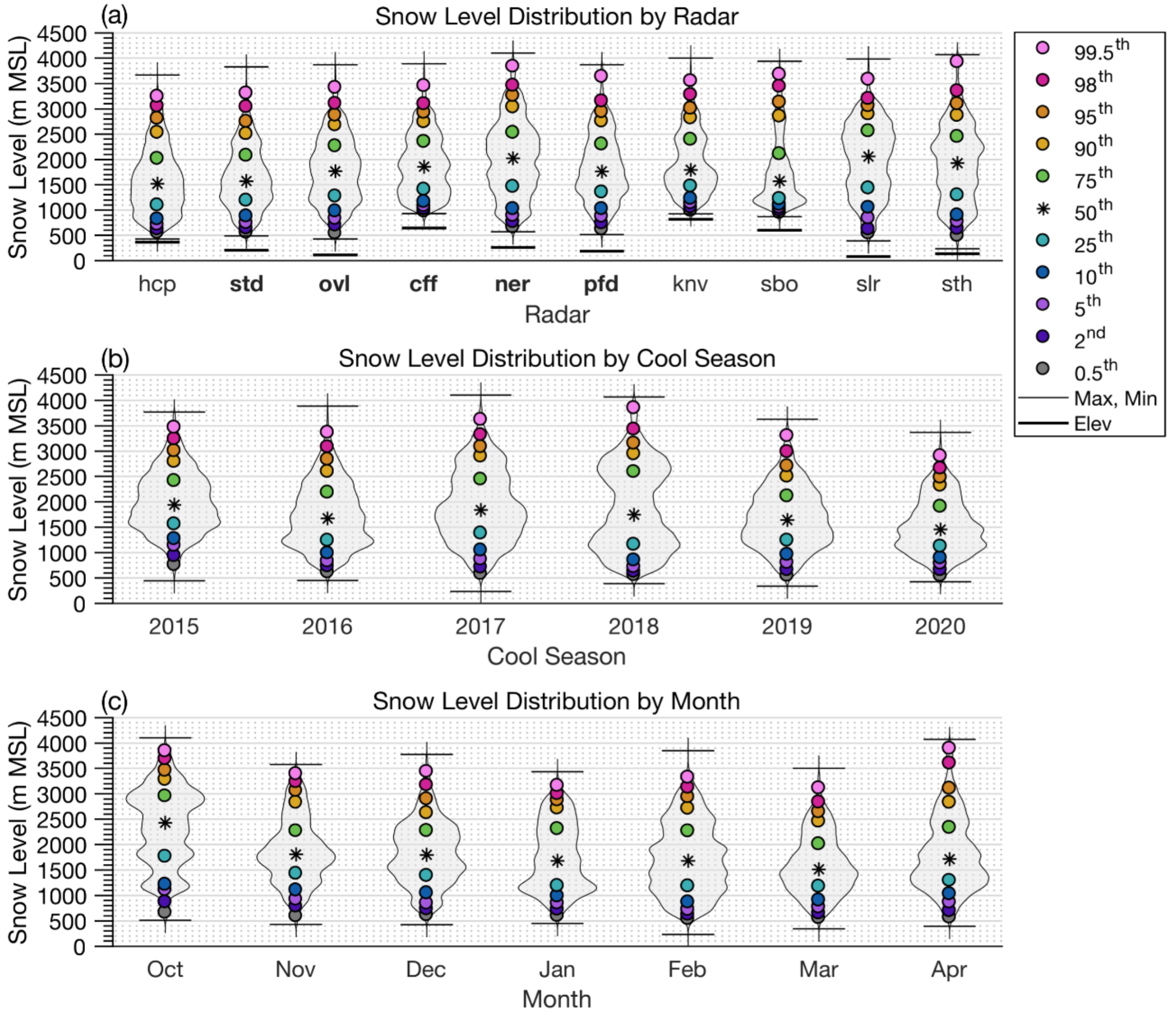

Figure 2.7. Frequency distributions of quality-controlled snow level measurements are displayed within each violin, organized by (a) radar, (b) cool season, and (c) month. Snow level height is plotted along the vertical axis. The number of occurrences is represented by the width of each violin. Note these violin widths are based on snow levels within each violin and are not standardized across violins or subplots. Percentiles computed using all snow levels within each violin are also plotted. From bottom to top, the 0.5th, 2nd, 5th, 10th, 25th, 50th (i.e., median), 75th, 90th, 95th, 98th, 99.5th percentiles, are displayed. All percentiles are plotted as colored circles except for medians which are displayed as black asterisks. The lower and upper horizontal solid line for each violin indicates the minimum and maximum snow level, respectively. In (a), the radar ground elevation is also shown as a bold line. Violin tails that extend vertically to magnitudes larger than the minimum or maximum value do not contain real snow level observations, but are instead a result of kernel density estimation (smoothing) within the violin plotting function (Hoffman 2021).

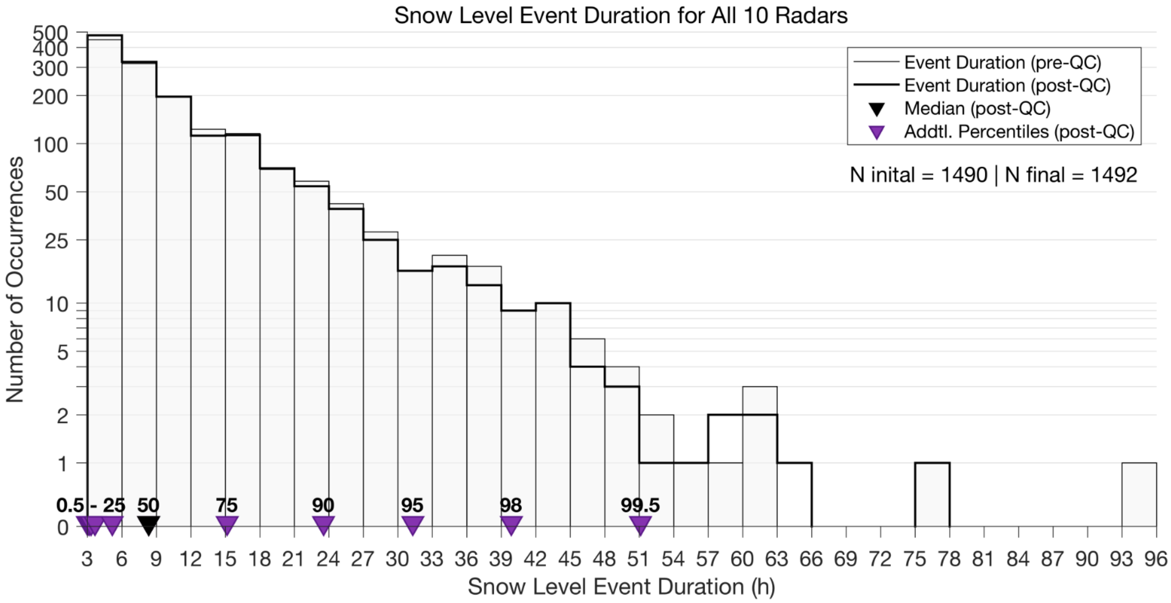

Figure 2.8. Semilog frequency distribution (displayed as a histogram) of the duration of all semicontinuous snow level events for all 10 radars. The number of occurrences is shown in log form on the y-axis for each event duration bin along the x-axis (three-hour bins). Note the y-axis begins at one and increases by increments of 1-10. Percentiles for post-QC snow levels are shown as inverted triangles as in Figure 2.5.

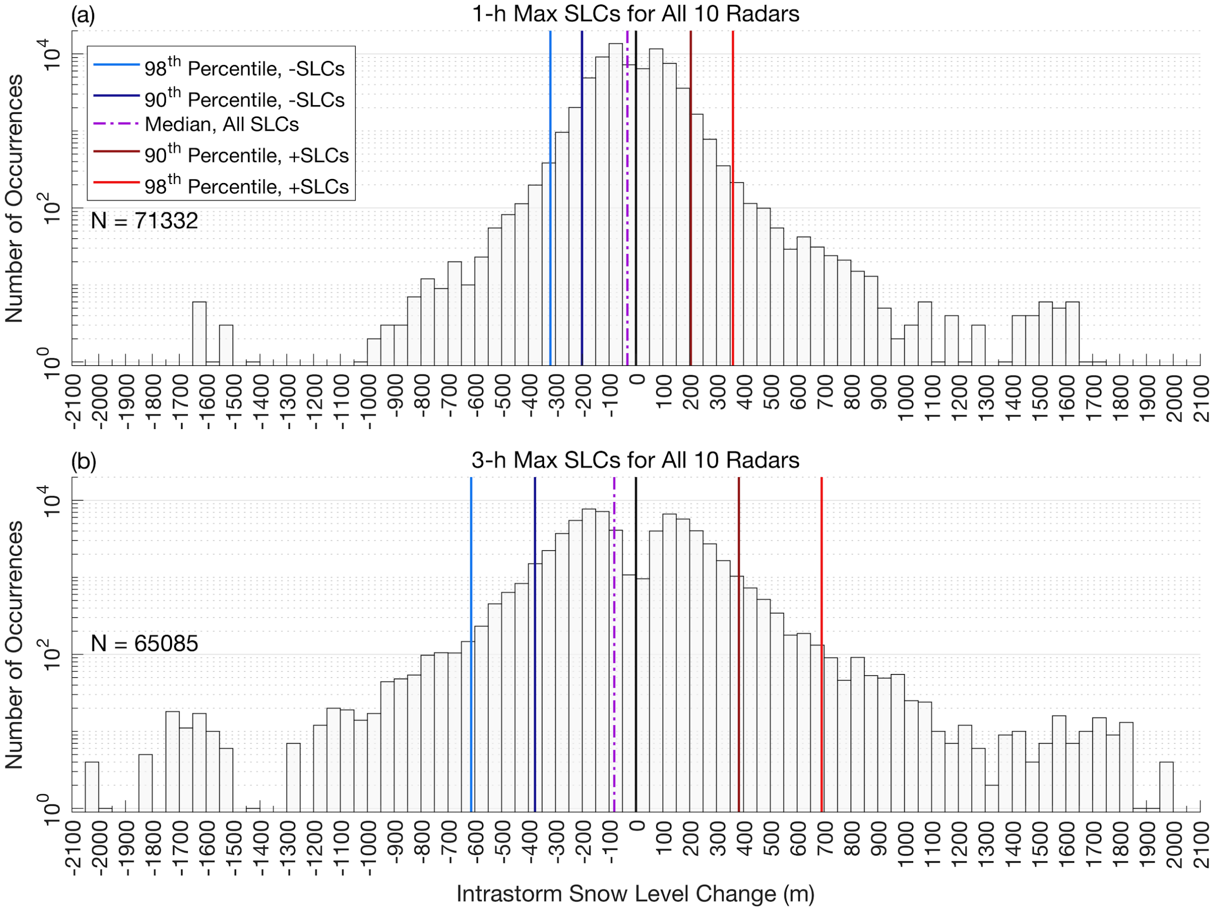

Figure 2.9. Histogram similar to Figures 2.5 and 2.8, but now for all maximum SLCs found within (a) one-hour (b) three-hour time increments. The number of occurrences (light gray bars) is plotted in log form along the y-axis for each binned SLC along the x-axis (binned every 50 m). Vertical lines, from left to right, indicate the 98th percentile for -SLCs (bright blue), 90th percentile for -SLCs (dark blue), median (i.e., 50th percentile) for both positive and negative SLCs (dash-dot purple), zero line (bold black), 90th percentile for +SLCs (dark red), and 98th percentile for +SLCs (bright red). N is the total number of one- or three-hour SLCs without accounting for overlapping time periods resulting from rolling 10-min windows. Only post-QC intrastorm SLCs of magnitudes exceeding zero are included.

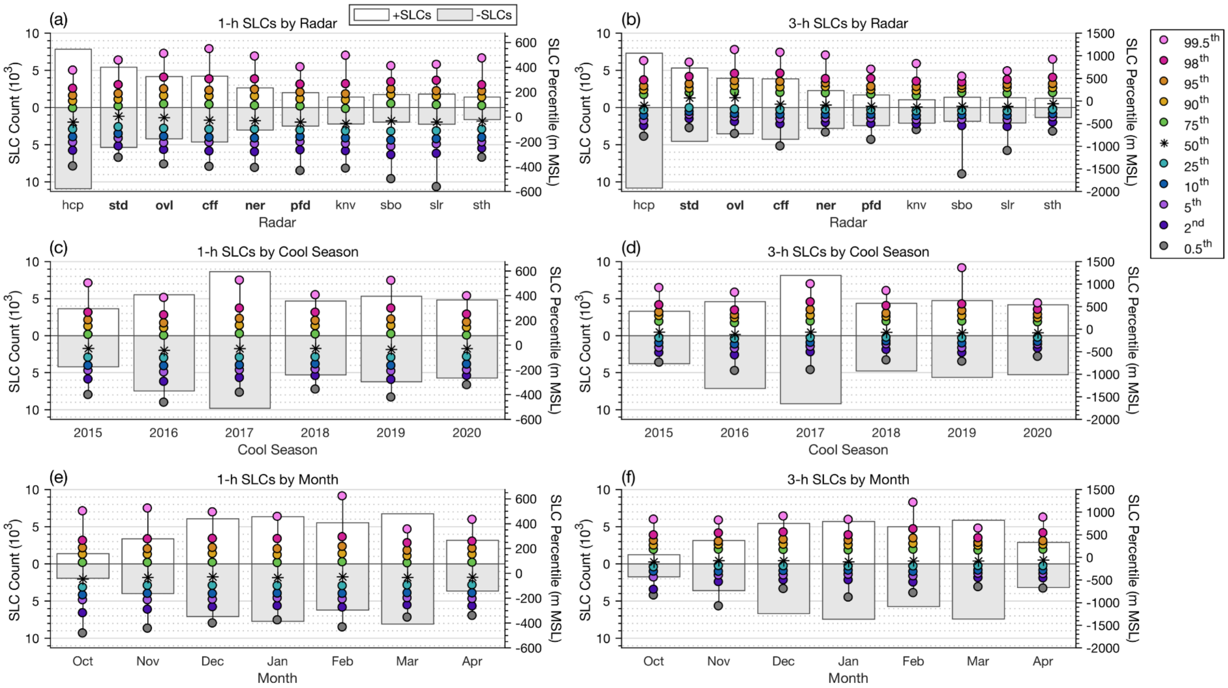

Figure 2.10. Total counts for one-hour, (a), (c), (e), and three-hour, (b), (d), (f), maximum SLCs shown as bars along the left-hand y-axis in 10^3. The zero line for the left-hand y-axis is positioned near the centerpoint of the axis, with medium gray (downwards-counting) bars and white (upwards-counting) bars indicating the negative and positive SLC sample sizes, respectively. Along the right-hand y-axis, percentiles for all SLCs regardless of sign are plotted as colorful circles in m MSL (as in Fig. 2.7). Medians are shown as black asterisks. The background y-axis grid corresponds to the left-hand y-axis. Subplots display values separated by radar, (a) and (b), cool season, (c) and (d), and month, (e) and (f). Note the range for right-hand y-axes differs between the left-column subplots (for one-hour SLCs) and the right-column subplots (for three-hour SLCs).

Chapter 3

Extreme Intrastorm Changes in Radar-Derived Snow Levels: Definition and Characteristics

3.1. Abstract

Abrupt, large-magnitude rises and falls in rain-snow transition elevations, or atmospheric snow levels, affect precipitation phase and have implications for hydrologic processes and communities. Our study defines, identifies, and examines *extreme snow level changes* (SLCs) derived from 10 California vertically-oriented radars during six recent cool seasons. Through a percentile-based threshold approach, we define extreme SLCs as changes with magnitudes ≥ 400 m within a one-hour period. We identify a total of 134 extreme snow level rises and 113 extreme falls. Extreme +SLCs occurred ~1.5-4.4 times more often in 2017 than any other year while extreme -SLCs occurred ~1.3-4.7 times more in 2016 than any other cool season. December through March contain the largest number of extremes while October and April have reduced counts. February experienced the peak number of both extreme snow level rises and falls. The three northernmost radars observed quadruple the number of extreme snow level rises occurring at the three southernmost sites and nearly twice as many extreme falls. We also uncover notable spatiotemporal relationships for extremes across close-proximity or downstream-upstream neighbor radars.

Further, we enlist a high-resolution atmospheric river detection catalogue, discovering 60-100% of extreme SLCs at each radar occurred during an atmospheric river storm period. By

assessing reanalysis-derived integrated water vapor transport (IVT) values, we find an extreme snow level rise is at least four times as likely to occur within large-magnitude IVT maximum conditions (1000-1100 kg m^{-1} s^{-1}) than with IVT maxima half as large (< 600 kg m^{-1} s^{-1}). Additionally, mean SLCs during large-magnitude IVT periods are almost twice the magnitude of +SLCs and nearly 1.5 times larger than those of -SLCs during small-magnitude IVT maximum events (~100-200 kg m^{-1} s^{-1}). Methodologies established to detect and elucidate extreme intrastorm SLCs in this study support future studies involving causes and hydrometeorological impacts of rapid and substantial changes in snow level.

3.2. Significance Statement

California experiences cool season storms providing valuable water, but also contributing to disasters affecting lives and property. While snow from storms can result in immediate hazards, it often remains at high-elevations until gradually melting in warmer weather. Rainwater flows into rivers and reservoirs and can suddenly lead to flooding and landslides. To isolate instances where precipitation type changed abruptly and substantially, we defined and described extreme one-hour vertical changes (magnitude ≥ 400 m) in the radar-derived atmospheric snow level, the altitude where falling snow becomes rain. We provide a statewide climatology of extreme rises and falls, and examine associations with California's most prevalent storms, atmospheric rivers, also setting the stage for future investigations of controlling mechanisms and impacts of extremes.

3.3. Introduction

Landfalling atmospheric rivers (ARs) provide California with the majority of its annual precipitation (up to 40-60%) and mountain snowpack (up to 40%) for water supplies in only a few cool season days (e.g., Guan et al. 2010; Dettinger et al. 2011; Ralph and Dettinger 2012; Rutz and Steenburgh 2012; Ralph et al. 2013a; Rutz et al. 2014). These transient, elongated ribbons of enhanced vertically-integrated water vapor transport (IVT exceeding 250 kg m^{-1} s^{-1}) form over near-tropical Pacific regions, extending up to ~3 km MSL with lengths (> 1500 km) double the extent of their widths (Ralph and Dettinger 2011; Ralph et al. 2018).

AR-attributed precipitation ended 33-40% of persistent California droughts between 1950 and 2010 (Dettinger 2013). Each year, however, an average of ~1-3 ARs impinging on northern coastal regions are categorized as extreme or exceptional, resulting in flood and snow hazards that outweigh water resource benefits (1980-2017; Ralph et al. 2019a) and lead to costly damage (Corringham et al. 2019). Hazards can also result during weaker ARs (reduced-IVT and/or shorter-duration) which occur more frequently. During ARs, orographic lifting mechanisms and precipitation enhancements intensify in regions upwind of coastal and inland mountains as a result of moist-statically neutral conditions within the lowest 3 km of the atmosphere (Ralph et al. 2006). An average of 10-25 ARs (of all strengths) affect northern coastal California each cool season (e.g., Ralph et al. 2013a, 2019a, 2019b; Rutz et al. 2014). Near the coast and further inland, AR conditions persist for an average of ~20-25 and 15-20 hours, respectively.

Atmospheric water vapor thresholds (e.g., based on IVT or precipitable water) and spatial and temporal parameters are often employed to detect and track ARs (Shields et al. 2018; Ralph et al. 2019b). When ARs reach western coasts and penetrate inland, their moisture interacts with

California’s Coast Ranges, Sierra Nevada, and southern Klamath Mountains. In some cases, this interaction drastically enhances precipitation along windward slopes through orographic lifting (e.g., White et al. 2003a; Smith et al. 2010) which, in turn, affects winter floods and springtime runoff flows (e.g., Dettinger et al. 2004). Also near or within California’s mountains, there exist multiple hydrologically-important drainage watersheds which are sensitive to incoming precipitation (e.g., the American, Feather, Russian River basins).

Power outages, transportation complications, and avalanches (Hatchett et al. 2017a; 2018; 2020) can ensue from rapidly-accumulating or heavy snowfall during precipitating storms such as ARs. Landslides and debris flows (Young et al. 2017; Oakley et al. 2018; Cordeira et al. 2013), floods (e.g., Ralph et al. 2006, 2019a; Dettinger et al. 2011), and other rain or rain-on-snow (McCabe et al. 2007; Guan et al. 2016) hazards can swiftly take or threaten lives and damage infrastructure (e.g., Jibson 2006; White et al. 2019). Instances of rapid, large changes in the amount of rain versus the amount of snow experienced during precipitation storms can lead to multifaceted disasters, limiting preparedness for flood and snow hazards.

The atmospheric snow level or brightband height, described as the minimum altitude at which free-falling frozen hydrometeors melt completely to rain, dictates precipitation partitioning. Vertically-oriented radars identify the snow level as the altitude of maximum radar reflectivity within the hydrometeor melting layer (i.e., bright band; typically 300-700 m thick; Matsuo and Sasyo 1981). In coastal California, this max-reflectivity altitude is positioned an average of 192 m below freezing levels (0°C isothermal altitude; White et al. 2002).

Median cool season California snow levels are approximately 1500-1700 m MSL, with values of 1200-2000 and 1800-2500 m MSL at sites north and south of Saint Helena, respectively (Fig. 2 of Hatchett et al. 2017b; Fig. 1 of Henn et al. 2020; Figs. 2.5 and 2.7 of this dissertation). Because mountain regions consist of steeply sloped surface elevation bands, precipitation and runoff in watershed-feeding basins near the Sierra Nevada and other California orography, for instance, are especially sensitive to variations in snow level height. For two northern Sierra Nevada basins, a freezing level forecast error of only ± 350 m can yield watershed runoff volume uncertainties that exceed 50% of each reservoir's flood control capacity (i.e., contributing to flooding; Fig. 2 of Sumargo et al. 2020a).

Previous studies find key melting layer features, such as the freezing level, present difficulties for operational atmospheric and hydrologic models, resulting in forecast biases, e.g., underforecasts on the order of 100-900 m with larger biases during high snow level-heavy rainfall periods (White et al. 2010; Neiman et al. 2014; Henn et al 2020). A recent study computed and assessed one- and three-hourly maximum snow level changes (SLCs) across California during six water years (2015-2020), finding snow level rises and falls most common during December through March, at northern radar locations, and during enhanced-precipitation cool seasons including 2017 which set the climatological max for precipitation (findings of Chapter 2 of this dissertation). Smaller-magnitude SLCs (-200 to 200 m in one hour) occurred more often, 90% and 57% of the time for one- and three-hour SLCs, respectively, but larger-magnitude intrastorm SLCs have also been observed (Figs. 2.9 and 2.10 of this dissertation). For example, recent studies feature one- and three-hour SLCs on the order of 300-1000 m occurring during the hydrometeorologically high-impact 2019 Valentine’s Day Event and 2017 Oroville Dam Spillway Emergency (White et al. 2019; Hatchett et al. 2020; Figs. 2.3 and 2.4 of this dissertation).

In related work, six cases featuring large-magnitude snow level rises (> 500 m during a single precipitation event or across successive events; occurring on the order of ≤ 24 hours) were assessed during 2010-2014 cool seasons at a Colfax and Sacramento site (southwest of Colfax ~80 km; Fig. 2 of Hatchett et al. 2016). Every one of these large-magnitude intra- or inter-storm rises occurred during one or multiple landfalling ARs. Elevated snow levels (means of 2100-2400 m MSL) and associated extreme precipitation (accumulated liquid precipitation exceeding the 93rd-98th percentile; depending on event, radar, precipitation station) coincided with mid-season (December-March) peak runoff events during five of these six large-magnitude snow level rise cases.

Recent studies prove ARs play dominant roles in California precipitation occurrence, intensity, and processes (e.g., summary provided by Gimeno et al. 2014), but less is known about changes in snow level surrounding AR and storm periods. To provide a robust definition for and evaluation of *extreme intrastorm SLCs* we include snow level falls in addition to rises which were solely considered in previous work. Additionally, we consider an increased number of recent cool seasons (six total), capturing years with anomalously high and low precipitation totals. Further, we increase the number of radar locations considered, employing measurements derived from 10 vertically-oriented California S-band radars ranging from near-coast regions to the southern Klamath mountains to along the windward side of the Sierra Nevada. To start, we outline employed datasets and methodologies to define and describe extremes (Sections 3.4-3.5). Next, we share results and discuss (Section 3.6) their physical interpretation and significance. We present and describe the distribution and characteristics of extreme intrastorm SLCs and their variations by cool season, month, and radar. Associations between SLCs of varying magnitude and atmospheric moisture and ARs are also identified and explored. Lastly, we summarize findings in the context of societal implications (Chapter 4 of this dissertation), providing motivation for future studies centering hydro-societal impacts and atmospheric mechanisms driving extreme SLCs.

3.4. Data

3.4.1. Intrastorm Snow Level Changes

We employ both maximum sub-daily (one-hourly) SLCs and semicontinuous snow level events described and identified by Osborne et al. in Chapter 2 of this dissertation. Initially, we consider all maximum intrastorm SLCs previously computed using 10-minute rolling intervals to maximize SLC sample size. Later, we adjust for overlapping or repeating extreme SLCs (Section 3.5.1). A maximum one-hour SLC is described as a single peak-magnitude SLC within a one-hour time window, respectively (a single rise or fall per time window).

We solely consider SLCs within semicontinuous snow levels events, previously defined as time periods which provide valid data for ≥ 50% of the event, do not contain gaps in snow level measurements that exceed three hours (allowing for brief breaks in clouds or intermittent non-brightband precipitation periods, for instance), and amount to a total event duration of at least three hours (including data gaps). This dataset providing semicontinuous snow level events and SLCs is only capable of capturing snow level-containing stratiform precipitation events, so convective (elevated turbulence makes it difficult to identify snow levels) or warm, solely rain-containing or cooler snow-exclusive events (which do not contain snow levels) are not included (White et al. 2003a; Neiman et al. 2005; as described in Chapter 2 of this dissertation).

In addition, in Chapter 2, Osborne et al. designed and applied data quality check (QC) filters to minimize the number of large-magnitude (~300-1000 m) intrastorm SLC false alarms. Only ~2.8% of the original snow level dataset (1 October-1 May of water years 2015-2020) was omitted to minimize inexplicable or error-yielding snow levels and cases featuring short-lived SLCs (sustained durations of less than one hour) which are considered less likely to contribute to notable variations in hydrologic processes. To assess the most rapidly-occurring SLCs and to determine a minimum threshold for extremes (Fig. 3.1; Section 3.5.1), we employ these post-QC one-hour SLCs.

Original radar-derived snow level measurements were provided by the National Oceanic and Atmospheric Administration Physical Science Laboratory (NOAA PSL) of the Earth System Research Laboratories (NOAA ESRL), the California Department of Water Resources (CA-DWR), and the Cooperative Institute for Research in Environmental Sciences (CIRES). The 10 included profilers are Frequency-Modulated Continuous-Wave (FMCW) radars for which transmitted signals are modulated instead of unmodulated, contributing to improved accuracy by providing both target speed and distance. Further, radar signal transmission and reception are continuous instead of pulsed, reducing production and operation costs and helping filter out larger signals (Battan 1973; White et al. 2002; Johnston et al. 2017). These FMCW Snow Level Radars (SLRs; henceforth termed radars) operate within the S-band (2.835 GHz) which is well-suited for measuring differences in hydrometeors even during extreme precipitation (Table 3.1, Fig. 3.2).

Radars were run with 40 to 60-m vertical bands up to a maximum height of ~8-10 km. The Doppler radars provide snow levels up to every 10 minutes during snow-level containing precipitation events (typically stratiform events rather than convective). These reduced-cost, state-of-the-art S-band radars and their accompanying snow level detection algorithm (involving reflectivities measured as signal-to-noise ratios, and vertical radial velocities) come as valuable deliverables of the interagency Hydrometeorology Testbed (HMT) Legacy Project and the Pacific Land-falling Jets Experiment (PACJET; White et al. 2002, 2013). At present, there are limitations regarding the common period of record across radars (six years considered in this study). There also exist periods when FMCW radars could not be operated (e.g., January 2019's U.S. government shutdown).

Vertically-oriented radars identify the snow level as the altitude of maximum reflectivity within the melting layer. Reflectivity is simultaneously enhanced at the snow level (i.e., brightband height) by two predominant characteristics of melting hydrometeors. One key factor is the relatively large diameter of melting hydrometeors which are closer in size to snowflake clusters (~3-13 mm diameters) and are more likely than rain (diameters near 2 mm, with 5 mm maximum) to grow by aggregation due to their water-coated surfaces (Austin and Bemis 1950; Matsuo and Sasyo 1981). The other predominant factor involves the increased liquid-to-solid water ratio of melting particles compared to frozen hydrometeors (dielectric constant of ~0.93 and 0.21 for water and ice, respectively; e.g., White et al. 2002). During example cases for Bodega Bay (coastal California upstream of Saint Helena) and a downstream site near western foothills of the central Sierra Nevada, reflectivity values (measured as signal-to-noise ratios) of around 86-88 dB and 105 dB, respectively, result at the snow level - compared to reflectivities 1-20 and 1-15 dB smaller for higher snow-experiencing altitudes and lower altitudes containing rain-snow mixtures or rain, respectively (Fig. 2 of White et al. 2002; Fig. 2 of White et al. 2010).

3.4.2. Atmospheric Moisture

We use vertically-integrated water vapor transport (IVT) values computed and stored on the Center for Western Weather and Water Extremes (CW3E) supercomputer server. IVT values were computed using variables provided by the National Aeronautics and Space Administration (NASA) Modern Era Retrospective Analysis for Research and Applications, Version 2 (MERRA-2; Gelaro et al. 2017). CW3E's high-resolution MERRA-2 IVT dataset has a spatial resolution of 0.5° latitude (~50 km) x 0.625° longitude and contains three-hourly instantaneous values derived using the following equation:

$$IVT = -\frac{1}{g}\int_{Pb}^{Pt} (q_{(p)}\, \boldsymbol{V}_{H(p)})\, dp, \qquad \textit{Equation 1}$$

where $\boldsymbol{V}_H$ is the horizontal wind vector (m s^{-1}, including zonal and meridional components), g is the acceleration due to gravity, P_b and P_t denote the bottom and top-level atmospheric pressure (1000 and 200 hPa), respectively, and q is specific humidity (dimensionless ratio, kg kg^{-1}; mass of water vapor to total system mass) (Cordeira et al. 2013; Shields et al. 2018). Because the SLCs we emphasize occur over one-hour windows, we proceed by expanding the IVT dataset to one-hourly using linear temporal interpolation. We identify MERRA-2 grid cells nearest to each radar location. If the nearest MERRA-2 grid point lies east or north of the radar, we instead consider the nearest point upstream of the radar, to the west and south (Fig. 3.2).

3.4.3. Atmospheric River Events

To determine whether or not an atmospheric river (AR) existed within ± six hours of an extreme SLC, we utilize the Guan and Waliser (GW) catalogue, Version 2 (V2), incorporating six-hourly MERRA-2 variables (AR detection in Guan and Waliser 2015 - V1; refined in Guan et al. 2018 - V2; AR tracking and additional AR variables in Guan and Waliser 2019 - V3). Using methods and IVT threshold and land-sea mask files consistent with Guan et al. (2018), Zhenhai Zhang of CW3E provided AR information for water year 2020. Since the AR catalogue spatial grid is identical to the MERRA-2 IVT grid, we consider the same 10 grid points (upstream and near each radar) used for IVT in the previous section.

Results may vary if employing other AR catalogues, as underlying detection and tracking methods may require different moisture, temporal, or spatial criteria (e.g., Shields et al. 2018; Ralph et al. 2019b). The GW method identifies "AR shapes" using measures of (i) IVT intensity, IVT direction, and moisture plume geometry. To elaborate, AR shapes are defined as areas where: (i) IVT exceeds a minimum of 100 kg m^{-1} s^{-1} and also exceeds a local (single cell) minimum threshold defined by the seasonal 85th percentile (includes 5-month period centered on month of interest from 1997-2014), (ii) the plume's mean IVT indicates considerable poleward motion within 45° of the plume's orientation, and (iii) the enhanced IVT region exceeds a length of 2000 km and a 2:1 length-to-width ratio. Recent refinements to the algorithm help capture ARs with enhanced IVT cores that lack a clearly-defined 85th percentile IVT contour (Guan et al. 2018 - V2). The GW catalogue employs IVT computed using the same variables as Equation 1 (integrated up to 300 hPa instead of 200 hPa; Guan and Waliser 2015).

One reason we employ the GW AR detection (and tracking) catalogue is that it was created using IVT instead of integrated water vapor (IWV; Equation 1 without horizontal winds) alone. IVT accounts for not only the intensity, but also the movement of column-integrated moisture which is important for orographic precipitation processes (Neiman et al. 2002, 2009).

Another reason is because the method considers local and seasonal measurements to define minimum moisture thresholds rather than universal thresholds. Additionally, we selected the GW catalogue because it had a 94% match-rate with manually-identified AR landfall times (using satellite-observed IWV) along North America's western coasts which were recorded in the Neiman et al. (2008) catalogue (Guan and Waliser 2015). Lastly, AR ranking (rather than detection or tracking) methods (e.g., Ralph et al. 2019a) involve temporal requirements for enhanced IVT that are valuable for categorizing ARs by moisture intensity, duration, and impacts. These duration requirements, however, may be too strict for identifying weaker or shorter-duration ARs in studies involving atmospheric changes at hourly scales.

3.5. Methodology

3.5.1. Defining and Identifying Extreme Intrastorm Snow Level Changes

We define extremes (Fig. 3.1) based on 98th percentiles of SLCs (Table 3.1 and Fig. 3.3) within the maximum one-hour SLC dataset at five key radars (Fig. 3.2; SLC dataset described in Chapter 2 of this dissertation). Although 98th percentiles for positive and negative one-hour SLCs generally lie slightly beneath 400 m-magnitudes, we intentionally assign 400 m as the minimum magnitude used to define extreme intrastorm SLCs. As a result, in terms of magnitude, we isolate and investigate only the most extreme sub-daily SLCs. Additionally, by rounding the minimum threshold to 400 m for both one-hour rises and falls, we aim to provide results that are more relevant to forecasting operations, i.e., numerical weather prediction model vertical resolutions (vertical pressure-adjusted levels with spacing on the order of 300 m in the lowest 1-2 km).

Throughout this study, we place emphasis on values and results from five key radars which are located within hydrologically high-impact watershed basins along a northwest-to-southeast track within the windward side of the Sierra foothills (bolded in Table 1 and Fig. 1: Shasta Dam, Oroville, Colfax, New Exchequer Dam, Pine Flat Dam). Hereafter, one-hour SLCs of magnitudes ≥ 400 m are termed *extreme*. We later also refer to SLCs of magnitudes ≥ 800 m as *exceptional*.

When computing one-hour maximum SLCs in work described in Chapter 2 of this dissertation, we used rolling 10-min windows to maximize the number of valid SLCs. Therefore, within the employed intrastorm SLC variables, multiple extreme SLCs of the same sign can result within a period shared by multiple one-hour time windows. To determine local SLC maxima and minima, we first employed a peak detection algorithm (specifically, the MATLAB findpeaks function) for all positive and negative SLCs, respectively. Then, we identified instances where multiple extreme one-hour SLCs of the same sign exist within a single hour, respectively, and proceeded with only the single true-maximum extreme positive or negative SLC for each window. For this study, the most statistically-extreme intrastorm SLCs are desired which inherently limits the number of samples. To predict results when provided a larger population, we performed bootstrap resampling in certain cases (next section).

3.5.2. Significance Testing

Bootstrap resampling is employed for all statistical significance testing in this study, consistent with methods outlined in Dixon (2006) which were formally introduced by Efron (1979) and modified or expanded upon by studies that followed. All resampling efforts consider

10,000 random extractions from a larger population. After a value is selected, it is also returned to the population pool which means it may be selected multiple times. Random resampling in this way allows us to mimic the chaotic nature of the atmosphere and precipitating storms while assuming realizations of the near future yield a similar range of values or distributions as those in the previous six years. If considering realizations further into the future, a Monte Carlo method (e.g., Metropolis and Ulam 1949) could instead be used for statistical significance testing, as these methods do not solely rely on pre-existing measurements, but rather create new values to consider in a future climate.

When computing exceedance likelihood (Fig. 3.8), for example, bootstrap resampling considers 10,000 random maximum IVT value extractions from a pool of radar-averaged (mean) IVT maxima corresponding to non-extreme SLCs for each radar individually. With each extraction, we draw *n* number of samples from each radar population. The value of *n* matches the total number of non-extreme SLCs (for all years) which varies from radar to radar. For each radar, the exceedance likelihood is the percentage of the 10,000 resampled radar-averaged maximum IVT values (drawn from the non-extreme SLC IVT maxima pool) that exceeds the radar's IVT maximum for extreme SLCs.

We perform similar testing for results shown in Figure 3.9, but instead, to determine 90% confidence intervals for mean SLCs and extreme SLC percentages within each IVT maxima bin. In this case, for each IVT bin, we perform resample extractions (*n* number of times, where *n* = number of SLCs) to determine 95th and 5th percentile values resulting from 10,000 resampled mean SLCs and extreme SLC percentages.

3.6. Results and Discussion

3.6.1. Extreme Snow Level Change Threshold and Mean Conditions

As explained in Section 3.5.1, the 400 m-magnitude threshold for extreme one-hour changes is determined based on 98th percentile values (Fig. 3.1, Table 3.1). For the five key Sierra radars (Fig. 3.2), the 98th percentile for snow level falls is ~70 m smaller in magnitude than the value for rises; -315 m compared to 386 m, or 347 m when considering the absolute value of both positive and negative SLCs (Table 3.1, Fig. 3.3a). While ~2% of all positive and all negative SLCs (assessed separately by sign) at key radars are of magnitudes equaling or exceeding corresponding 98th percentile values, only ~1.8% and 0.9%, respectively, equal or exceed the 400 m-magnitude extreme threshold. As a result of the established 400-m extreme threshold for both positive and negative SLCs, this study yields fewer extreme snow level falls than rises, 113 extreme falls and 134 extreme rises (Figs. 3.3, 3.4, 3.5).

Percentiles for one-hour SLCs accounting for all 10 radars are slightly reduced in most cases compared to results for the five key radars, with exceptions for percentiles computed for all -SLCs (Table 3.1, Fig. 3.3a). The 98th percentile for one-hour SLCs varies by radar, from 298 and 303 m (Happy Camp and Saint Helena, respectively) to 417 m (Colfax) for +SLCs, and -283 (Saint Helena and Shasta Dam) to -366 m (San Bernardino) for -SLCs (Fig. 3.3b-c). This range of values across radars is narrower for smaller percentiles (90th and 95th; 0.5th-75th, not shown) and markedly wider for the 99.5th percentile (Fig. 3.3a-c). The range of values for +SLC 99.5th percentiles is notably wider (316 m) than that of +SLC 98th percentiles (119 m; Fig. 3.3b). Additionally, the range of 99.5th -SLC percentile values is nearly four times larger than the range for -SLC 98th percentiles (327 m and 83 m, respectively; Fig. 3.3c).

We find +SLC 98th percentiles of markedly smaller magnitudes resulting at Saint Helena and Happy Camp compared to other sites including San Luis Reservoir which is also located nearer the coast (Figs. 3.2 and 3.3b-c). For -SLCs, 98th percentiles at Saint Helena and Shasta Dam are reduced compared to all others. For instance, Saint Helena, which is ~144 km southwest (upstream) of Colfax at an elevation nearly 4.8 times below that of Colfax, yields positive and negative SLC 98th percentiles ~115 m and 55 m smaller, respectively, than those of Colfax (Figs. 3.2 and 3.3b-c). We find similar results when comparing 98th percentiles at Saint Helena to those for downstream Oroville which is slightly northwest of Colfax at an elevation similar to that of Saint Helena (98th percentiles are ~95 and 35 m larger, respectively, at Oroville compared to Saint Helena; Figs. 3.2 and 3.3b-c).

The fact that Saint Helena, however, produces one of the largest +SLC 99.5th percentiles (803 m; second only to Colfax's 828 m) and the largest overall +SLC, 1714 m during the 2019 Valentine's Day Event (Fig. 7 of Hatchett et al. 2020, and Fig. 2.3e of this dissertation), shows that exceptionally high-magnitude snow level rises can indeed occur at this nearer-coast site. Similarly, Colfax, New Exchequer, and Oroville experienced their largest snow level rise of 1602 m, 1537 m, and 1295 m, respectively, which arrived 5-11 hours after the initial rise at Saint Helena during the 2019 Valentine's Day Event (~4:05 UTC on 13 Feb 2019; Fig. 2.3 of this dissertation). Near 12:15 UTC the same day, Saint Helena's most extreme snow level fall occurred. This maximum fall (471 m) at Saint Helena was the smallest maximum for -SLCs of all 10 radars, a notable 202 m smaller than Kernville which takes second place (-673 m max). Approximately 45 minutes later, Colfax saw its largest fall of -1568 m, more than 3.3 times larger in magnitude than the maximum fall occurring at Saint Helena (Fig. 2.3 of this dissertation).

Overall, -SLC 98th percentiles tend towards a roughly direct relationship with radar longitudes with increased values for inland sites further east (refer to Fig. B.1), although a few values appear as outliers and there exist sample size limitations. Based on the SLC dataset considered in this study, we do not note clear trends involving -SLC 98th percentiles and latitudes or radar elevations, or for +SLC 98th percentiles and radar latitudes, longitudes, or elevations. Medians for -SLCs and +SLCs tend towards a nearly direct relationship with radar longitudes and a nearly inverse relationship with radar latitudes (more notably for -SLCs; Fig. B.2). Of relevance, previous studies found median snow levels at southern (climatologically-warmer and drier) California radars on the order of 300-1000 m higher than medians for northern locations (e.g., Fig. 1 of Henn et al. 2020, and Fig. 2.7a of this dissertation). Findings of this chapter additionally suggest one-hour SLC medians at southern (or eastern) radar locations exhibit larger magnitudes than those further north (or nearer the coast).

For eight of the radars, -SLC 98th percentiles are between 1 and 80 m smaller in magnitude (mean: ~45 m, median: ~50 m) than respective +SLC percentiles. The remaining radars (Happy Camp and San Bernardino) result in the opposite, with -SLC 98th percentiles 15 and 18 m larger, respectively, than +SLC percentiles. This result suggests extreme snow level rises are more likely to exist with larger magnitudes than those of extreme falls. We find 21 fewer -SLCs register as extreme (compared to +SLCs; Fig. 3.1, Table 3.1). The fact that the 400-m threshold for extremes is nearer the 98th percentile for one-hour snow level rises than the value for falls (Fig. 3.3) may contribute to this sign-dependent difference in the number of extremes.

When considering all extreme SLCs across the five key radars, the mean starting altitude for extreme rises is 580 m lower than the starting altitude for extreme falls (Fig. 3.1). The mean ending altitude for extreme rises is 630 m larger than the mean for extreme falls. Mean starting and ending heights for extreme SLCs when assessing all 10 radars are similar to (within ~14-40 m) values for only key radars, as are respective median heights compared to means (within ~18-65 m). Additionally, the mean ending (warmer) snow level altitude for extreme rises lies ~30 m above the mean starting (warmer) altitude for extreme falls. Meanwhile, the mean starting (cooler) snow level height for extreme +SLCs exists ~20 m above the mean ending (cooler) altitude for -SLCs (Fig. 3.1). The mean ending (warmer) snow level altitude and the mean starting (cooler) snow level altitude for +SLCs at key radars exist 20-30 m above the mean starting (warmer) and ending (cooler) altitudes for -SLCs, respectively. This result suggests extreme snow level rises, on average, involve slightly higher snow levels compared to those during extreme falls (note snow levels ≥ ~2000 m were associated with heavier rainfall periods in White et al. 2010). Lastly, across key radars, median magnitudes for one-hour extreme snow level rises and falls are similar to one another (~508 m and -518 m, respectively), and are ~100 and 70 m smaller than their respective means (Table 3.1, Fig. 3.4a-b).

3.6.2. Cool Season Variation of Extreme Snow Level Changes

Extreme +SLCs occurred most frequently during 2017 and 2019, with counts of 48 and 32, respectively, ~2.1-4.4 times larger than the other four cool seasons (Fig. 3.4c). Negative extremes are more often identified in 2016, 2017, and 2019 cool seasons compared to other years, with counts of 33, 25, and 24, respectively (Fig. 3.4d). These values are ~2.4-4.7 times larger than the extreme fall counts of the three remaining years. The smallest extreme rise counts are 11 (2015) and 14 (2016 and 2020), while the minimum number of extreme falls, 10 and 7, exist during 2018 and 2020, respectively (Fig. 3.4c-d). Maximum -SLCs are of smaller magnitudes for water years 2015 and 2018, 70 and 645 m, respectively, compared to peaks of ~980-1620 m for the remaining years. Extreme rise maxima are also reduced for 2015 and 2020 in addition to 2016, ~910-1060 m compared to ~1430-1710 m for the other cool seasons.

When instead considering medians for extreme magnitudes, we find values ~5 (2019) to 127 (2015) m larger for extreme snow level rises compared to falls to all years except 2018 and 2020. For these two cool seasons, the medians for extreme +SLCs are ~26 and 33 m smaller, respectively, than corresponding extreme -SLC medians. Further, the range of median values for extreme +SLC magnitudes (width of 156 m) is nearly three times wider than the range for extreme -SLCs (Fig. 3.4c-d).

Our investigations reveal there are not only more extreme +SLCs overall during 2017 and 2019 compared to other cool seasons (Fig. 3.4c), but that the greatest number of exceptional +SLCs (magnitude ≥ 800 m) also occur during these years (10 and 9, respectively; Fig. 3.5c). For -SLCs, elevated exceptional SLC occurrences result during 2016 and 2017 (5 and 3, respectively; Fig. 3.5d). It should be noted that sample sizes for exceptional SLCs are relatively small, with 25 exceptional rises and 11 falls in total.

Largely, anomalously wet cool seasons yield more extreme and exceptional snow level rises and falls (Figs. 3.4c-d and 3.5c-d). Included is the recording-setting 2017 cool season which received a total of 240 cm of precipitation compared to a climatological mean of ~130 cm (Durand et al. 2020). The 2017 cool season contrasts with the dry 2015 cool season (95 cm of accumulated precipitation) which induced and exacerbated severe multi-year drought conditions across the western U.S. Anomalously wet years inherently offer a larger number of precipitation periods in which snow levels can exist, and may provide the atmospheric and hydrologic conditions necessary to produce precipitation events of larger magnitude, intensity, frequency, or impact. Conditions necessary to generate and fuel an atmospheric river storm or those associated with an El Niño period, for example, may duly contribute to rapid vertical changes in low-level temperatures that result in extreme SLCs. As anomalously wet and dry periods are influenced by interconnected atmospheric dynamic and thermodynamic mechanisms and air-sea teleconnections of various spatiotemporal scales, investigations of these interactions and their possible influences on SLCs are appropriate for future studies.

3.6.3. Seasonality of Extreme Snow Level Changes

Extreme SLCs also exhibit seasonality, with the largest number of extremes, both rises and falls, detected in December through February (Fig. 3.4e-f). Minimum counts occur during the first and last month of the season, October and April. For instance, 2-4.7 and 2.3-2.8 times as many extreme +SLCs and -SLCs, respectively, are detected during February (a total of 33 and 25, respectively) compared to during October and November (early-season months). Further, February contains ~3.3 and 4 times the total number of extreme snow level rises and falls, respectively, that occur during April (late-season month).

Slightly elevated medians for extreme snow level rises occur in February (~590 m) and April (~600 m), ~10-150 m larger than medians for the five other months assessed. October through March experience peak maximum extreme +SLCs of ~1600-1710 m. For October, December, and March, extreme +SLC maxima that are roughly double the magnitude of respective maxima for extreme -SLCs occurred (Fig. 3.4e-f). Peaks in the number of exceptional +SLCs occur during January and February, with total counts of 5 and 12, respectively (Fig. 3.5e). For -SLCs, November and January contain the largest number of exceptional SLCs, a total of 4 each (Fig. 3.5f).

3.6.4. Spatiotemporal Relationship of Extreme Snow Level Changes

An inverse relationship between median snow level and latitude has been described in previous studies (e.g., Henn et al. 2020, Chapter 2 of this dissertation). As an example, during the high-impact 2019 Valentine's Day Event, base snow levels and those following the first extreme snow level rise were ~100-300 m higher at New Exchequer than those at Colfax (Fig. 2.3 of this dissertation). Higher snow levels mean the atmosphere remained warmer or above freezing to a slightly greater atmospheric depth at New Exchequer, which is ~150 km southeast of Colfax at an elevation 385 m lower than that of Colfax (Fig. 3.2).

Results centered on the latitudinal variation of extreme SLCs also support findings suggesting higher-latitude regions have warmer snow levels (Fig. 3.4a-b). Northern radars typically receive more water-year total precipitation than southern radars, contributing to a larger number of snow level samples overall for identifying extreme SLCs (refer to Figs. 2.6a and 2.10a of this dissertation). These increased sample sizes at northern radars may result in part because the radars are positioned within primary AR pathways (e.g., Rutz et al. 2015) and/or regions slightly upwind of Sierra Nevada slopes (i.e., contributing to orographic precipitation enhancements). Snow levels, however, do not exist during solely snow-containing precipitation periods, which are more likely at climatologically-cooler and higher-elevation regions.

Evidence of a latitudinal dependence emerges when considering counts for extreme SLCs (Fig. 3.4a-b). There is a notably large number of extremes detected at higher-latitude mountain foothills radars (Happy Camp, Shasta Dam, Oroville, Colfax, New Exchequer Dam) compared to Sierra-foothills radars further south (Pine Flat Dam, Kernville, San Bernardino) and those nearer the coast (San Luis Reservoir and Saint Helena). For example, Oroville experienced 5.2 times more extreme +SLCs over all six cool seasons than Pine Flat Dam. Happy Camp saw nearly three times more extreme snow level falls than Kernville. Happy Camp and Saint Helena had the highest-magnitude maximum extreme snow level rises (1650 m and 1714 m, respectively), but substantially lower-magnitude maxima for extreme snow level falls (-848 and -471 m).

When considering exceptional SLCs instead of extremes, a dependence on latitude or geographic location is less clear (Fig. 3.5a-b). Albeit, the three southmost radars (Pine Flat Dam, Kernville, San Bernardino) experience fewer exceptional +SLCs compared to the five northmost radars (Happy Camp, Shasta Dam, Oroville, Colfax, New Exchequer Dam). Additionally, near-coast Saint Helena yields slightly elevated exceptional +SLC counts more similar to those of its downwind neighbors, Oroville and Colfax (3 compared to 5 and 6, respectively). Colfax is subjected to the greatest number of exceptional SLCs, 6 rises and 4 falls.

By examining extreme SLCs occurring across radar sites (Figs. 3.6 and 3.7), we observe relationships between geographic location, and the total percentage of SLCs simultaneously occurring at another site (within ± 6h). We also note there are relationships across radars that involve extreme SLCs and anomalous magnitudes for maximum SLC values surrounding each extreme SLC period (average of maxima, with one max per time-matched extreme SLC). Results reveal these relationships are stronger for extreme snow level rises compared to extreme falls, and for radars in closer proximity to one another as well as those along the same diagonal southwestern to northeastern pathway. For instance, during the ± six-hour windows surrounding extreme snow level rises at Colfax, the mean magnitudes for all +SLC maxima at Oroville and New Exchequer Dam are also elevated (Fig. 3.6).

In this case, Oroville's mean SLC maximum registers as extreme (470 m) while the maximum at New Exchequer is only slightly less than the 400-m minimum threshold for extremes (370 m). These two SLC-averaged maxima are notably more similar to the maxima for Colfax (~590 m) than maxima for other sites. Of the 23 extreme snow level rises at Colfax, 20 (~87%) were time window-matched (within ± 6h) with observed +SLC values at Oroville and 15 (~65%) at New Exchequer Dam (Fig. 3.6). A larger percentage of Colfax extreme +SLCs were also time-matched at sites to the north, Shasta Dam and Happy Camp (~78% and 52%, respectively), compared with those to the south, Pine Flat Dam, Kernville, San Bernardino (13-35%). Upstream at San Luis Reservoir and Saint Helena, counts for time-matched rise periods are more similar to those of the northernmost two sites (12 and 14, or 52% and 61%, respectively). At these nearer coast sites, mean +SLC maxima are ~3.4 and 2.5 times smaller, respectively, than the maxima for Colfax (~171 m and 233 m, respectively) which are also similar in magnitude to those of northern radars, Happy Camp and Shasta Dam (~200-230 m).

We find SLC time-matched percentages and maximum magnitudes are not always symmetric when examining results for two radars (e.g., when assessing extremes at one versus another). For example, when considering extreme +SLCs at New Exchequer Dam (13 total), ~54% are time-matched with +SLCs at Pine Flat Dam. This is compared to ~100% of extreme rises at Pine Flat Dam (5 total) returning time-matched +SLCs at New Exchequer Dam. The two mean SLC maximum resulting from these cases, however, are similar to one another, ~240 m compared to 260 m, respectively. Meanwhile, time-matched SLC percentages when considering Colfax extreme +SLCs matched with SLCs at Oroville and the reverse are more similar to one another, ~87% and 85%, respectively. Resulting means for +SLC maxima for both scenarios are also similar to one another and are categorized as extreme (~470 m and ~440 m, respectively).

While 85% of extreme +SLCs at New Exchequer Dam are matched with a +SLC value to the north at Colfax, ~78% are matched upstream at San Luis Reservoir and 46% at Saint Helena. Notably smaller percentages of these extreme +SLCs are time-matched at the southernmost two inland radars, Kernville and San Bernardino (38% and 23%, respectively). In this scenario, Colfax and Saint Helena each return a mean matched-maximum +SLC value flagged as extreme (457 m and 531 m). Additionally, mean +SLC maxima for Happy Camp and Oroville to the northwest are just shy of extreme (385-395 m). For upstream San Luis Reservoir, the mean SLC maximum is ~260 m, more similar to maxima resulting for the southernmost three radars.

Similar patterns, where the likelihood of mean SLC maxima exceeding the minimum threshold for extremes increases for radars in closer proximity to the radar in question, also emerge for other sites. For example, during extreme +SLCs (± 6h) at the two nearer-coast sites, San Luis Reservoir and Saint Helena, we note elevated +SLC maxima at downwind radars, Colfax (~307 and 370 m, respectively) and New Exchequer Dam (~412 and 626 m, respectively). It is also important to note the small sample size for extreme +SLCs, especially for the two nearer-coast sites (7 and 6, respectively) and the southernmost three radars (5-6 total).

Results considering extreme -SLCs and their mean -SLC maxima and time-matched -SLC percentages differ from those considering extreme +SLCs. Mean -SLC maximum values for ± 6h windows surrounding extreme -SLCs are smaller overall, with only one exceeding a magnitude of 400 m (Fig. 3.7). This exception appears when considering the mean -SLC maximum for Colfax during extreme -SLCs at upstream Saint Helena (2 extreme falls total). The mean -SLC maximum within the time windows surrounding each extreme fall is actually 2.5 times smaller at Saint Helena itself (-458 m) than at Colfax, where it registers as exceptional (-1145 m with both extremes matched). Resultant mean maximum -SLC magnitudes at Shasta Dam and Oroville are near-extreme, ~345-350 m. When considering the reverse scenario, i.e., extreme -SLCs at Shasta Dam and Oroville, mean -SLC maxima for Saint Helena and San Luis Reservoir are of relatively small magnitudes (-120 m to -185 m).

As was true (and more pronounced) for extreme +SLCs, the percentage of time-matched extreme -SLCs often increases with proximity to the extreme SLC site, or when the two evaluated radars exist within a similar geographic subregion (e.g., both nearer the coast, or along the western base of the southern Sierra) or within the same southwest-northeast transect. For instance, ~91% of extreme falls at Oroville are matched with a -SLC maximum at Colfax, while 87% of Colfax's extreme falls are matched at Oroville (Fig. 3.7). Additionally, as another example, 100%, 75%, and ~88% of the extreme snow level falls at San Luis Reservoir (8 total) return time-matched -SLCs at downwind New Exchequer Dam, Colfax, and Oroville, respectively (average SLC maxima: ~230-300 m). Both time-matched extreme -SLC percentages and -SLC maxima for these three downwind radars are larger than values for other radars.

3.6.5. Vertically-Integrated Moisture Flux and Extreme Snow Level Changes

When considering +SLCs, radar-averaged (mean) IVT maxima associated with extreme SLCs are consistently larger than means for non-extreme SLCs at the same radar (Fig. 3.8a). Extreme +SLC-matched IVT maxima range from ~18 kg m^{-1} s^{-1} (Saint Helena) to ~155 kg m^{-1} s^{-1} (Oroville) larger than their respective non-extreme radar-averaged IVT maxima. Only two sites (Colfax and Saint Helena) result in elevated IVT maxima for extreme +SLCs that are less than ~40 kg m^{-1} s^{-1} larger than IVT maxima for respective non-extreme +SLCs. The median and mean of all 10 IVT maximum differences for +SLCs are ~60 and 70 kg m^{-1} s^{-1}, respectively. When assessing -SLCs, the median and mean of all 10 difference values are a tad larger, ~74 and 81 kg m^{-1} s^{-1}, respectively (Fig. 3.8b). For two radars, averaged IVT maxima associated with extreme -SLCs are slightly smaller than means linked with non-extremes (Colfax and New Exchequer Dam, -0.2 and -66 kg m^{-1} s^{-1}, respectively).

We find the largest positive difference between extreme and non-extreme -SLC IVT maxima at Saint Helena (nearly +260 kg m^{-1} s^{-1}). For +SLCs, however, Saint Helena has the smallest difference between extreme and non-extreme means. This dissimilarity may stem from the site's small sample size for extremes (Table 3.1, Fig. 3.4a-b) and notable differences in results when considering snow level rises versus falls. For example, the median and maximum magnitude for extreme snow level rises at Saint Helena are ~185 m and ~1240 m larger than the extreme fall median and maximum, respectively (Fig. 3.4a-b).

Through significance testing, we find three radars each for snow level rises and falls that have significant IVT exceedance likelihoods, i.e., a < 5% chance of resampled radar-averaged IVT maxima for non-extreme SLCs exceeding means for extremes (refer to triangles in Fig. 3.8). With the exception of Happy Camp, sites resulting in significant exceedance likelihoods differ between positive and negative SLCs; the three northernmost radars for snow level rises, and a southern and nearer-coast radar (San Bernardino and Saint Helena) for falls.

In summary, we find the majority of individual radar-averaged IVT maximum values are larger during extremes compared to non-extremes (Fig. 3.8). We also assessed SLCs across all 10 radars to examine how SLC magnitudes and percentages of extreme SLCs vary depending on IVT maxima bins (average of each maximum IVT value found within ± six hours of each SLC for all radars; Fig. 3.9). The percentage of extreme snow level rises is at least four times larger for the largest-magnitude maximum IVT bin (1000-1100 kg m^{-1} s^{-1}) than for a reduced-magnitude IVT bin (between the 0-100 and 500-600 kg m^{-1} s^{-1} bin), ~2.9% compared to 0-0.7%, respectively (Fig. 3.9a). Given the available snow level observations, there is a direct, nonlinear relationship between maximum IVT magnitude and the likelihood of detecting an extreme +SLC (Fig. 3.9a).

For -SLCs, relationships between IVT maxima, mean SLC magnitudes, and occurrences of extremes are not as prominent or consistent (Fig. 3.9b). As noted for +SLCs, however, results for -SLCs suggest larger-magnitude IVT maxima were associated with a larger percentage of extreme snow level falls when compared to smaller-magnitude IVT maxima. These percentages are 0.9% and 2.3% for the largest and second-largest IVT bins, respectively, compared to ~0-0.5% for smaller-magnitude IVT bins (Fig. 3.9b).

Computed 90% confidence intervals suggest, if additional snow levels are considered through resampling (allowing for increased sample sizes), the resulting percentages for extreme SLCs within periods of large-magnitude IVT maxima (800-1100 kg m^{-1} s^{-1}) can fall within a fairly wide range of values (Fig. 3.9). Narrower confidence intervals result for smaller-magnitude IVT maxima (100-800 kg m^{-1} s^{-1}). This result suggests that extreme SLC percentages associated with smaller-magnitude IVT maxima bins are more likely to closely predict percentages resulting from a larger pool of samples (i.e., a bootstrap-expanded snow level dataset).

Similar to percentages of extreme SLCs, the mean magnitude of +SLCs and -SLCs also increases as the magnitude of SLC-averaged IVT maxima bins increases (Fig. 3.9). Additionally, wider confidence intervals and smaller sample sizes result for larger-magnitude IVT maxima bins compared to smaller-magnitude bins. Further, mean SLC magnitude increases more steeply with increasing IVT maxima for snow level rises compared to falls (Fig. 3.9). Maximum magnitudes for mean SLCs (161 m and 152 m for +SLCs and -SLCs, respectively) exist within the two largest-magnitude IVT maxima bins. These peak mean SLC magnitudes are ~1.5-2 times larger than respective magnitudes during the two smallest-magnitude IVT bins.

3.6.6. Atmospheric Rivers and Extreme Snow Level Changes

Because landfalling ARs can uniquely alter near-surface air temperatures and atmospheric conditions, we also consider relationships between SLCs and AR events using the Guan and Waliser (2015) detection method (Fig. 3.10). ARs are detected at radar-matching grid points for at least 60% of extreme positive and negative SLCs, with larger percentages resulting at certain radars (minimum of ~60% at New Exchequer Dam and Colfax, respectively). ARs occur during 80-100% of extreme snow level rises at five sites (Oroville, Pine Flat Dam, Kernville, San Luis Reservoir, Saint Helena). The same range of larger percentages exists for extreme falls at only two sites (Oroville, and Saint Helena). Extreme-matched AR association percentages are larger than the narrower percentage ranges for non-extreme snow level rises and falls (~35-60% range for each).

For only one radar, Colfax, the percentage of extreme snow level falls occurring during an AR is only slightly larger than the equivalent value for non-extreme falls (~60% versus 58%). For all other cases, AR associations are ~15-55 or ~15-40 percentage points larger for extreme positive and negative SLCs, respectively, than corresponding non-extreme values. We compute AR association median percentages for extreme rises and falls of ~77% and 75%, respectively, and for non-extreme rises and falls of ~50% and 47%, respectively (means also fall within similar ranges). Results also suggest an overall tendency for both the number of non-extreme and extreme SLCs to peak at northern radars and remain smaller for southern sites (Fig. 3.10). Smaller counts that are more similar to those of southern Sierra foothills or inland radars are also observed at the two nearer-coast sites (San Luis Reservoir and Saint Helena). Total SLC counts for each radar are two to four orders of magnitude larger for non-extreme changes compared to extremes.

Through bootstrap significance testing (Section 3.5.2), we find that the likelihood of resampled AR association percentages for each radar for non-extremes exceeding those of extremes (i.e., exceedance likelihood, not shown here) fell within a similar range of values for positive and negative SLCs, ~35-60%. A 0% exceedance likelihood for both positive and negative SLCs, however, results when requiring that SLCs must simultaneously occur at all five key radars instead of only one. This means there is a stronger association between AR periods and extreme SLCs (compared to non-extremes) occurring across key radars, i.e., it is virtually impossible for the AR association for non-extreme SLCs occurring at all five key radars to exceed the AR association for extreme SLCs.

This study does not suggest all AR time periods contain one or more extreme SLCs, but rather presents evidence that extreme SLCs are more likely to occur during ARs (Fig. 3.10a and c). Because, by definition, ARs are plumes of enhanced column-integrated moisture (IVT typically > 250 kg m^{-1} s^{-1}) and results suggest larger-magnitude SLCs are associated with larger IVT maxima (Figs. 3.8 and 3.9), findings indicating a stronger association between AR periods and extreme SLCs compared to non-extreme SLCs are well-supported (Fig. 3.10).

Complex interactions involving atmospheric, ground surface, soil, and hydrologic conditions are at play during ARs. Additional factors that determine resulting precipitation and impacts include AR intensity, speed, and orientation relative to topographic features (upslope water vapor flux; e.g., Neiman et al. 2002; Hecht and Cordeira 2017). ARs affecting the western U.S. are typically situated within the warm sector of the extratropical cyclone, behind a warm frontal system and ahead of a cold front (e.g., Zhu and Newell 1998; Ralph et al. 2004, 2005, 2018). Intruding air masses can contribute to changes in near-surface temperatures through the horizontal advection of warm or cool air and by altering the stability of the atmosphere. Further, during ARs, evaporation, cloud formation, and precipitation processes can affect atmospheric temperatures (thus snow levels) through latent heating or cooling.

In this dissertation study, however, we compute SLCs within one-hour time increments which means the key atmospheric processes contributing to each extreme SLC must have an exceptionally rapid and large impact on low-level air temperatures. For future studies, we suggest further explorations of localized thermodynamic processes, frontal systems and embedded ARs associated with extratropical cyclones, as well as larger-scale ocean-atmosphere interactions which may also influence extreme snow level rises and falls.

3.7. Acknowledgements

Joel R. Norris, Anna M. Wilson, Benjamin J. Hatchett, F. Martin Ralph, and Brian Henn contributed to materials provided in this dissertation chapter. Chapter 3, in part, is being prepared for submission for publication as: Osborne, T.C., J.R. Norris, A.M. Wilson, B.J. Hatchett, F.M. Ralph, and B. Henn. The dissertation author was the primary investigator and author of this material. Authors express gratitude to NOAA ESRL, the CA-DWR, and CIRES for providing valuable snow level observations and details. We thank Bin Guan and Duane Waliser of NASA Jet Propulsion Laboratory for providing their AR detection catalogue, and Zhenhai Zhang of CW3E for providing updates to include the 2020 water year. We also thank Edwin Sumargo, Brian Kawzenuk, Chad Hecht, and Forest Cannon of CW3E for helpful input during this study. Additionally, authors value the continued support of Art Miller of SIO at UC San Diego, Amin Dezfuli of NASA Goddard Space Flight Center, and personnel of the NOAA California Nevada River Forecast Center.

3.8. Data Availability Statement

The intrastorm SLC dataset used in this chapter was provided by Osborne et al. (described in Chapter 2). Brian Kawzenuk of CW3E computed IVT values using NASA MERRA-2 variables made available by the NASA Goddard Earth Sciences (GES) Data and Information Services Center (DISC) at https://disc.gsfc.nasa.gov/datasets. The AR detection code and catalogue, housed here: https://ucla.box.com/ ARcatalog, was provided by Bin Guan.

3.9. Figures and Tables

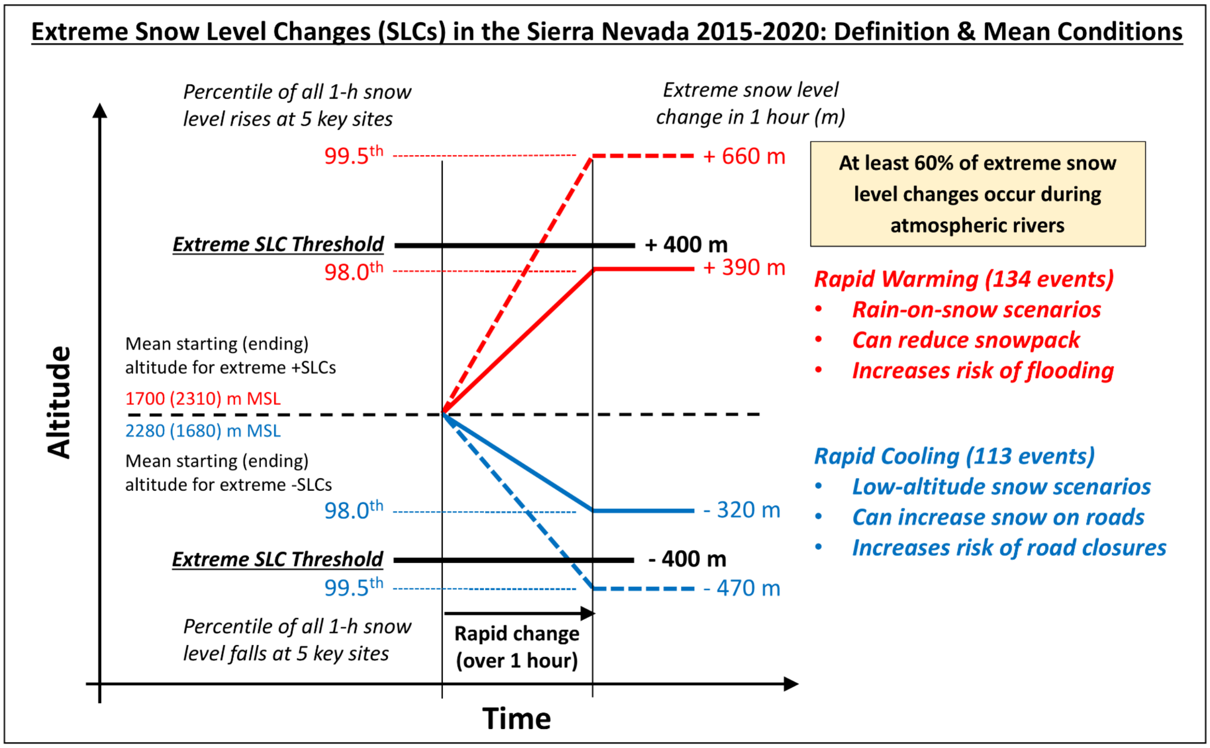

Figure 3.1. Schematic illustration introducing the definition and mean conditions of extreme snow level rises (in red) and falls (in blue). Results are based on one-hour SLCs at five key Sierra Nevada radars during cool seasons of water years 2015-2020. This interpretation of snow level altitude versus time is centered at a hypothetical Sierra foothills FMCW radar site. The bold dashed black line separates the values for extreme rises (top half; red) and falls (bottom half; blue). Included are lines denoting the 98th and 99.5th percentile value for all (extreme and non-extreme) positive or negative one-hour SLCs computed. SLC thresholds used to define extreme one-hour SLCs (magnitude ≥ 400 m) are shown as bold solid black lines. The mean starting and ending altitude for extreme +SLCs, or average base altitude at which extreme snow level rises begin or end at the five key sites, is shown in red to the left above the dashed black line. The mean for extreme falls is shown in blue beneath the dashed black line. All computed percentiles and mean starting altitudes have been rounded to the nearest 10. Text within the rightmost column indicates the total number of extreme rises and falls at all 10 radars (in parentheses), and lists possible hydrologic and societal impacts of extreme SLCs.

Table 3.1. Details of the 10 FMCW S-band radars (provided by NOAA PSL) and SLC statistics resulting from this study. Bolded text in the first two columns is used for key radars within hydrologically high-impact Sierra Nevada basins. Columns following the third column provide statistics when solely assessing one-hour +SLCs (before comma) or -SLCs (after comma). In the fourth column (SLC 98th percentiles), additional results considering all SLCs are included in parentheses. The first and second value in the parentheses result from considering all SLCs (both sign and magnitude) and from taking the absolute value of all SLCs (magnitude only), respectively. Where indicated, only extreme (ext.; magnitude ≥ 400 m) or exceptional (exp.; magnitude ≥ 800 m) one-hour SLCs are considered. All values are rounded to the nearest whole number.

Site Name	Site Code	Install Date	1-h SLC 98th Percentile	Number Ext. 1-h SLCs	Ext. 1-h SLCs Mean (m)	Ext. 1-h SLCs Median (m)	Ext. 1-h SLC Standard Deviation (m)	Number Exc. 1-h SLCs
Happy Camp	hcp	02 Feb 2012	298, -313 (227, 308)	20, 28	739, -520	658, -487	365, 97	4, 1
Shasta Dam	**std**	09 Dec 2009	359, -283 (257, 306)	22, 13	569, -574	509, -505	168, 270	2, 1
Oroville	**ovl**	08 Dec 2011	399, -320 (317, 361)	26, 11	601, -538	596, -522	243, 113	5, 0
Colfax	**cff**	10 Dec 2008	417, -338 (303, 363)	23, 15	638, -702	508, -528	290, 385	6, 4
New Exchequer Dam	**ner**	03 Dec 2010	391, -323 (304, 362)	13, 9	648, -560	522, -538	304, 132	3, 1
Pine Flat Dam	**pfd**	06 Dec 2010	336, -335 (261, 335)	5, 8	564, -517	569, -477	138, 109	0, 0
Kernville	knv	02 Jan 2012	352, -319 (264, 334)	6, 9	581, -504	570, -481	165, 86	1, 0
San Bernardino	sbo	12 Mar 2013	349, -366 (281, 360)	6, 10	678, -625	507, -511	461, 359	1, 1
San Luis Reservoir	slr	02 Apr 2013	357, -353 (292, 353)	7, 8	510, -674	437, -723	122, 213	0, 3
Saint Helena	sth	09 July 2014	303, -283 (256, 288)	6, 2	904, -458	643, -458	583, 18	3, 0
5 Key Radars			386, -315 (289, 347)	89, 56	607, -591	508, -518	243, 255	16, 6
All 10 Radars			361, -319 (269, 335)	134, 113	637, -573	525, -502	295, 224	25, 11

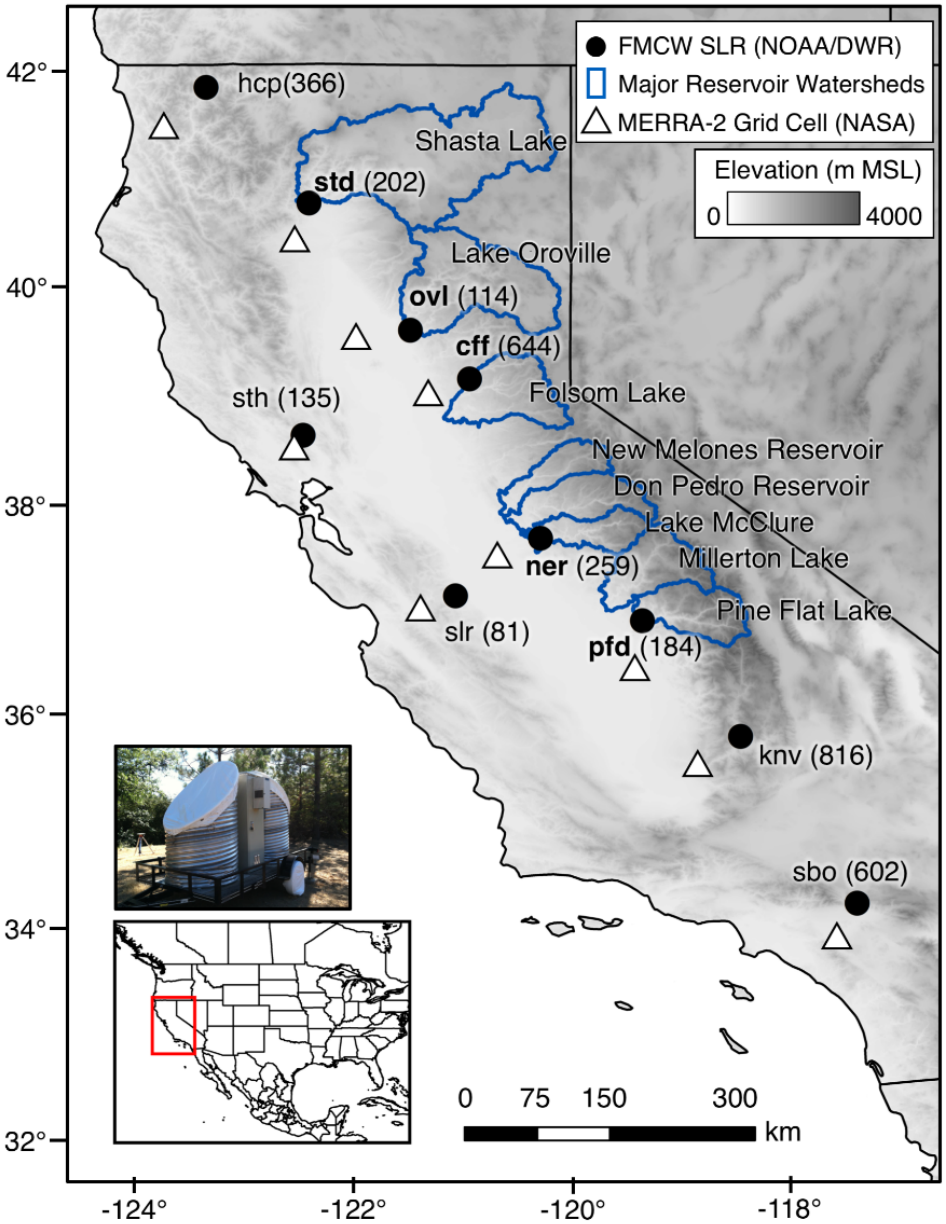

Figure 3.2. Basemap of California including 10 FMCW radar study sites (black circles), with radar elevations in parentheses (m MSL). NASA MERRA-2 reanalysis grid cells used in IVT and AR analysis are also shown (white triangles outlined in black). Eight hydrologically-important watersheds within the Sierra Nevada are outlined in blue and labeled. Within these basins, key radars are indicated by bold text. A photograph of the vertically-oriented Colfax radar is also featured (provided by NOAA ESRL).

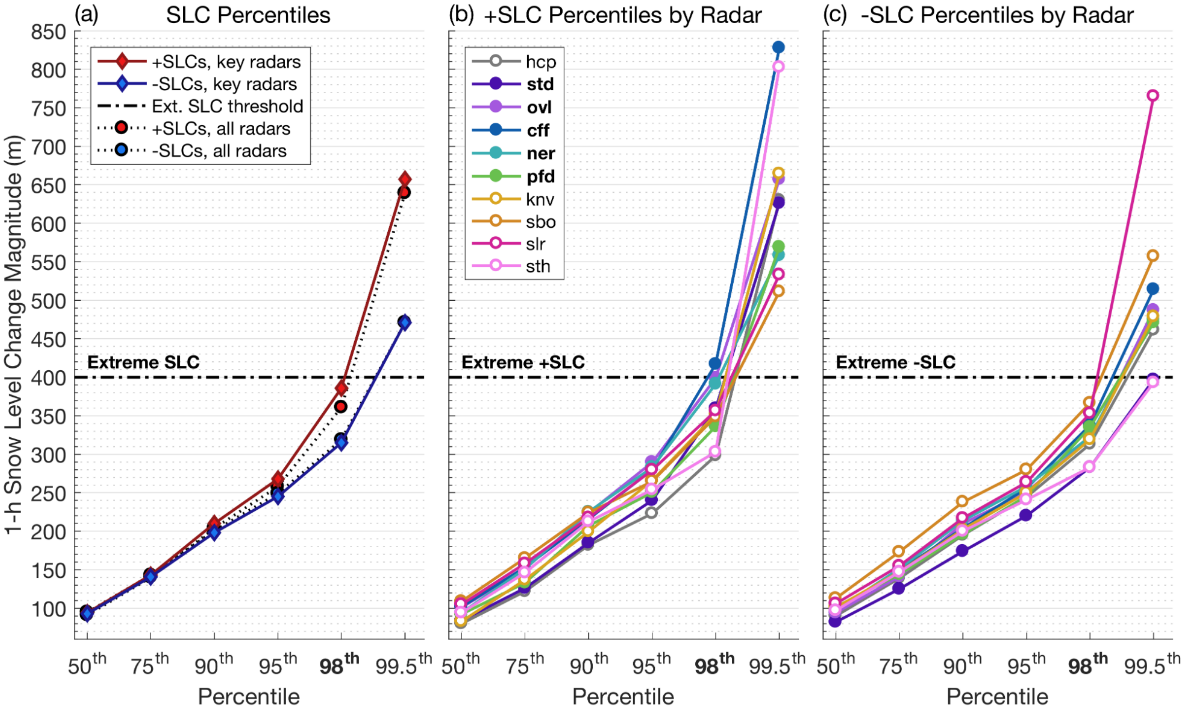

Figure 3.3. Computed one-hour SLC percentiles, and the threshold determined to define extreme changes, i.e., the 400 m-magnitude (horizontal black dash-dot line). (a) Spatiotemporal mean percentiles for snow level rises (red markers) and falls (blue markers) detected at the five key radars (diamonds) and all 10 radars (circles) considered in this study. (b) and (c): Mean percentiles for positive and negative SLC magnitudes, respectively, at each of the 10 FMCW radar sites. Note that only a single maximum SLC within each one-hour time window is used to compute percentiles. In (b) and (c), text labels for key radars are bolded and their corresponding circular markers are color-filled. Note that the minimum threshold for *extreme* was determined by considering 98th percentiles (bolded label along the x-axis). Radar sites are ordered latitudinally from north to south, with nearer-coast sites (slr and sth) included at the end.

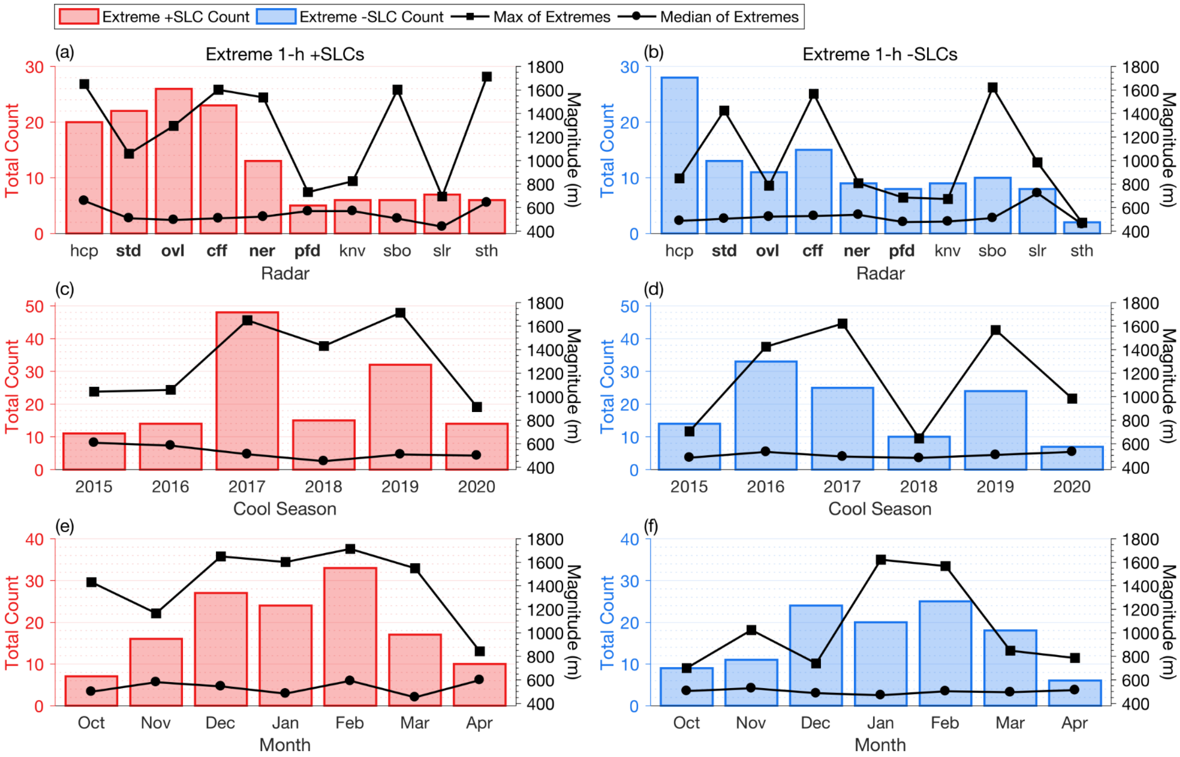

Figure 3.4. Extreme SLC counts (left y-axes) and maximum and 50th percentile values (right y-axes) by radar, (a) and (b), cool season, (c) and (d), and month, (e) and (f). Radars in (c) and (d), from left to right, are ordered from north to south, with near-coast radars included in the rightmost two columns and key radars in bold text. The month assigned to each SLC is determined by considering the SLC start time in Pacific Time (local time). Counts for extreme positive SLCs are shown as vertical red bars [(a), (c), (e)] while counts for negative extremes are shown as vertical blue bars [(b), (d), (f)]. Maximum and median (i.e., 50th percentile) values for extreme SLCs are shown as black lines with filled squares and circles, respectively. The five key Sierra radars are in bold text along the x-axis in (c) and (d).

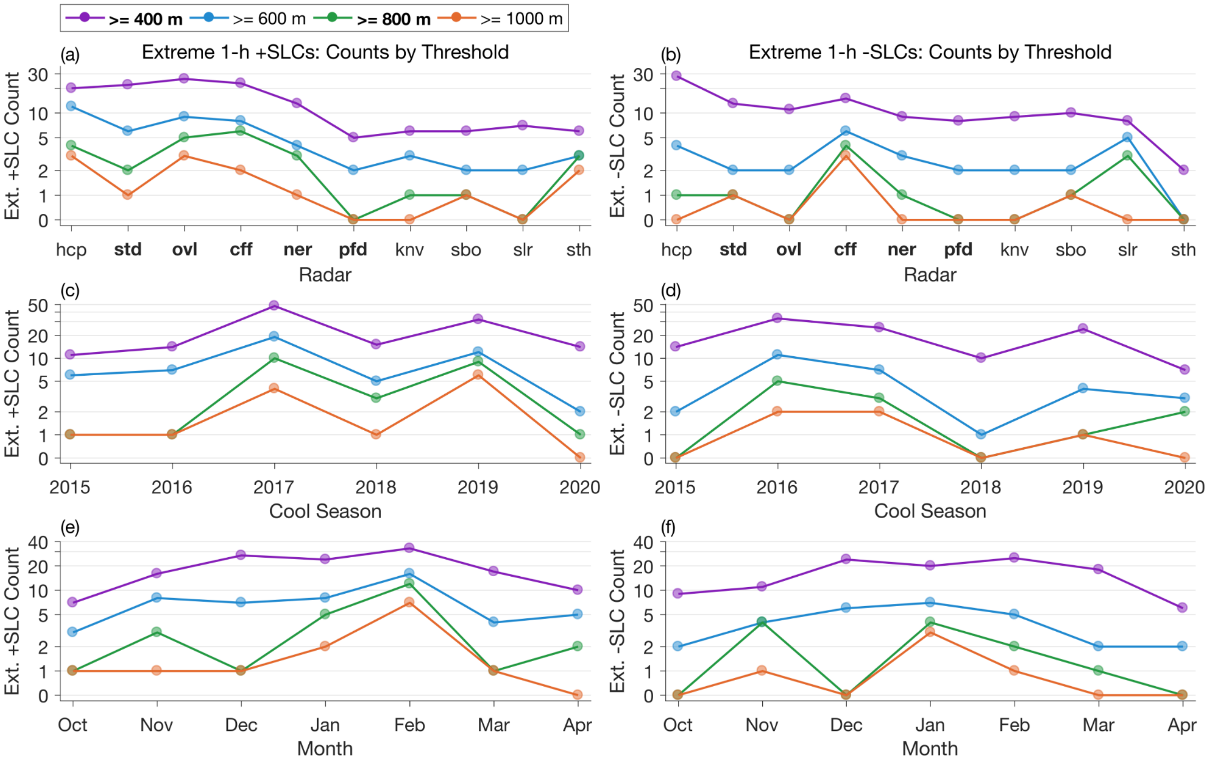

Figure 3.5. Extreme SLC counts by radar, (a) and (b), cool season, (c) and (d), and month, (e) and (f). The y-axis is shown in log form. Within each subplot, there are four lines representing the number of extreme SLCs exceeding four separate large-magnitude SLC thresholds. Extreme snow level rise counts are plotted in (a), (c), (e) while counts for negative extremes are plotted in (b), (d), (f). Along the x-axis of (c) and (d), the five key radars are bolded. Within the legend, the minimum thresholds used to define *extreme* and *exceptional* one-hour SLCs (400 and 800 m, respectively) are bolded.

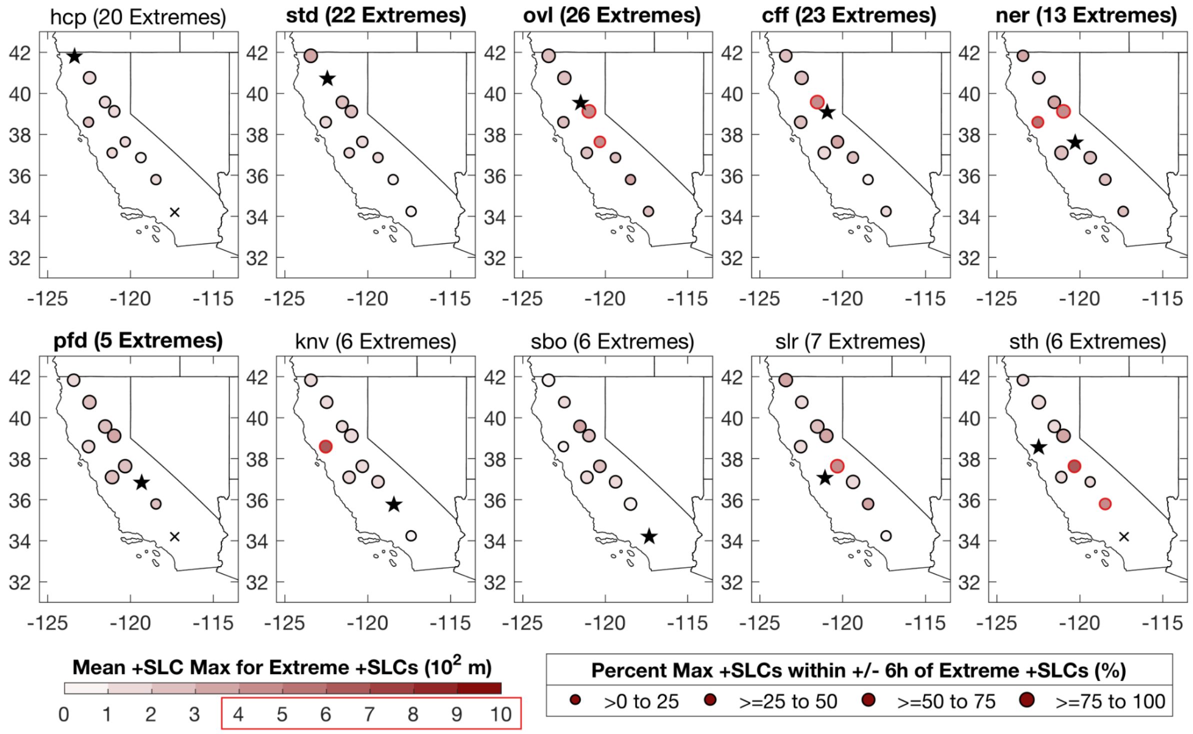

Figure 3.6. Relationships between extreme or substantial one-hour +SLCs occurring across multiple radars. For each subplot, the title and black star indicate the radar of interest, or the radar for which extreme +SLCs are assessed. For all other radars, means of the maximum +SLC magnitudes found within ± six hours of each extreme +SLC (that occurred at the radar of interest) are plotted as red-gradient circles. Each circle's gradient shade is determined based on the mean of +SLC maxima computed at the radar location (10^2 m; refer to the color bar), with one max +SLC considered per time-matched extreme. Circles are outlined in bright red when the mean +SLC maximum exists within the extreme range (magnitude ≥ 400 m). The size of each circle indicates the percentage of extreme +SLCs (at the radar of interest) that are matched with a valid +SLC maxima for each radar. The total number of extreme +SLCs is included in parentheses within each subplot title. An "x" indicates that there are no time-matched +SLCs within the confined time window surrounding each extreme. Key radars are labeled in bold text.

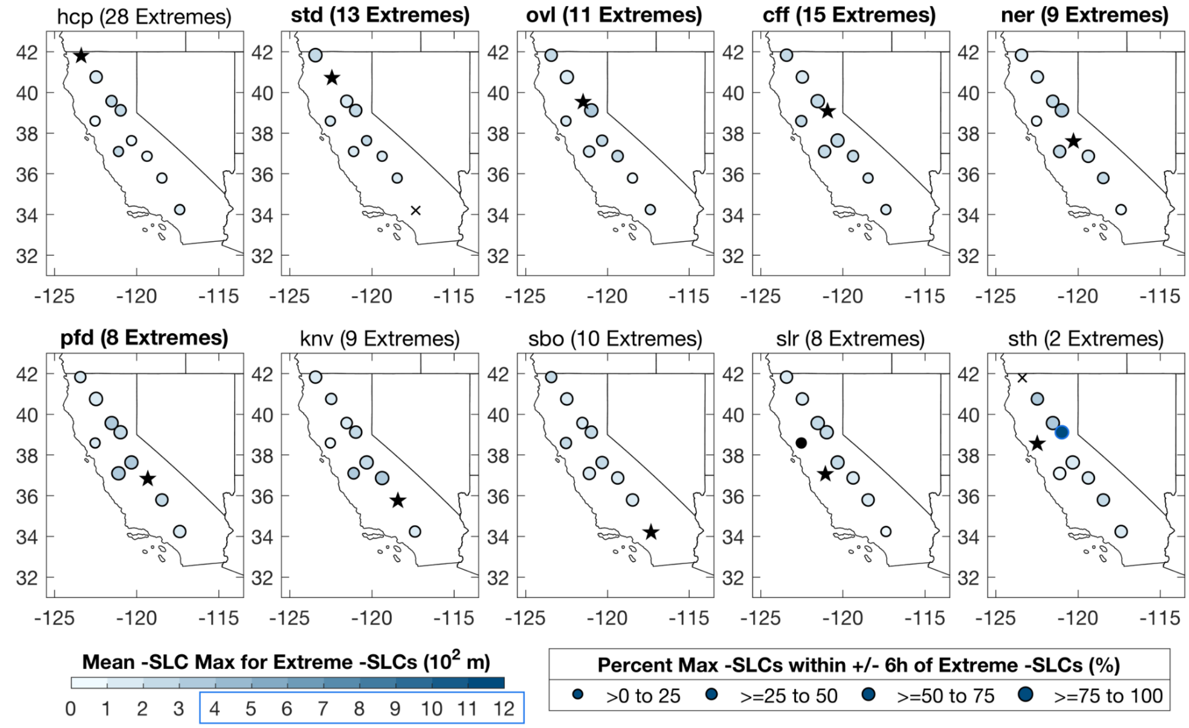

Figure 3.7. Same as Figure 3.6, but now for extreme SLC falls (magnitudes) instead of rises, with blue shading instead of red.

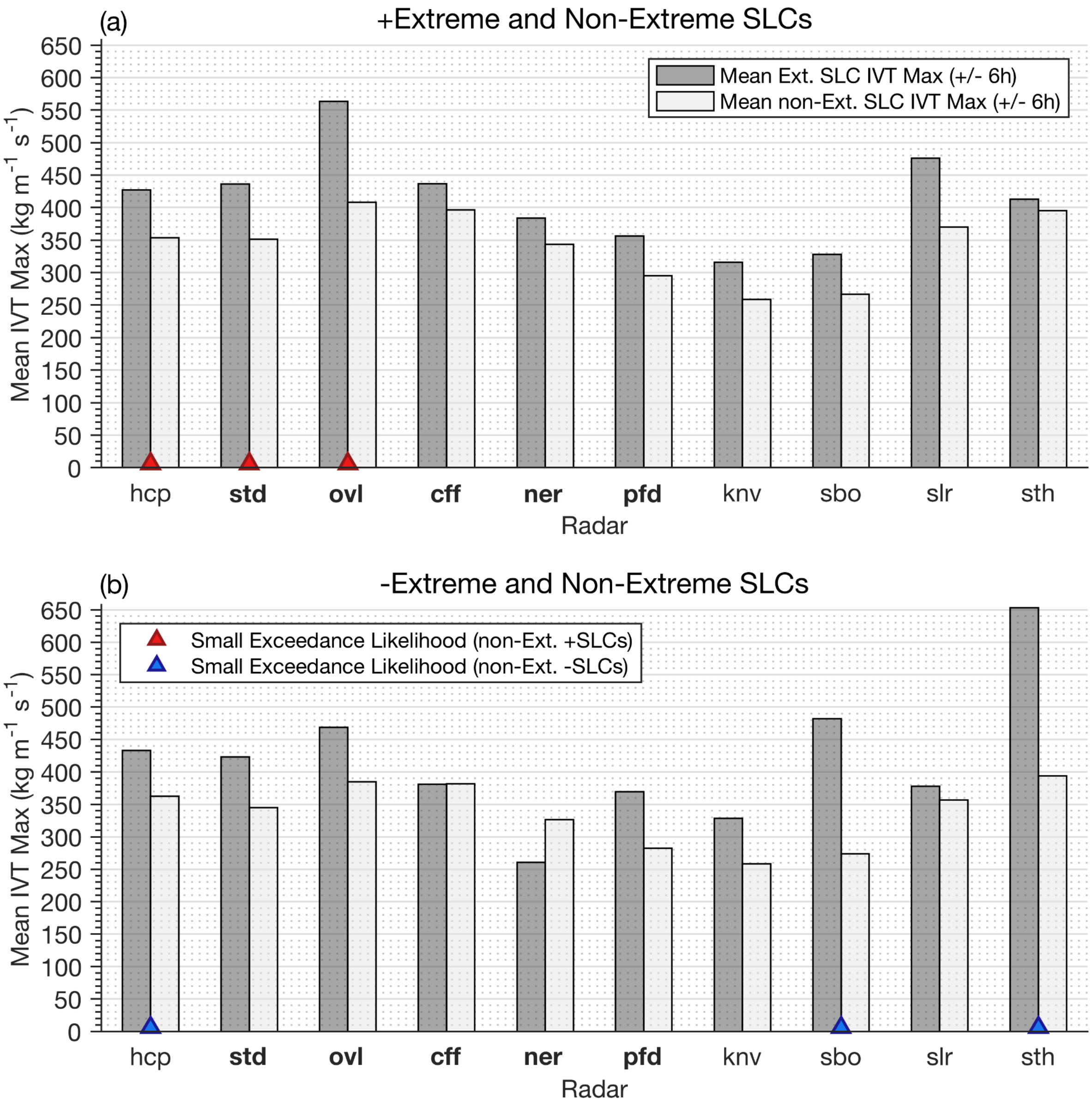

Figure 3.8. Bar plot of radar-averaged (mean) IVT maxima for one-hour snow level (a) rises and (b) falls. The maximum IVT within a ± six-hour window surrounding each SLC is considered. Lighter gray bars represent mean IVT maxima for non-extreme (non-Ext.) SLCs while darker gray bars represent values for extreme SLCs (Ext.). Red and blue triangles indicate radars for which the likelihood of a bootstrap resampled radar-averaged IVT maxima for non-extreme changes exceeding the IVT maxima for extreme changes at the same radar is small (< 5%). For details on computing the exceedance likelihood through bootstrapping (refer to Section 3.5.2). Key radar sites are shown in boldface text.

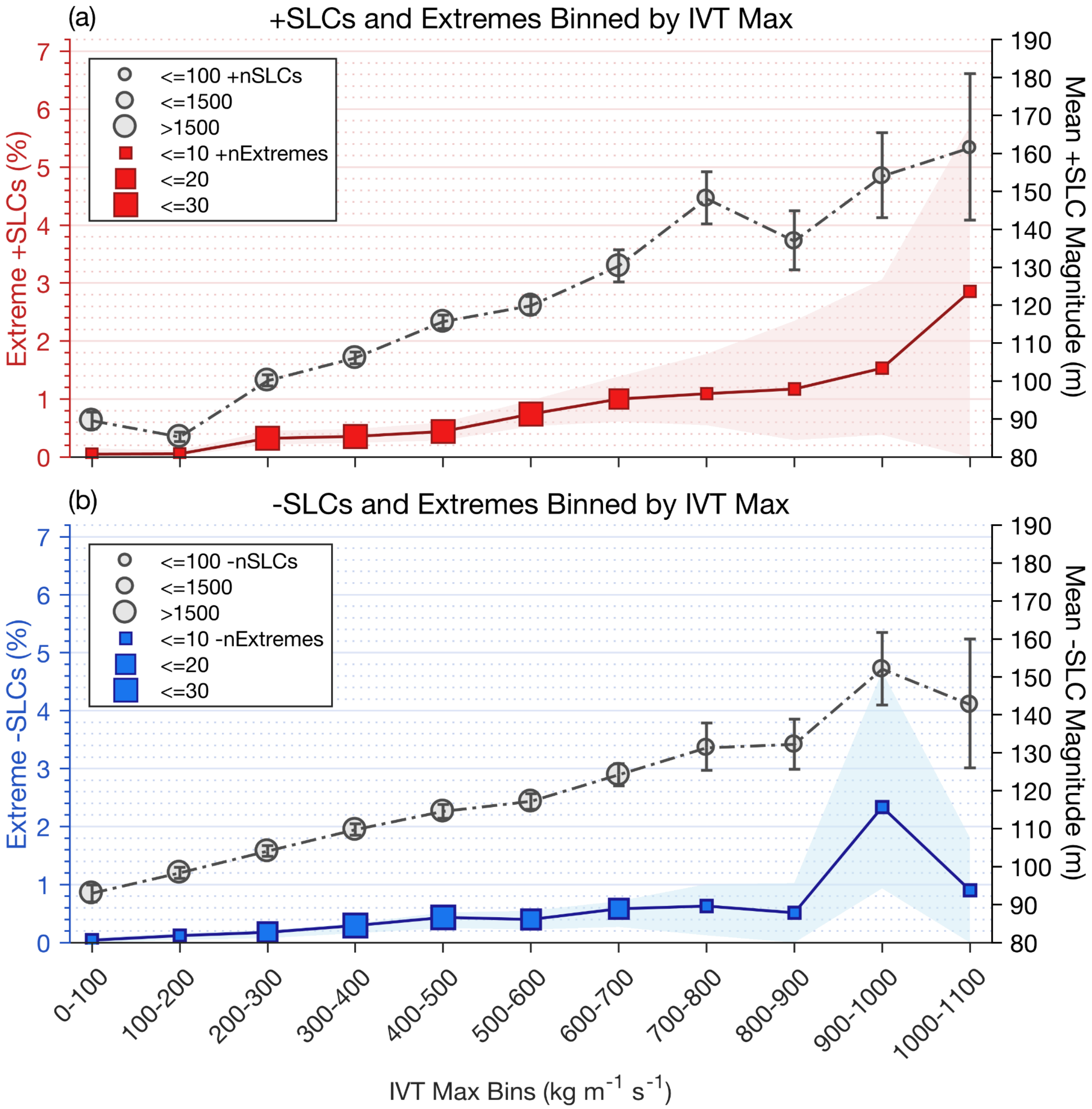

Figure 3.9. Plots of both percent extreme one-hour SLCs (left y-axis; square markers) and mean SLC magnitude (right y-axis; circle markers) for max IVT bins (x-axis). (a) Positive and (b) negative SLCs are considered separately. The averaged IVT maximum, which is the 10-radar mean of all maximum IVT values selected from the ± six-hour window surrounding each SLC (one max IVT per SLC), is binned every 100 kg m^{-1} s^{-1}. Markers for percent extreme SLCs (red and blue squares) and mean SLC magnitude (gray circles) are sized based on the number of extreme SLCs (*nExtremes*) and the number of SLC samples (*nSLCs*) within each max IVT bin, respectively. The 90% confidence intervals for percent extreme SLCs (red and blue shaded areas) and mean SLC magnitude (black vertical bars) are also included. Statistical confidence intervals are determined through bootstrap resampling methods (refer to Section 3.5.2).

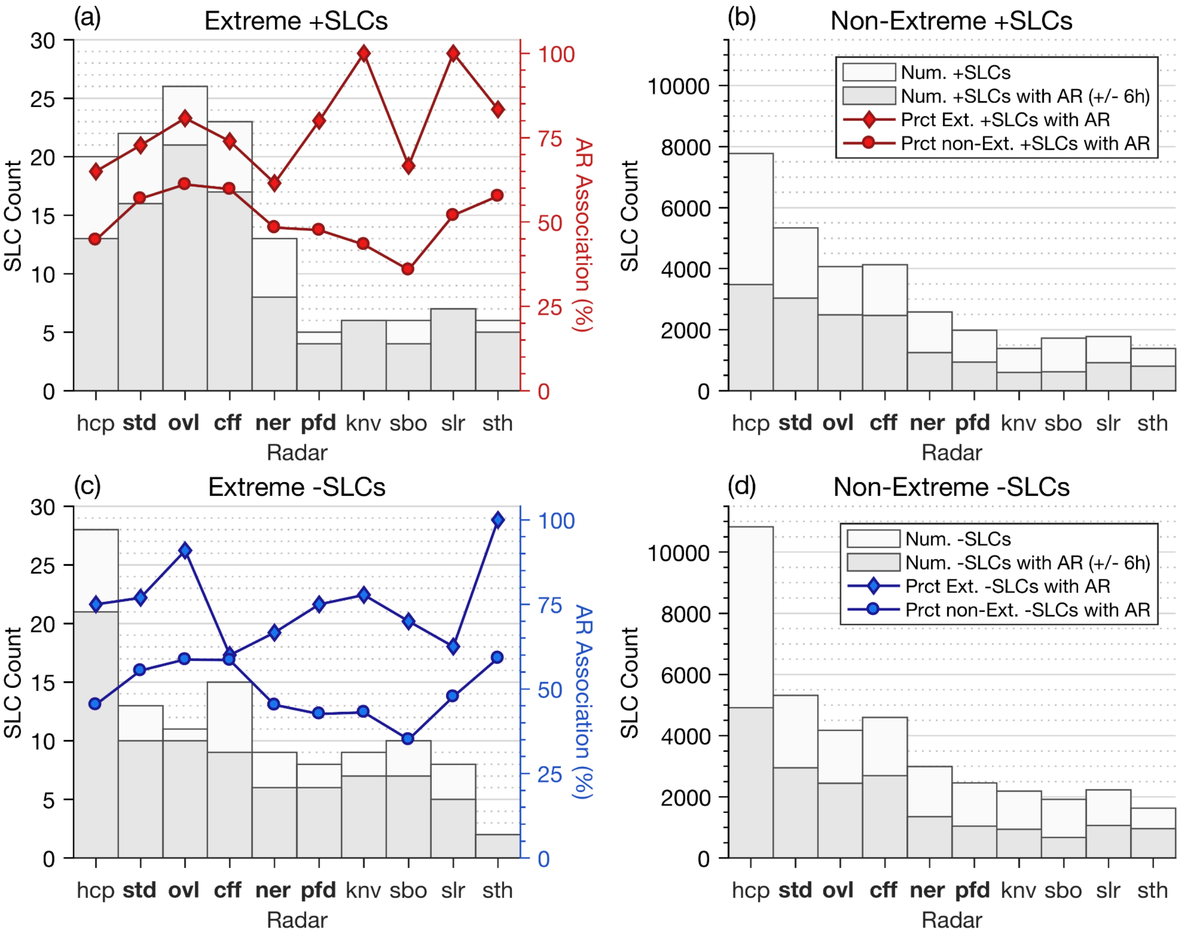

Figure 3.10. Relationship between SLCs and ARs depending on radar. Counts (*num.*) for all SLCs by radar (lighter gray bars) and for SLCs occurring with an AR within ± six hours (darker gray bars) are plotted along the left y-axis for (a) extreme and (b) non-extreme +SLCs, and for (c) extreme and (d) non-extreme -SLCs. In (a) and (c), percentages (*prct*) of extreme (diamonds) and non-extreme (circles) SLCs occurring during AR periods are plotted along the right y-axis in (a) red and (c) blue. (b) and (d) only display non-extreme SLC counts (bars), as corresponding AR association percentages are instead shown on (a) and (c), respectively, for easier comparison. Key radars are indicated in bold text.

Chapter 4

Conclusion and Future Work

This dissertation developed a robust detection algorithm and methodology to identify and describe extreme intrastorm snow level changes (SLCs). A number of these rapid, substantial vertical changes in snow level were observed during precipitation events that resulted in severe hydrometeorological and societal impacts. This work defined an extreme SLC as a rise or fall in radar-derived snow level with a magnitude ≥ 400 m which occurs within one hour. To identify and investigate extreme changes in snow level, this dissertation developed a definition and methodology to isolate semicontinuous snow level events, or periods lasting at least three hours that contain snow levels (allowing for gaps up to three hours long). Further, to minimize spurious SLC, this work established and applied a series of snow level data quality filters.

Ultimately, this dissertation provides a catalogue and characterization of extreme intrastorm SLC, semicontinuous snow level events, and all maximum SLC occurring during one and three hours. Additionally, this work described extreme intrastorm SLC in terms of spatiotemporal tendencies, uncovering variations in the magnitude and number of extremes from one radar, cool season, and month to another. A total of 1492 semicontinuous snow level events were identified for cool seasons 2015-2020 across 10 California Snow Level Radars. Within these events, more than 70,000 one-hour SLCs and nearly 65,000 three-hour SLCs were computed and assessed. Median magnitudes for SLC fell between 90-95 m for one-hour rises and falls separately. Results highlight the wide range of magnitudes that intrastorm snow level rises and falls span, from less than 100 m to 1600 and 2000 m, respectively.

Further, this work identified and examined a total of 134 and 113 extreme snow level rises and falls, respectively, which occurred during semicontinuous events. The number of extreme SLC occurrences exhibited a latitudinal and longitudinal dependence. More specifically, radars in northern sites and in western Sierra foothills regions provided a larger number of extreme SLC compared to those further south or nearer the coast. Additionally, compared to an extreme snow level fall at any of the 10 radars, a substantial or extreme snow level rise at one radar was more likely to also occur (within ± six hours) at another radar positioned within a similar geographic subregion (i.e., both nearer the coast or part of the southern Sierra foothills), or along the same southwest-northeast transect.

Both extreme snow level rises and falls were more likely to occur during anomalously wet years, and during December through March, most notably in December and February. This dissertation identified similar patterns in peak counts by cool season, radar, and month for intrastorm SLCs and semicontinuous snow level events. Results also provided evidence that exceptional (magnitude ≥ 800 m) snow level rises, in addition to extremes, were considerably more likely to occur during the month of February compared to any other month.

Results also suggest there exists a strong relationship between extreme SLC and periods of enhanced integrated water vapor transport (IVT) including during western U.S. landfalling atmospheric rivers. For all radars, we found radar-averaged IVT maxima were larger (by up to ~150 kg m^{-1} s^{-1}) during extreme snow level rises compared to non-extreme rises. The same held true for snow level falls (up to ~260 kg m^{-1} s^{-1} larger for extremes) for all but two radars. The chances of detecting an extreme +SLC were decreased by more than a fourth with a smaller-magnitude averaged maximum IVT (< 600 kg m^{-1} s^{-1}) compared to maximum IVT magnitudes 5-11 times larger (1000-1100 kg^{-1} m s^{-1}). Mean SLC magnitudes were nearly twice and 1.5 times larger in magnitude for snow level rises and falls, respectively, during these larger-magnitude maximum IVT periods compared to during smaller-magnitude IVT periods.

Key findings of this dissertation involving relationships between extreme SLCs and atmospheric rivers also support the direct relationship found between extreme SLC percentages and SLC magnitudes, and maximum IVT values. Depending on the radar, 60-100% of extreme SLCs coincided with an atmospheric river (within ± six hours), compared to 35-60% of non-extremes. These findings suggest extreme SLCs and larger mean SLC magnitudes are more likely during high-moisture conditions which supply a key ingredient to encourage storm formation. Additionally, the detection algorithm resulting from this dissertation work identified extreme intrastorm SLCs during the 2017 Oroville Spillway Emergency, 2019 Valentine's Day event, and other high-impact events that motivated these studies. This result emphasizes the key role SLCs can have in determining storm impacts.

For future work, investigations of relationships between extreme SLC and frontal systems with or without embedded atmospheric rivers will be helpful. More specifically, considerations of diabatic and additional thermodynamic processes that may alter atmospheric stabilities or temperatures within snow level-relevant altitudes are encouraged. Examples include localized processes such as wet-bulbing, horizontal temperature advection, latent heating or cooling through storm and precipitation processes, and related interactions. These processes may yield local variations in atmospheric stabilities that allow for even slight changes in atmospheric conditions (e.g., weak temperature advection) to rapidly and dramatically alter snow levels.

Additionally suggested are explorations of relationships between extreme SLCs and ocean-atmosphere teleconnections stemming from large-scale modes of climate variability. Investigations of relevancies to numerical weather prediction and regional streamflow forecasting may also add value. Included in this category are considerations of localized diabatic processes which likely affect snow levels, but present challenges in model microphysics parameterization. Future work may also benefit from the use of reanalysis data to include a longer time series of snow level estimates and computed SLCs, or to include non-brightband rain types when identifying and examining precipitation periods (e.g., to compare to semicontinuous snow level events identified in this research).

Further, it is recommended that ensuing investigations emphasize precipitation during extreme SLCs of varying sign, magnitude, change-rate, and type (e.g., one versus multiple extremes in a single event). Finally, this dissertation work observed certain extreme SLC cases in connection with negative hydro-societal impacts. As such, future studies should place emphasis on comprehensively assessing streamflow responses and societal impacts of extreme SLCs, including damage to life and infrastructure, and disruptions to ecosystems. The methodologies, findings, and data catalogues provided through this dissertation support ongoing and forthcoming research involving rapid and substantial changes in snow level as well as their atmospheric drivers, and impacts on hydrology and communities.

Chapter 5

Bibliography

Abatzoglou, J.T., 2016: Contribution of cutoff lows to precipitation across the United States. *J. Appl. Meteor. Climatol.*, **55**, 893-899, https://doi.org/10.1175/JAMC-D-15-0255.1.

Adusumilli, S., M.A. Fish, H.A. Fricker, and B. Medley, 2021: Atmospheric river precipitation contributed to rapid increases in surface height of the West Antarctic Ice Sheet in 2019. *Geophys. Res. Lett.*, **48**, e2020GL091076, https://doi.org/10.1029/2020GL091076.

Aldern, J.D., and R.W. Goode, 2014: The stories hold water: learning and burning in North Fork Mono homelands. *Decolonization: Indigeneity, Education & Society*, **3**, 3, 26-51, https://jps.library.utoronto.ca/index.php/des/article/download/21228/18068.

Andrade-Sánchez, J., R. Eaton-Gonzalez, C. Leyva-Aguilera, and M. Wilken-Robertson, 2021: Indigenous mapping for integrating traditional knowledge to enhance community-based vegetation management and conservation: the Kumeyaay basket weavers of San José de la Zorra, México. *International Journal of Geo-Information*, **10**, 3, 124, https://doi.org/10.3390/ijgi10030124.

Austin, P.M., and A.C. Bemis, 1950: A quantitative study of the "bright band" in radar precipitation echoes. *J. Atmos. Sci.*, **7**, 2, 145-151, https://doi.org/10.1175/1520-0469(1950)007<0145:AQSOTB>2.0.CO;2.

Bao, J.W., S.A. Michelson, P.J. Neiman, F.M. Ralph, and J.M. Wilczak, 2006: Interpretation of enhanced integrated water vapor bands associated with extratropical cyclones: their formation and connection to tropical moisture. *Mon. Wea. Rev.* **134**, 1063-1080, https://doi.org/10.1175/MWR3123.1.

Bartusek, S.T., H. Seo, C.C. Ummenhofer, and J. Steffen, 2021: The role of nearshore air-sea interactions for landfalling atmospheric rivers on the U.S. West Coast. *Geophys. Res. Lett.*, **48**, e2020GL091388, https://doi.org/10.1029/2020GL091388.

Battan, L.J., 1973: *Radar Observation of the Atmosphere*. University of Chicago Press, 324 pp.

Blamey, R.C., A.M. Ramos, R.M. Trigo, R. Tomé, and C.J. Reason, 2018: The Influence of atmospheric rivers over the South Atlantic on winter rainfall in South Africa. *J. Hydrometeor.*, **19**, 127-142, https://doi.org/10.1175/JHM-D-17-0111.1.

California Department of Water Resources (CA-DWR), 2015: Hydroclimate Report: Water Year

2015, https://cawaterlibrary.net/wp-content/uploads/2017/10/a3037_Hydroclimate_report_v11.pdf.

Cordeira, J.M., F.M. Ralph, and B.J. Moore, 2013: The development and evolution of two atmospheric rivers in proximity to western North Pacific tropical cyclones in October 2010. *Mon. Wea. Rev.*, **141**, 4234-4255, https://doi.org/10.1175/MWR-D-13-00019.1.

Cordeira, J.M., J. Stock, M.D. Dettinger, A.M. Young, J.F. Kalansky, and F.M. Ralph, 2019: A 142-year climatology of northern California landslides and atmospheric rivers. *Bull. Amer. Meteorol. Soc.*, **100**, 8, 1499-1509, https://doi.org/10.1175/BAMS-D-18-0158.1.

Corringham, T.W., F.M. Ralph, A. Gershunov, D.R. Cayan, and C.A. Talbot, 2019: Atmospheric rivers drive flood damages in the western United States. *Science Advances*, **5**, 12, 1-7, https://doi.org/10.1126/sciadv.aax4631.

Dacre, H.F., P.A. Clark, O. Martinez-Alvarado, M.A. Stringer, and D.A. Lavers, 2015: How do atmospheric rivers form?. *Bull. Amer. Meteor. Soc.,* **96**, 1243-1255, https://doi.org/10.1175/BAMS-D-14-00031.1.

Debbage, N., P. Miller, S. Poore, K. Morano, T. Mote, and J.M. Shepherd, 2017: A climatology of atmospheric river interactions with the southeastern United States coastline. *Int. J. Climatol.*, **37**, 4077-4091, https://doi.org/10.1002/joc.5000.

DeFlorio, M. J., D.W. Pierce, D.R. Cayan, and A.J. Miller, 2013: Western U.S. extreme precipitation events and their relation to ENSO and PDO in CCSM4. *J. Climate,* **26**, 4231-4243, https://doi.org/10.1175/JCLI-D-12-00257.1.

DeFlorio, M.J., D.E. Waliser, B. Guan, D.A. Lavers, F.M. Ralph, and F. Vitart, F., 2018: Global assessment of atmospheric river prediction skill. *J. Hydrometeor.*, **19**, 2, 409-426, https://doi.org/10.1175/JHM-D-17-0135.1.

Demirdjian, R., J.R. Norris, A. Martin, F.M. Ralph, 2020: Dropsonde observations of the ageostrophy within the pre-cold-frontal low-level jet associated with atmospheric rivers. *Mon. Wea. Rev.*, **148**, 4, 1389-1406, https://doi.org/10.1175/MWR-D-19-0248.1

Dettinger, M.D., K. Redmond, and D. Cayan, 2004: Winter orographic precipitation ratios in the Sierra Nevada - large-scale atmospheric circulations and hydrologic consequences. *J. Hydrometeor.*, **5**, 6, 1102-1116, https://doi.org/10.1175/JHM-390.1.

Dettinger, M.D., F.M. Ralph, T. Das, P.J. Neiman, and D. Cayan, 2011: Atmospheric rivers, floods, and the water resources of California. *Water,* **3**, 455-478, https://doi.org/10.3390/w3020445.

Dettinger, M.D., 2011: Climate change, atmospheric rivers, and floods in California - a multimodel analysis of storm frequency and magnitude changes. *J. of the Amer. Water Res. Assoc.*, **47**, 514-523, https://doi.org/10.1111/j.1752-1688.2011.00546.x.

Dettinger, M.D., 2013: Atmospheric rivers as drought busters on the U.S. West Coast. *J. Hydrometeor.,* **14**, 1721-1732, https://doi.org/10.1175/JHM-D-13-02.1.

Dettinger, M.D., 2016: Historical and Future relations between large storms and droughts in California. *San Francisco Estuary Watershed Sci.*, **14**, 2, https://doi.org/10.15447/sfews.2016v14iss2art1.

Dezfuli, A., 2020: Rare atmospheric river caused record floods across the Middle East. *Bull. Amer. Meteor. Soc.*, **101**, 4, E394-E400. https://doi.org/10.1175/BAMS-D-19-0247.1.

Dixon, P.M., 2006: Bootstrap resampling. *Encyclopedia of Environmetrics*, A.H. El-Shaarawi, W.W. Piegorsch, and G. Høst, Wiley, https://doi.org/10.1002/9780470057339.vab028.

Dong, L., L.R. Leung, J. Lu, and Y. Gao, 2019: Contributions of extreme and non-extreme precipitation to California precipitation seasonality changes under warming. *Geophys. Res. Lett.*, **46**, 13470-13478, https://doi.org/10.1029/2019GL084225.

Dube, Ernest, and E. Munsaka, 2018: The contribution of indigenous knowledge to disaster risk reduction activities in Zimbabwe: A big call to practitioners. *Jàmbá Journal of Disaster Risk Studies*, **10**, https://doi.org/10.4102/jamba.v10i1.493.

Durand, J.R, and Coauthors, 2020: Drought and the Sacramento-San Joaquin Delta, 2012-2016: environmental review and lessons. *San Francisco Estuary and Watershed Science*, **18**, 2, https://doi.org/10.15447/sfews.2020v18iss2art2.

Efron, B., 1979: Bootstrap methods: another look at the jackknife. *The Annals of Statistics*, **7**, 1, 1-26. https://doi.org/10.1214/aos/1176344552.

Gelaro, R., and Coauthors, 2017: The Modern-Era Retrospective Analysis for Research and Applications, version 2 (MERRA-2), *J. Clim.*, **30**, 14, 5419-5454, https://doi.org/10.1175/JCLI-D-16-0758.1.

Gershunov, A., T. Shulgina, F.M. Ralph, D.A. Lavers, and J.J. Rutz, 2017: Assessing the climate-scale variability of atmospheric rivers affecting western North America. *Geophys. Res. Lett.*, **44**, 7900-7908, https://doi.org/10.1002/2017GL074175.

Gershunov, A., and Coauthors, 2019: Precipitation regime change in Western North America: the role of atmospheric rivers. *Scientific Reports.*, **9**, 9944, https://doi.org/10.1038/s41598-019-46169-w.

Gimeno, L., R. Nieto, M. Vázquez, D.A. Lavers, 2014: Atmospheric rivers: a mini-review.

Front. Earth Sci., **2**, 1-2, https://doi.org/10.3389/feart.2014.00002.

Gorodetskaya, I.V., M. Tsukernik, K. Claes, M.F. Ralph, W.D. Neff, and N.P.M. Van Lipzig, 2014: The role of atmospheric rivers in anomalous snow accumulation in East Antarctica. *Geophys. Res. Lett.*, **41**, 6199-6206, https://doi.org/10.1002/2014GL060881.

Guan, B., N.P. Molotch, D.E. Waliser, E.J. Fetzer, and P. J. Neiman, 2010: Extreme snowfall events linked to atmospheric rivers and surface air temperature via satellite measurements. *Geophys. Res. Lett.*, **37**, L20401, https://doi.org/10.1029/2010GL044696.

Guan, B., N.P. Molotch, D.E. Waliser, E.J. Fetzer, and P. J. Neiman, 2013: The 2010/2011 snow season in California's Sierra Nevada: role of atmospheric rivers and modes of large-scale variability. *Water Resour. Res.*, **49**, 6731-6743, https://doi.org/10.1002/wrcr.20537.

Guan, B., and D.E. Waliser, 2015: Detection of atmospheric rivers: evaluation and application of an algorithm for global studies. *J. Geophys. Res. Atmos.*, **120**, 12 514-12 535, https://doi.org/10.1002/2015JD024257.

Guan, B., D.E. Waliser, F.M. Ralph, E.J. Fetzer, and P.J. Neiman, 2016: Hydrometeorological characteristics of rain-on-snow events associated with atmospheric rivers. *Geophys. Res. Lett.*, **43**, 2964-2973, https://doi.org/10.1002/2016GL067978.

Guan, B., D.E. Waliser, and F.M. Ralph, 2018: An intercomparison between reanalysis and dropsonde observations of the total water vapor transport in individual atmospheric rivers. *J. Hydrometeor.*, **19**, 2, 321-337, https://doi.org/10.1175/JHM-D-17-0114.1.

Guan, B., and D.E. Waliser, 2019: Tracking atmospheric rivers globally: spatial distributions and temporal evolution of life cycle characteristics. *Journal of Geophysical Research: Atmospheres*, **124**, 12523-12552, https://doi.org/10.1029/2019JD031205.

Guirguis, K., A. Gershunov, T. Shulgina, R.E.S. Clemesha, and F.M. Ralph, 2018: Atmospheric rivers impacting Northern California and their modulation by a variable climate. *Clim. Dyn.*, **52**, 6569-6583, https://doi.org/10.1007/s00382-018-4532-5.

Hatchett, B.J., M.L. Kaplan, and S. Burak, 2016: Some characteristics of upside-down storms in the northern Sierra Nevada, California-Nevada, USA. *Proceedings of the International Snow Science Workshop*, Breckenridge, CO, http://arc.lib.montana.edu/snow-science/objects/ISSW16_P4.03.pdf.

Hatchett, B.J., S. Burak, J.J. Rutz, N.S. Oakley, E.H. Bair, and M. L. Kaplan, 2017a: Avalanche fatalities during atmospheric river events in the western United States. *J. Hydrometeor.,* **18**, 1359-1374, https://doi.org/10.1175/JHM-D-16-0219.1.

Hatchett, B.J., B. Daudert, C.B. Garner, N.S. Oakley, A.E. Putnam, and A.B. White, 2017b: Winter snow level rise in the northern Sierra Nevada from 2008 to 2017. *Water*, **9**, 11, 899, https://doi.org/10.3390/w9110899.

Hatchett, B.J., 2018: Snow level characteristics and impacts of a spring typhoon-originating atmospheric river in the Sierra Nevada, USA. *Atmosphere*, **9**, 6, 233, https://doi.org/10.3390/atmos9060233.

Hatchett, B.J., and Coauthors, 2020: Observations of an extreme atmospheric river storm with a diverse sensor network. *Earth and Space Science*, **7**, 8, e2020EA001129. https://doi.org/10.1029/2020EA001129.

Hecht, C.W., and J.M. Cordeira, 2017: Characterizing the influence of atmospheric river orientation and intensity on precipitation distributions over North Coastal California, *Geophys. Res. Lett.*, **44**, 9048-9058, https://doi.org/10.1002/2017GL074179.

Henn, B., R. Weihs, A.C. Martin, F.M. Ralph, and T.C. Osborne, 2020: Skill of rain-snow level forecasts for landfalling atmospheric rivers: a multimodel assessment using California's network of vertically profiling radars. *J. Hydrometeor.*, **21**, 4, 751-771, https://doi.org/10.1175/JHM-D-18-0212.1.

Hoffmann, H., 2021: Violin plot. MATLAB Central File Exchange. Last Accessed August 2021, https://www.mathworks.com/matlabcentral/fileexchange/45134-violin-plot.

Hollins, L.X., D.A. Eisenberg, and T.P. Seager, 2018: Risk and resilience at the Oroville Dam. *Infrastructures*, **3**, 4, 49 pp, https://doi.org/10.3390/infrastructures3040049.

Hu, H., F. Dominguez, Z. Wang, D.A. Lavers, G. Zhang, and F.M. Ralph, 2017: Linking atmospheric river hydrological impacts on the U.S. West Coast to Rossby wave breaking. *J. Climate*, **30**, 3381-3399, https://doi.org/10.1175/JCLI-D-16-0386.1.

Jibson, R.W., 2006: The 2005 La Conchita, California, landslide. *Landslides*, **3**, 73-78, https://doi.org/10.1007/s10346-005-0011-2.

Johnston, P.E., J.R. Jordan, A.B. White, D.A. Carter, D.M. Costa, and T.E. Ayers, 2017: The NOAA FM-CW Snow-Level Radar. *J. Atmos. Oceanic Technol.*, **34**, 249-267, https://doi.org/ 10.1175/JTECH-D-16-0063.1.

Jong, B.-T., M. Ting, and R. Seager, 2016: El Niño's impact on California precipitation: seasonality, regionality, and El Niño intensity. *Environ. Res. Lett.*, **11**, 054021, https://doi.org/10.1088/1748-9326/11/5/054021.

Kamae, Y., W. Mei, S. Xie, M. Naoi, and H. Ueda, 2017: Atmospheric rivers over the northwestern Pacific: climatology and interannual variability. *J. Climate,* **30**, 5605-5619, https://doi.org/10.1175/JCLI-D-16-0875.1.

Kim, H.M., Y. Zhou, and M.A. Alexander, 2017: Changes in atmospheric rivers and moisture transport over the Northeast Pacific and western North America in response to ENSO diversity. *Clim. Dyn.*, **52**, https://doi.org/10.1007/s00382-017-35989.

Lamjiri, M.A., M.D. Dettinger, F.M. Ralph, and B. Guan, 2017: Hourly storm characteristics along the U.S. West Coast: role of atmospheric rivers in extreme precipitation. *Geophys. Res. Lett.*, **44**, 7020-7028, https://doi.org/10.1002/2017GL074193.

Lamjiri, M.A, M.D. Dettinger, F.M. Ralph, N.S. Oakley, and J.J. Rutz, 2018: Hourly analyses of the large storms and atmospheric rivers that provide most of California's precipitation in only 10 to 100 hours per year. *San Francisco Estuary and Watershed Science*, **16**, 4, https://doi.org/10.15447/sfews.2018v16iss4art1.

Lavers, D.A., R.P. Allan, E.F. Wood, and A.J. Wade, 2012: The detection of atmospheric rivers in atmospheric reanalyses and their links to British winter floods and the large-scale climatic circulation. J. Geophys. Res., **117**, D20106, https://doi.org/10.1029/2012JD018027.

Lavers, D.A., and G. Villarini, 2015: The contribution of atmospheric rivers to precipitation in Europe and the United States. *J. Hydrol.*, **522**, 382-390, https://doi.org/10.1016/j.jhydrol.2014.12.010.

Lundquist, J.D., P.J. Neiman, B. Martner, A.B. White, D.J. Gottas, and F.M. Ralph, 2008: Rain versus snow in the Sierra Nevada, California: comparing Doppler profiling radar and surface observations of melting level. *J. Hydrometeor.*, **9**, 194-211, https://doi.org/10.1175/2007JHM853.1.

Lundquist, J.D., J.R. Minder, P.J. Neiman, and E. Sukovich, 2010: Relationships between barrier jet heights, orographic precipitation gradients, and streamflow in the northern Sierra Nevada. *J. Hydrometeor.*, **11**, 5, 1141-1156, https://doi.org/10.1175/2010JHM1264.1.

Lynn, E., A. Cuthbertson, M. He, J.P. Vasquez, M.L. Anderson, P. Coombe, J.T. Abatzoglou, and B.J. Hatchett, 2020: Technical note: precipitation-phase partitioning at landscape scales to regional scales. *Hydrol. Earth Syst. Sci.*, **24**, 11, 5317-5328, https://doi.org/10.5194/hess-24-5317-2020.

Marwitz, J.D., 1983: The kinematics of orographic airflow during Sierra storms. *J. Atmos. Sci.*, **40**, 1218–1227, https://doi.org/10.1175/1520-0469(1983)040<1218:TKOOAD>2.0.CO;2.

Matsuo, T., and Y. Sasyo, 1981: Melting of snowflakes below freezing level in the atmosphere.

Journal of the Meteorological Society of Japan, **59**, 1, 10-25, https://doi.org/10.2151/jmsj1965.59.1_10.

McCabe, G.J., M.P. Clark, and L.E. Hay, 2007: Rain-on-snow events in the western United States. *Bull. Amer. Meteor. Soc.*, **88**, 3, 319-328, https://doi.org/10.1175/BAMS-88-3-319.

Metropolis, N., and S. Ulam, 1949: The Monte Carlo method. *Journal of the American Statistical Association*, **44**, 247, 335-341, https://doi.org/10.1080/01621459.1949.10483310.

Minder, J.R., D.R. Durran, and G.H. Roe, 2011: Mesoscale controls on the mountainside snow line. *J. Atmos. Sci.*, **68**, 2107-2127, https://doi.org/10.1175/JAS-D-10-05006.1.

Minder, J.R., and D.E. Kingsmill, 2013: Mesoscale variations of the atmospheric snow line over the Northern Sierra Nevada: multiyear statistics, case study, and mechanisms. *J. Atmos. Sci.,* **70**, 916-938, https://doi.org/10.1175/JAS-D-12-0194.1.

Mock, C.J., 1996: Climatic controls and spatial variations of precipitation in the western United States. *J. Climate*, **9**, 1111–1125, https://doi.org/10.1175/1520-0442(1996)009<1111:CCASVO>2.0.CO;2.

Moore, B.J., P.J. Neiman, F.M. Ralph, and F.E. Barthold, 2012: Physical processes associated with heavy flooding rainfall in Nashville, Tennessee, and vicinity during 1–2 May 2010: the role of an atmospheric river and mesoscale convective systems. *Mon. Wea. Rev.,* **140**, 358-378, https://doi.org/10.1175/MWR-D-11-00126.1.

Mundhenk, B.D., E.A. Barnes, and E.D. Maloney, 2016: All-season climatology and variability of atmospheric river frequencies over the North Pacific. *J. Climate*, **29**, 4885-4903, https://doi.org/10.1175/JCLI-D-15-0655.1.

Neiman, P.J., F.M. Ralph, A.B. White, D.E. Kingsmill, and P.O.G. Persson, 2002: The statistical relationship between upslope flow and rainfall in California's coastal mountains: observations during CALJET. *Mon. Wea. Rev.*, **130,** 1468-1492, https://doi.org/10.1175/1520-0493%282002%29130%3C1468%3ATSRBUF%3E2.0.CO%3B2.

Neiman, P.J., G.A. Wick, F.M. Ralph, B.E. Martner, A.B. White, and D.E. Kingsmill, 2005: Wintertime nonbrightband rain in California and Oregon during CALJET and PACJET: geographic, interannual, and synoptic variability. Mon. Wea. Rev., 133, 5, 1199-1223, https://doi.org/10.1175/MWR2919.1.

Neiman, P.J., F.M. Ralph, G.A. Wick, J.D. Lundquist, and M.D. Dettinger, 2008: Meteorological characteristics and overland precipitation impacts of atmospheric rivers affecting the West Coast of North America based on eight years of SSM/I satellite observations. *J. Hydrometeor.*, **9**, 22-47, https://doi.org/10.1175/2007JHM855.1.

Neiman, P. J., A.B. White, F.M. Ralph, D.J. Gottas, and S.I. Gutman, 2009: A water vapor flux tool for precipitation forecasting. *Proceedings of the Institution of Civil Engineers: Water Management*, **162**, 2, 83-94, https://doi.org/10.1680/wama.2009.162.2.83.

Neiman, P.J., M. Hughes, B.J. Moore, F.M. Ralph, and E.M. Sukovich, 2013: Sierra barrier jets, atmospheric rivers, and precipitation characteristics in Northern California: a composite perspective based on a network of wind profilers. *Mon. Wea. Rev.*, **141**, 4211-4233, https://doi.org/10.1175/MWR-D-13-00112.1.

Neiman, P.J., D.J. Gottas, A.B. White, L.J. Schick, and F.M. Ralph, 2014: The use of snow-level observations derived from vertically profiling radars to assess hydrometeorological characteristics and forecasts over Washington's Green River Basin. *J. Hydrometeor.*, **15**, 2522-2541, https://doi.org/10.1175/JHM-D-14-0019.1.

Newell, R.E., N.E. Newell, Y. Zhu, C. Scott, 1992: Tropospheric rivers? - a pilot study. *Geophys. Res. Letters*, **19**, 24, 2401-2404, https://doi.org/10.1029/92GL02916.

Oakley, N. S., J.T. Lancaster, B.J. Hatchett, J. Stock, F.M. Ralph, S. Roj, S., and S. Lukashov, 2018: A 22-year climatology of cool season hourly precipitation thresholds conducive to shallow landslides in California. *Earth Interactions,* **22**, 14, 1-35, https://doi.org/10.1175/EI-D-17-0029.1.

Payne, A. E., and G. Magnusdottir, 2014: Dynamics of landfalling atmospheric rivers over the North Pacific in 30 years of MERRA reanalysis. *J. Climate*, **27**, 18, 7133-7150, https://doi.org/10.1175/JCLI-D-14-00034.1.

Payne, A.E., and Coauthors, 2020: Responses and impacts of atmospheric rivers to climate change. *Nature Reviews Earth and Environment*, **1**, 143-157, https://doi.org/10.1038/s43017-020-0030-5.

Ralph, F.M., P.J. Neiman, and G.A. Wick, 2004: Satellite and CALJET aircraft observations of atmospheric rivers over the eastern North Pacific Ocean during the winter of 1997/98. *Mon. Wea. Rev.*, 132, 1721-1745, https://doi.org/10.1175/1520-0493(2004)132<1721:SACAOO>2.0.CO;2.

Ralph, F.M., P.J. Neiman, and R. Rotunno, 2005: Dropsonde observations in low-level jets over the northeastern Pacific Ocean from CALJET-1998 and PACJET-2001: mean vertical-profile and atmospheric-river characteristics. *Mon. Wea. Rev.*, **133,** 889-910, https://doi.org/10.1175/WAF-D-13-00025.1.

Ralph, F.M., P.J. Neiman, G.A. Wick, S.I. Gutman, M.D. Dettinger, D.R. Cayan, and A.B. White, 2006: Flooding on California's Russian River: role of atmospheric rivers. *Geophys. Res. Lett.*, **33**, L13801, https://doi.org/10.1029/2006GL026689.

Ralph, F.M., P.J. Neiman, G.N. Kiladis, K. Weickman, and D.W. Reynolds, 2011: A multi-scale observational case study of a Pacific atmospheric river exhibiting tropical-extratropical connections and a mesoscale frontal wave. *Mon. Wea. Rev.*, **139**, 1169-1189, https://doi.org/10.1175/2010MWR3596.1.

Ralph, F.M., and M.D. Dettinger, 2011: Storms, floods, and the science of atmospheric rivers. *Eos Trans.* AGU, **92**, 32, 265, https://doi.org/10.1029/2011EO320001.

Ralph, F.M., and M.D. Dettinger, 2012: Historical and national perspectives on extreme west coast precipitation associated with atmospheric rivers during December 2010. *Bull. Amer. Meteor. Soc.*, **93**, 6, 783-790, https://doi.org/10.1175/BAMS-D-11-00188.1.

Ralph, F.M., T. Coleman, P.J. Neiman, R.J. Zamora, and M.D. Dettinger, 2013a: Observed impacts of duration and seasonality of atmospheric-river landfalls on soil moisture and runoff in coastal northern California. *J. Hydrometeor.*, **14**, 443-459, https://doi.org/10.1175/JHM-D-12-076.1.

Ralph, F.M., and Coauthors, 2013b: The emergence of weather-related test beds linking research and forecasting operations. *Bull. Amer. Meteor. Soc.*, **94**, 8, 1187-1211, https://doi.org/10.1175/BAMS-D-12-00080.1.

Ralph, F.M., and Coauthors, 2017a: Atmospheric rivers emerge as a global science and applications focus. *Bull. Amer. Meteor. Soc.,* **98**, 1969-1973, https://doi.org/10.1175/BAMS-D-16-0262.1.

Ralph, F.M., and Coauthors, 2017b: Dropsonde observations of total integrated water vapor transport within North Pacific atmospheric rivers. *J. Hydrometeor.*, **18**, 2577-2596, https://doi.org/10.1175/JHM-D-17-0036.1.

Ralph, F.M., M.D. Dettinger, M.M. Cairns, T.J. Galarneau, and J. Eylander, 2018: Defining "atmospheric river": how the glossary of meteorology helped resolve a debate. *Bull. Amer. Meteor. Soc.,* **99**, 4, 837-839, https://doi.org/10.1175/BAMS-D-17-0157.1.

Ralph, F.M., J.J. Rutz, J.M. Cordeira, M.D. Dettinger, M. Anderson, D. Reynolds, L.J. Schick, and C. Smallcomb, 2019a: A scale to characterize the strength and impacts of atmospheric rivers. *Bull. Amer. Meteor. Soc.*, **100**, 2, 269-289, https://doi.org/10.1175/BAMS- D-18-0023.1.

Ralph, F.M., and Coauthors, 2019b: Atmospheric River Tracking Method Intercomparison Project (ARTMIP)-early start comparison of atmospheric river detection tools: how many atmospheric rivers hit northern California's Russian River watershed?. *Clim. Dyn.*, **52**, 4973-4994, https://doi.org/10.1007/s00382-018-4427-5.

Ramos, A.M., R.M. Trigo, M.L. Liberato, and R. Tomé, 2015: Daily precipitation extreme events in the Iberian Peninsula and its association with atmospheric rivers. *J. Hydrometeor.*, **16**, 579-597, https://doi.org/10.1175/JHM-D-14-0103.1.

Ramos, A.M., R. Nieto, R. Tomé, L. Gimeno, R.M. Trigo, M.L.R. Liberato, and D.A. Lavers, 2016: Atmospheric rivers moisture sources from a Lagrangian perspective, *Earth Syst. Dynam.*, **7**, 371-384, https://doi.org/10.5194/esd-7-371-2016.

Ramos, A.M., R.C. Blamey, I. Algarra, R. Nieto, L. Gimeno, R. Tomé, C.J. Reason, and R.M. Trigo, 2018: From Amazonia to southern Africa: atmospheric moisture transport through low-level jets and atmospheric rivers. *Ann. N.Y. Acad. Sci.*, https://doi.org/10.1111/nyas.13960.

Ray, A.J., and A.B. White, 2019: The Hydrometeorology Testbed-West Legacy Observing Network: supporting research to applications for atmospheric rivers and beyond. *Atmosphere*, **10**, 9, 533. https://doi.org/10.3390/atmos10090533.

Raymond, C., D. Singh, and R.M. Horton, 2017: Spatiotemporal patterns and synoptics of extreme wet-bulb temperature in the contiguous United States. *Journal of Geophysical Research: Atmospheres*, **122**, 13, 108-13, 124, https://doi.org/10.1002/2017JD027140.

Rutz, J.J., and W.J. Steenburgh, 2012: Quantifying the role of atmospheric rivers in the interior western United States. *Atmos. Sci. Lett.*, **13**, 257–261, https://doi.org/10.1002/asl.392.

Rutz, J.J., W.J. Steenburgh, and F.M. Ralph, 2014: Climatological characteristics of atmospheric rivers and their inland penetration over the western United States. *Mon. Wea. Rev.,* **142**, 905-921, https://doi.org/10.1175/MWR-D-13-00168.1.

Rutz, J.J., W.J. Steenburgh, and F.M. Ralph, 2015: The inland penetration of atmospheric rivers over western North America: a Lagrangian analysis. *Mon. Wea. Rev.,* **143**, 1924-1944, https://doi.org/10.1175/MWR-D-14-00288.1.

Ryoo, J., Y. Kaspi, D.W. Waugh, G.N. Kiladis, D.E. Waliser, E.J. Fetzer, and J. Kim, 2013: Impact of Rossby wave breaking on U.S. West Coast winter precipitation during ENSO events. *J. Climate,* **26**, 6360-6382, https://doi.org/10.1175/JCLI-D-12-00297.1.

Saltikoff, E., and Coauthors, 2019: An overview of using weather radar for climatological studies: successes, challenges, and potential. *Bull. Amer. Meteor. Soc.*, **100**, 9, 1739-1752, https://doi.org/10.1175/BAMS-D-18-0166.1.

San Diego Integrated Regional Water Management (IRWM) Program, 2017: Tribal water stories of coastal southern California. Last modified October 2017, Accessed June 2021, https://www.sdirwmp.org/pdf/TribalWaterStories.pdf.

Sellars, S.L., B. Kawzenuk, P. Nguyen, F.M. Ralph, and S. Sorooshian, 2017: Genesis, pathways, and terminations of intense global water vapor transport in association with large-scale climate patterns. *Geophys. Res. Lett.*, **44**, 12, 465-12, 475, https://doi.org/10.1002/2017GL075495.

Shields, C.A., and Coauthors, 2018: Atmospheric River Tracking Method Intercomparison Project (ARTMIP): project goals and experimental design. *Geosci. Model Dev.*, **11**, 2455-2474, https://doi.org/10.5194/gmd-11-2455-2018.

Smith, B.L., S.E. Yuter, P.J. Neiman, and D.E. Kingsmill, 2010: Water Vapor Fluxes and orographic Precipitation over Northern California Associated with a Landfalling Atmospheric River, *Mon. Wea. Rev.*, **138**, 1, 74-100, https://doi.org/10.1175/2009MWR2939.1.

Smith, R.B., 1979: The influence of mountains on the atmosphere. *Advances in Geophysics*, **21**, 87-230, https://doi.org/10.1016/S0065-2687(08)60262-9.

Stewart, R.E., J.D. Marwitz, J.C. Pace, and R.E. Carbone, 1984: Characteristics through the melting layer of stratiform clouds. J. Atmos. Sci., **41**, 22, 3227-3237, https://doi.org/10.1175/1520-0469(1984)041%3C3227:CTTMLO%3E2.0.CO;2.

Sumargo, E., F. Cannon, F.M. Ralph, and B. Henn, 2020a: Freezing level forecast error can consume reservoir flood control storage: potentials for Lake Oroville and New Bullards Bar reservoirs in California. *Water Resources Research*, **56**, e2020WR027072, https://doi.org/10.1029/2020WR027072.

Sumargo, E., H. McMillan, R.Weihs, C.J. Ellis, A.M. Wilson, and F.M. Ralph, 2020b: A soil moisture monitoring network to assess controls on runoff generation during atmospheric river events. *Hydrological Processes*, **35**, 1, e13998, https://doi.org/10.1002/hyp.13998.

Valipour, M., S.M. Bateni, N.R. Dalezios, M. Almazroui, E. Heggy, Z. Şen, and A.N. Angelakis, 2020: Review of past, present and future observation methods. *Hydrology*, T.V. Hromadka II and P. Rao, Ed.

Vano, J.A., M.D. Dettinger, R. Cifelli, D. Curtis, A. Dufour, K. Miller, J.R. Olsen, and A.M. Wilson, 2019: Hydroclimatic extremes as challenges for the water management community: lessons from Oroville Dam and Hurricane Harvey. *Bull. Amer. Meteor. Soc.*, **100**, 1, S9-S14, https://doi.org/10.1175/BAMS-D-18-0219.1.

Viale, M., and M.N. Nuñez, 2011: Climatology of winter orographic precipitation over the subtropical central Andes and associated synoptic and regional characteristics. *J. Hydrometeor.*, **12**, 481-507, https://doi.org/10.1175/2010JHM1284.1.

Waliser, D., and B. Guan, 2017: Extreme winds and precipitation during landfall of atmospheric rivers. *Nature Geoscience*, **10**, 179-183, https://doi.org/10.1038/ngeo2894.

White, A.B., J.R. Jordan, B.E. Martner, F.M. Ralph, and B.W. Bartram, 2000: Extending the dynamic range of an S-band radar for cloud and precipitation studies. *J. Atmos. Oceanic Technol.*, **17**, 9, 1226-1234, https://doi.org/10.1175/1520-0426(2000)017<1226:ETDROA>2.0.CO;2.

White, A.B., D.J. Gottas, E.T. Strem, F.M. Ralph, and P.J. Neiman, 2002: An automated brightband height detection algorithm for use with Doppler radar spectral moments. *J. Atmos. Oceanic Technol.*, **19**, 687-697, https://doi.org/10.1175/1520-0426(2002)019<0687:AABHDA>2.0.CO;2.

White, A.B., P.J. Neiman, F.M. Ralph, D.E. Kingsmill, and P.O.G. Persson, 2003a: Coastal orographic rainfall processes observed by radar during the California Land-Falling Jets Experiment. *J. Hydrometeor.*, **4**, 2, 264-282, https://doi.org/10.1175/1525-7541(2003)4<264:CORPOB>2.0.CO;2.

White, A.B., D.J. Gottas, F.M. Ralph, and P.J. Neiman, 2003b: Operational bright-band snow level detection using Doppler radar. U.S. Patent 6, 615, 140, Filed 30 August 2001, and Issued 2 September 2003.

White, A.B., D.J. Gottas, A.F. Henkel, P.J. Neiman, F.M. Ralph, and S.I. Gutman, 2010: Developing a performance measure for snow-level forecasts. *J. Hydrometeor.*, **11**, 739-753, https://doi.org/10.1175/2009JHM1181.1.

White, A.B., and Coauthors, 2013: A twenty-first-century California observing network for monitoring extreme weather events. *J. Atmos. Oceanic Technol.*, **30**, 1585-1603, https://doi.org/10.1175/JTECH-D-12-00217.1.

White, A.B., B.J. Moore, D.J. Gottas, and P.J. Neiman, 2019: Winter storm conditions leading to excessive runoff above California's Oroville Dam during January and February 2017. *Bull. Amer. Meteor. Soc.*, **100**, 55-70, https://doi.org/10.1175/BAMS-D-18-0091.1.

Whiton, R. C., P.L. Smith, S.G. Bigler, K.E. Wilk, and A.C. Harbuck, 1998: History of operational use of weather radar by U.S. weather services. part I: the pre-NEXRAD era. *Wea. Forecasting*, **13**, 2, 219-243, https://doi.org/10.1175/1520-0434(1998)013<0219:HOOUOW>2.0.CO;2.

Wick, G.A., P.J. Neiman, F.M. Ralph, and T.M. Hamill, 2013: Evaluation of forecasts of the water vapor signature of atmospheric rivers in operational numerical weather prediction models. *Wea. Forecasting,* **28**, 1337-1352, https://doi.org/10.1175/WAF-D-13-00025.1.

Young, A.M., K.T. Skelly, and J.M. Cordeira, 2017: High-impact hydrologic events and atmospheric rivers in California: an investigation using the NCEI storm events database. *Geophys. Res. Lett.*, **44**, 3393-3401, https://doi.org/10.1002/2017GL073077.

Zhang, H., and H. Nakagawa, 2018: Validation of indigenous knowledge for disaster resilience against river flooding and bank erosion. *Science and Technology in Disaster Risk Reduction in Asia*, 57-76, https://doi.org/10.1016/B978-0-12-812711-7.00005-5.

Zhou, Y., H. Kim, and B. Guan, 2018: Life cycle of atmospheric rivers: identification and climatological characteristics. J*ournal of Geophysical Research: Atmospheres*, **123**, 12, 715-12, 725, https://doi.org/10.1029/2018JD029180.

Zhu, Y, and R.E. Newell, 1994: Atmospheric rivers and bombs. *Geophys. Res. Lett.*, **21**, 18, 1999-2002, https://doi.org/10.1029/94GL01710.

Zhu, Y., and R.E. Newell, 1998: A proposed algorithm for moisture fluxes from atmospheric rivers. *Mon. Wea. Rev.*, **126**, 725-735, https://doi.org/10.1175/1520-0493(1998)126<0725:APAFMF>2.0.CO;2

Appendix A: Supplemental Materials for Chapter 2

Table A.1. Methodology flow table describing snow level data quality filters and steps to compute intrastorm SLCs (multi-page table).

Initial Steps (for Filters 1a & 1b)	Compute max-resolution snow level changes (SLCs), and check if *fairly substantial*
1. Find beginning value, X_t (or $X_{t,before}$ if X_t does not exist)	If value exists, use X_t Otherwise, search within the hour before for nearest real value ($X_{t-10\,min}$ to $X_{t-70\,min}$), $X_{t,before}$
2. Find ending value, $X_{t+10\,min}$ (or $X_{t,after}$ if $X_{t+10\,min}$ does not exist)	If value exists, use $X_{t+10\,min}$ Otherwise, search within the hour before for nearest real value ($X_{t+20\,min}$ to $X_{t+80\,min}$), $X_{t,after}$
3. If <u>*both*</u> 1. and 2. exist, subtract 1. from 2. to compute change, and proceed to 4.	Otherwise, disregard and compute next change, starting at 1.
4. Check for single measurement both 1-h before and 1-h after the change	If there is <u>*not*</u> a value within the hour preceding <u>*and*</u> the hour following the change, disregard and compute next change, starting at 1. Otherwise, proceed to 5.
5. Check if max-resolution change is *fairly substantial* (≥200 m magnitude)	If <u>*not*</u> *fairly substantial*, disregard and compute next change, starting at 1. Otherwise, proceed to 6.

Table A.1. Methodology flow table, Continued.

Data Filter 1 (a & b) Identify & omit very short-lived, *fairly substantial* changes in snow level

Data Filter 1a Identify & omit peaks dissimilar from mean of surrounding values

(beginning and/or ending change value falls outside ±300 m of mean for 1 h preceding and/or following)

6. a. Check for ≥2 values 1 h *preceding* beginning snow level ($X_{t,before}$) of the *fairly substantial* change

   b. Check for ≥2 values 1 h *following* $X_{t,before}$

   - If *neither* side contains ≥2 values, disregard and compute next change, returning to 1.
   - If *both* sides contain ≥2 values, compute mean (at right) for values 1-h *preceding* $X_{t,before}$ *and* for values 1-h *following* ⇨ Compute *max* & *minimum* allowable limits:
     - i. $X_{min,preceding} = \bar{X}_{preceding} - 300\ m$*
     - ii. $X_{max,preceding} = \bar{X}_{preceding} + 300\ m$
     - iii. $X_{min,following} = \bar{X}_{following} - 300\ m$
     - iv. $X_{max,following} = \bar{X}_{following} + 300\ m$
   - If only *one* side contains ≥2 values, compute 1-h mean (at right) on this side ⇨ Compute i. & ii. *or* iii. & iv., depending on which side contains ≥2 values

   If *both* sets of bounds exist, (i.) to (ii.) & (iii.) to (iv.), and $X_{t,before}$ falls outside at least one, then omit $X_{t,before}$. Proceed to 7.

   If only *one* set of bounds exists and $X_{t,before}$ falls outside, omit $X_{t,before}$ *and* the single value remaining on the opposite side (without bounds). Proceed to 7.

   Otherwise, proceed to 7.

7. Repeat 6., now for values surrounding the change ending value, $X_{t,after}$ (vs. $X_{t,before}$). Then, move 10 min forward (new $X_t = X_{t+10\ min}$) to repeat 1.-7. until all times are considered. After, proceed to 8.

Data Filter 1b Identify & omit remaining peaks dissimilar from surrounding values

(no similar measurement, i.e., value within ±100 m, exists within 30 min preceding or following the beginning and/or ending change value)

8. a. Check for value within 30 min *preceding* beginning snow level ($X_{t,before}$) of the *fairly substantial* change (if computed in 1.-5.)

   b. Check for value 30 min *following* $X_{t,before}$

   - If *neither* side contains at least one value within ±100 m* of $X_{t,before}$, then omit $X_{t,before}$ & proceed to 9.
   - If *one* or *both* sides contain *at least one* value within ±100 m of $X_{t,before}$, then keep $X_{t,before}$ as is & proceed to 9.

9. Repeat 8., now for values surrounding the change ending value, $X_{t,after}$ (vs. $X_{t,before}$). Then, move 10 min forward (new $X_t = X_{t+10\ min}$) to repeat 1.-5. & 8.-9. until all times are considered. After, proceed to 10.

Table A.1. Methodology flow table, Continued.

Data Filter 2** Identify & omit snow levels surrounded by nonexistent values *and* without a similar value within a wider range

(no snow level exists 1 h preceding or following a snow level measurement and the nearest value within a wider temporal range, ±6 h, does not fall within ±100 m of the observed measurement)

10. Now, instead of iterating through max-resolution *changes* in snow level, simply consider snow level *measurements*

11.
    a. Check for snow levels 1 h *preceding* the available snow level in focus (X_t)
    b. Check for values 1 h *following* X_t
        - If *one* or *neither* side contains ≥1 value, proceed to 12.
        - If *both* sides contain ≥1 value, move forward to next real snow level, and repeat 11. until all snow levels are considered

12. Find snow levels nearest to X_t, now in wider range (±6 h)
    - If *neither* the 6 h proceeding or following X_t contains a real value within ±100 m of X_t, omit X_t, and proceed to 13.
    - Otherwise, if *one* or *both* sides contains a value within ±100 m of X_t, proceed to 13.

13. Move forward to next available snow level and repeat 11. & 12. until all snow levels are considered

Next:

- Determine *semicontinuous snow level events* (≥50% data available with gaps up to 3 h long for a total event duration ≥3 h)
- Compute *1-h max snow level changes (SLCs)* within pre-determined events (single *max* pos. *or* neg. change within 1 h, with rolling 10-min)

Data Filter 3** Omit extreme SLCs falling at *beginning* or *end* of semicontinuous snow level

(start computing changes 30 min into event and end 1.5 h before end of event, i.e., do not compute first and last 4 max 1-h changes)

- We target SLCs occurring prior to or following a consistent period of brightband precipitation. By doing so, we minimize the number of instances where the pre- or post-change snow level height is likely not sustained long enough for the change to substantially alter impacts.
- When computing 1-h max SLCs, start 30 min after the beginning of the event (i.e., start at 45-minute mark), and compute changes up to 30 min before the final 1-h window (i.e., 1.5 h before event end). For example, for an event lasting 4 h, 20 min (i.e., total of 27 10-min values), compute max 1-h SLCs (with rolling 10-min window) between indices 5 and 17. This means, at maximum, the first and the last 4 possible 1-h changes (i.e., if all 10-min time steps contain a real value) are not considered.

** ±300 m & ±100 m ranges considered in Filters 1 & 2, respectively, were determined based on visual investigations of values surrounding fairly substantial SLCs*
*** Filters 2-3, unlike 1a & 1b, do not require Initial Steps 1.-5 (i.e., fairly substantial SLCs are not computed or considered). Filter 2 assesses snow level measurements. Filter 3 is included while computing 1-h max SLCs.*

Please note: Overall, we remain conservative in our methods in order to minimize the number of false-positive large SLCs.

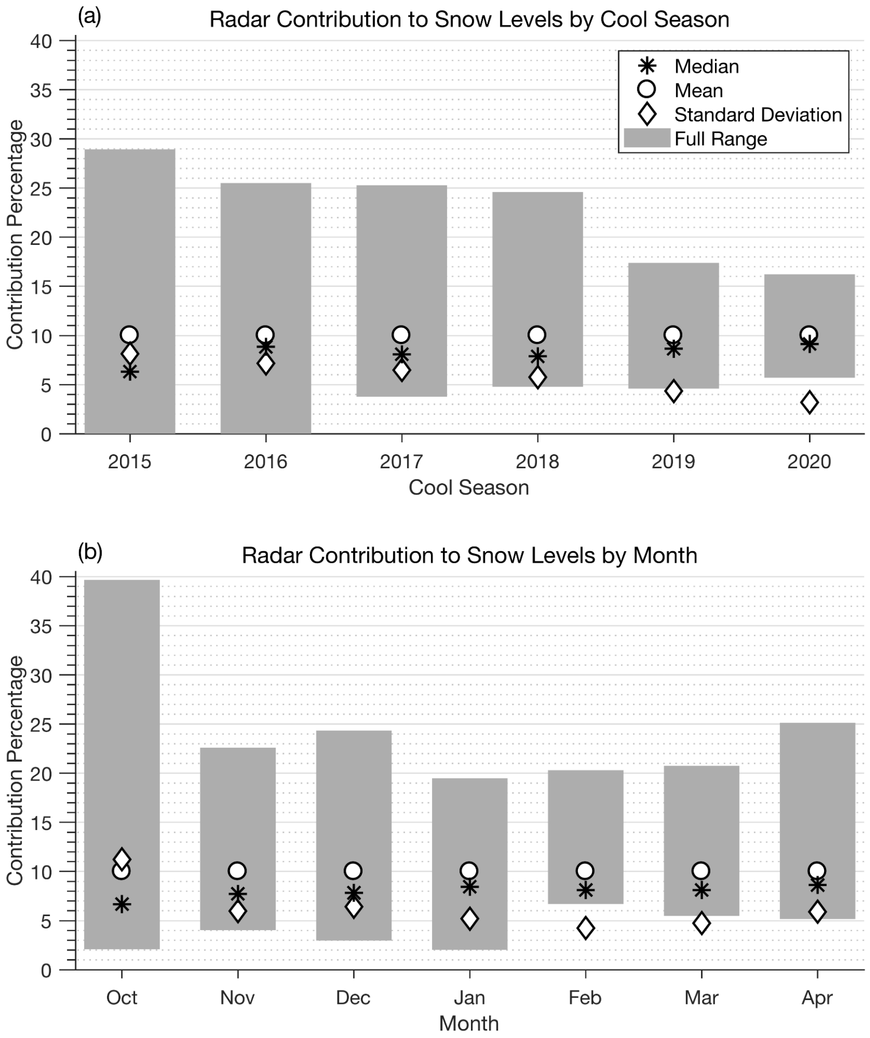

Figure A.1. Radar contribution to each snow level distribution (refer to Figs. 2.7b-c) computed as a percentage of the total number of quality-controlled observations for each (a) cool season and (b) month. For each, the median (black asterisks), mean (white circles), standard deviation (white diamonds), and full range (gray bars) of radar contribution percentages are shown.

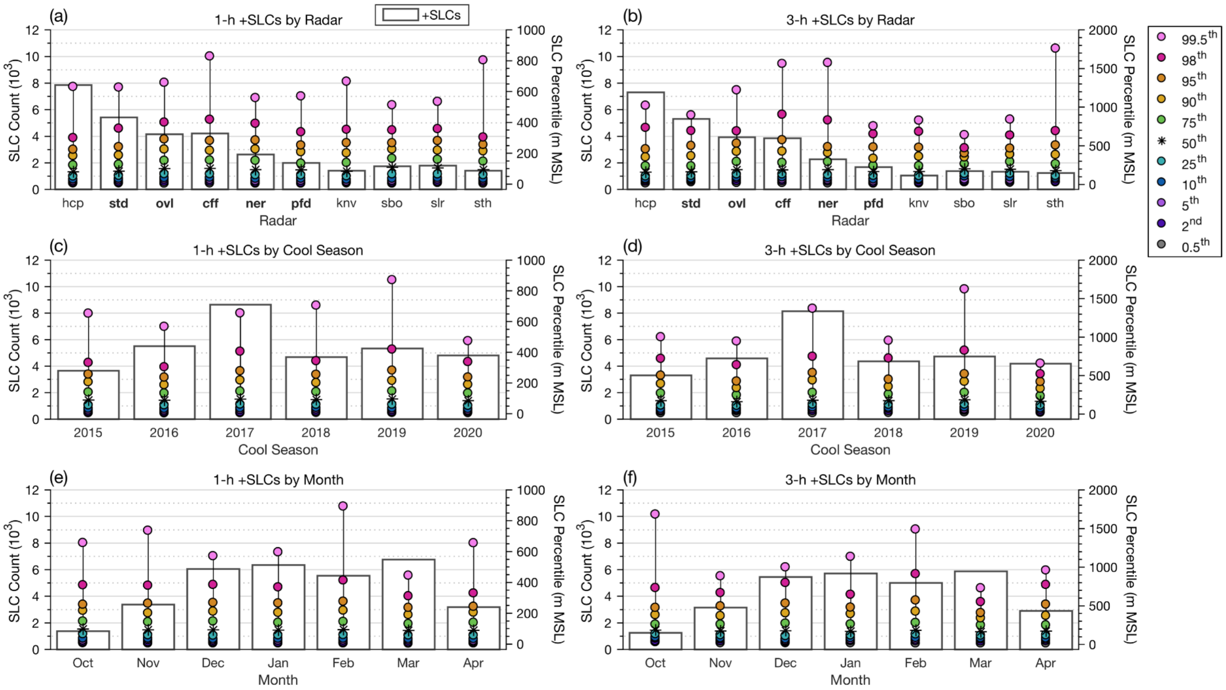

Figure A.2. Same as Figure 2.10, but only for +SLCs.

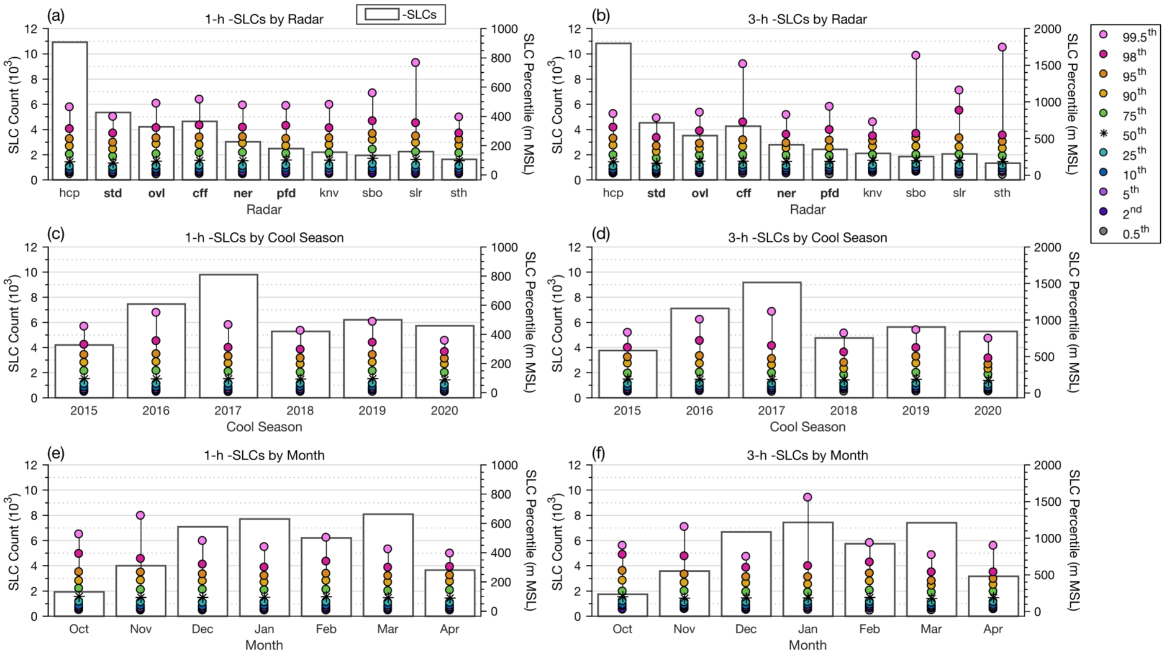

Figure A.3. Same as Figures 2.10 and A.2, but only for -SLCs.

Appendix B: Supplemental Materials for Chapter 3

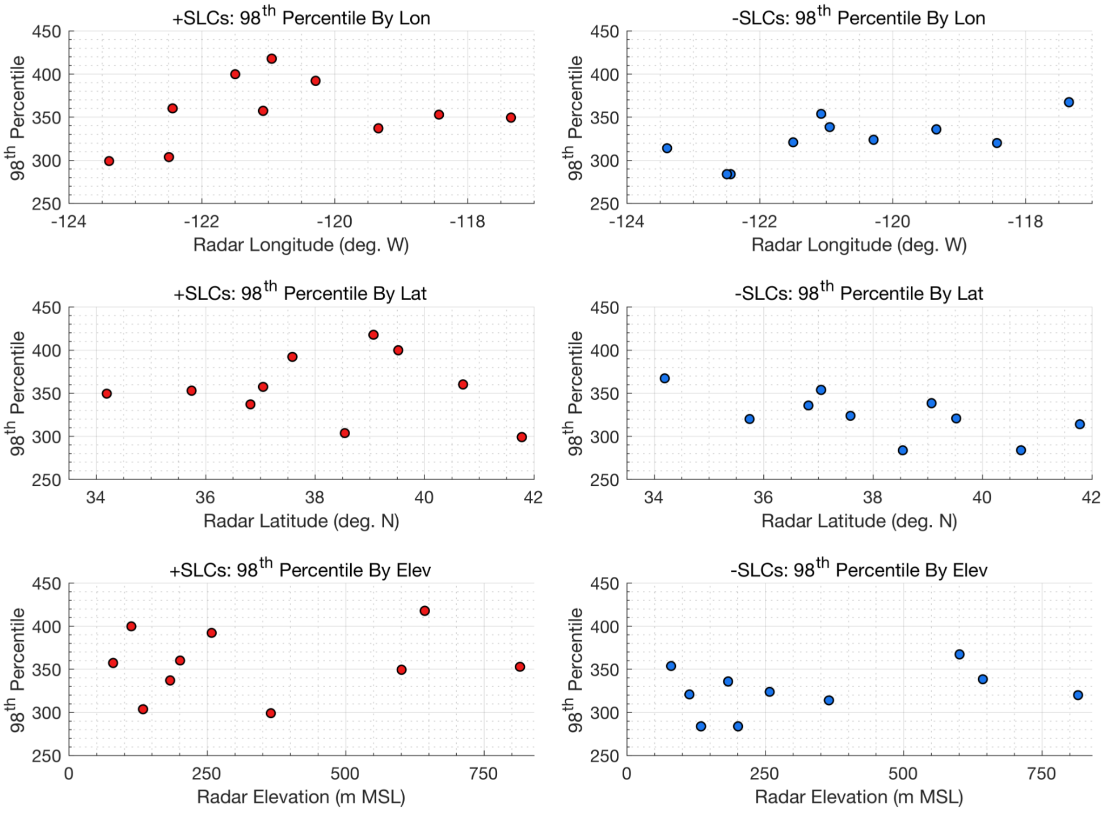

Figure B.1. Scatter plots of 98th percentile magnitudes for all +SLCs (left-column panels; red circles) and -SLCs (right-column; blue circles) by radar longitude (top row), latitude (middle row), and elevation in m MSL (bottom row).

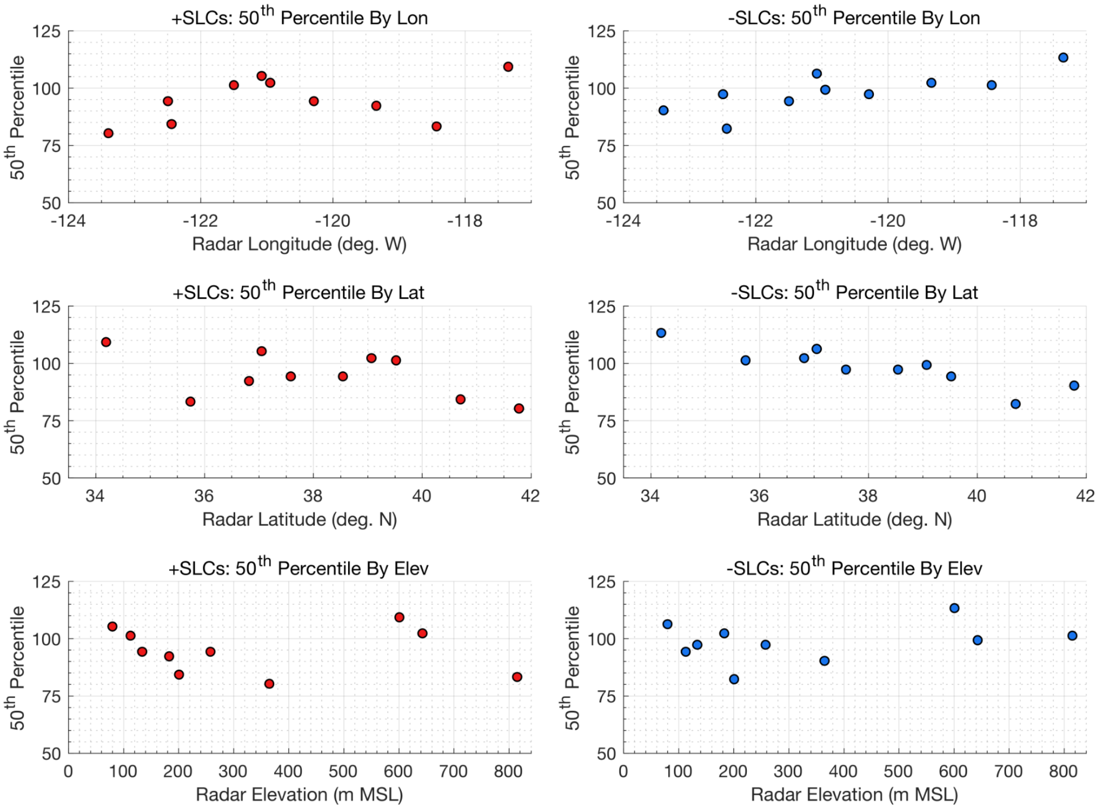

Figure B.2. Same as Figure B.1, but now considering 50th percentile magnitudes (medians).